SAIC 90/1472

ATTENUATION OF REGIONAL PHASES IN FENNOSCANDIA AND ESTIMATES OF ARRIVAL TIME AND AZIMUTH UNCERTAINTY USING DATA RECORDED BY REGIONAL ARRAYS

Thomas J. Sereno, Jr.

Science Applications International Corporation
10260 Campus Point Drive
San Diego, California 92121

September 1990

Semiannual Technical Report #3
1 January 1989 to 30 June 1990

Sponsored By:

Defense Advanced Research Projects Agency (DARPA)
Nuclear Monitoring Research Office (NMRO)
Seismic Detection Capability Modeling

ARPA Order No. 4511 (Amendment 19)

Issued by AFTAC under Contract F08606-88-C-0033.

SAIC 90/1472

ATTENUATION OF REGIONAL PHASES IN FENNOSCANDIA AND ESTIMATES OF ARRIVAL TIME AND AZIMUTH UNCERTAINTY USING DATA RECORDED BY REGIONAL ARRAYS

Thomas J. Sereno, Jr.

Science Applications International Corporation
10260 Campus Point Drive
San Diego, California 92121

September 1990

Semiannual Technical Report #3
1 January 1989 to 30 June 1990

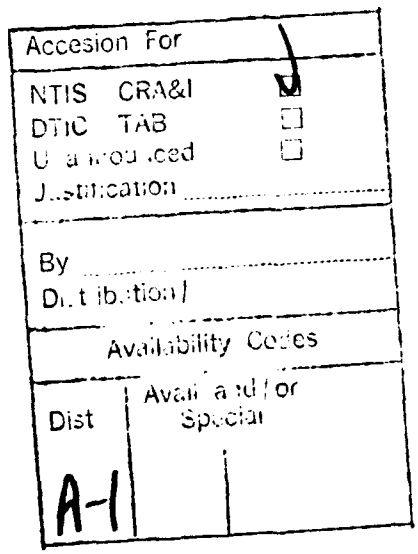

Sponsored By:

Defense Advanced Research Projects Agency (DARPA)
Nuclear Monitoring Research Office (NMRO)
Seismic Detection Capability Modeling

ARPA Order No. 4511 (Amendment 19)

Issued by AFTAC under Contract F08606-88-C-0033.

REPORT DOCUMENTATION PAGE

1a REPORT SECURITY CLASSIFICATION Unclassified	1b RESTRICTIVE MARKINGS
2a SECURITY CLASSIFICATION AUTHORITY	3 DISTRIBUTION / AVAILABILITY OF REPORT Cleared for public release with unlimited distribution
2b DECLASSIFICATION / DOWNGRADING SCHEDULE	
4 PERFORMING ORGANIZATION REPORT NUMBER(S) SAIC-90/1472	5 MONITORING ORGANIZATION REPORT NUMBER(S)
6a NAME OF PERFORMING ORGANIZATION Science Applications International Corporation 6b OFFICE SYMBOL (*If applicable*)	7a NAME OF MONITORING ORGANIZATION Air Force Technical Applications Center/TTR
6c ADDRESS (*City, State, and ZIP Code*) 10260 Campus Pt. Drive San Diego CA 92121	7b ADDRESS (*City, State, and ZIP Code*) HQ/AFTAC/TTR Patrick Air Force Base, FL 32925-6001
8a NAME OF FUNDING / SPONSORING ORGANIZATION Defense Advanced Research Projects Agency 8b OFFICE SYMBOL (*If applicable*) DARPA	9 PROCUREMENT INSTRUMENT IDENTIFICATION NUMBER F08606-88-C-0033
8c ADDRESS (*City, State, and ZIP Code*) 1400 Wilson Blvd. Arlington, VA 22209	10 SOURCE OF FUNDING NUMBERS PROGRAM ELEMENT NO: 62714E; PROJECT NO: 8A10; TASK NO: SOW 3.2; WORK UNIT ACCESSION NO:

11 TITLE (*Include Security Classification*)
Attenuation of regional phases in Fennoscandia and estimates of arrival time and azimuth uncertainty using data recorded by regional arrays

12 PERSONAL AUTHOR(S)
Thomas J. Sereno, Jr.

13a TYPE OF REPORT	13b TIME COVERED	14 DATE OF REPORT (*Year, Month, Day*)	15 PAGE COUNT
Semiannu. Tech Rep #3	FROM 1/1/89 TO 6/30/90	1990 September	115

16 SUPPLEMENTARY NOTATION

17 COSATI CODES		
FIELD	GROUP	SUB-GROUP
8	11	

18 SUBJECT TERMS (*Continue on reverse if necessary and identify by block number*)
Detection capability, location capability, regional networks, attenuation, generalized inversion, arrival time & azimuth uncertainty

19 ABSTRACT (*Continue on reverse if necessary and identify by block number*)

The primary objective of this project is to simulate the detection and location capability of seismic networks that include regional stations and arrays in and around the Soviet Union. This report summarizes several studies of important issues for normalizing these simulations. Initial application is to data recorded by the NORESS and ARCESS arrays in Norway because of the size and quality of the data set and the fact the independent networks provide accurate locations of regional events. ~~We estimate~~ azimuth and arrival time uncertainty are estimated for data recorded by these arrays to normalize simulations of location capability. We estimate frequency-dependent attenuation, source scaling, and site parameters using generalized inverse techniques; noise spectra for primary and secondary phases; and frequency-dependent array gain to normalize detection capability simulations. The normalized simulation method is used to predict

20 DISTRIBUTION / AVAILABILITY OF ABSTRACT	21 ABSTRACT SECURITY CLASSIFICATION
☐ UNCLASSIFIED/UNLIMITED ☒ SAME AS RPT. ☐ DTIC USERS	Unclassified
22a NAME OF RESPONSIBLE INDIVIDUAL Dr. Dean Clauter	22b TELEPHONE (*Include Area Code*) (407) 494-2251 22c OFFICE SYMBOL AFTAC/TTR

DD FORM 1473, 84 MAR 83 APR edition may be used until exhausted
All other editions are obsolete

the detection and location capability of NORESS and ARCESS. These simulations are compared to the capability actually achieved by these arrays to validate the normalization. This method is shown to give accurate results for NORESS and ARCESS, so we are confident that we can use it to determine the sensitivity to network parameters (e.g., number stations, number of arrays versus single stations, noise levels, etc). The next step is to extrapolate the NORESS/ARCESS results to predict the capability of hypothetical networks in the Soviet Union. However, it is important to include lateral variations in propagation characteristics to simulate capability for such a large area. Therefore, we use a tectonic map of Eurasia to develop a 5°×5° propagation grid. Source coupling is also important for accurate simulations, so we use a map of the surface geology of Eurasia as a guide to identify potential sites for cavity decoupling (e.g., regions of bedded or domed salt).

Table of Contents

LIST OF FIGURES

(THIS PAGE INTENTIONALLY LEFT BLANK)

LIST OF TABLES

1. INTRODUCTION

1.1 Project Objectives

The objective of this two-year study is to simulate detection and location capability of seismic networks that include regional stations and arrays in and around the Soviet Union. Three specific tasks are:

(1) Enhance and validate the extended version of the Seismic Network Assessment Program for Detection [*SNAP/D*, *Ciervo et al.*, 1985] called *SNAP/DX* [*Bratt et al.*, 1987] to accurately represent the treaty monitoring capability of seismic networks that include regional stations and arrays.

(2) Normalize *SNAP/DX* to the observed performance of existing stations and expected conditions in and around the Soviet Union.

(3) Apply the normalized simulation methods to assess the treaty monitoring capability of existing and proposed seismic networks.

1.2 Current Status

During the first year of this project we completed our enhancements to the *SNAP/DX* computer program and started to work on *SNAP/DX* normalization. The first semi-annual report describes the normalization results obtained during the first six months of the project [*Sereno*, 1989]. This included two studies: (1) a theoretical study of the sensitivity of *Pn* geometric spreading to the velocity gradient in the upper mantle, and (2) an empirical study of the attenuation of *Pn* and *Lg* phases recorded in eastern Kazakhstan. The purpose of the first study was to determine the frequency dependence of *Pn* geometric spreading for a few simple spherical earth models. This is important since most methods for estimating *Pn* attenuation require assumptions about the geometric spreading. The purpose of the second study was to examine how well our attenuation models based on data recorded in Fennoscandia match observations of wave propagation in the Soviet Union. This is important because there are too few data recorded in the Soviet Union to develop a complete attenuation model. Therefore, we would like to use our models that are based on attenuation and noise conditions at the NORESS and ARCESS arrays in Norway (if they are consistent with the few data that are available) to normalize the simulations.

The first annual report describes our enhancements to the *SNAP/DX* computer program [*Sereno et al.*, 1990]. The most important is the introduction of frequency dependence into the estimates for the source, station noise (for primary and secondary phases), attenuation, and array gain. The original *SNAP/D* and *SNAP/DX* calculate detection and location capability at fixed frequency, which is adequate to represent the capability for teleseismic events since the dominant signal frequency is only weakly dependent on distance. However, at regional distances the frequency of the maximum signal-to-noise ratio (*snr*) may be strongly distance-dependent. Therefore, accurate simulations

require that the detection capabilities at individual stations be evaluated at a frequency that depends on epicentral distance. The annual report introduces our new network simulation program, *NetSim*. It includes functional descriptions of the detection and location modules and detailed descriptions of each input and output parameter.

This is the third semi-annual report. It describes a new and more complete normalization of the simulations using NORESS and ARCESS data. Estimates of the uncertainty of arrival time and azimuth measurements are included to normalize simulations of the location capability of regional networks. We use data from more than 400 events with four or more defining phases recorded at both NORESS and ARCESS between October 1989 and March 1990. However, since the residuals were determined from the same data that were used to locate the events, it is possible that the variance estimates (particularly for arrival time) are biased low. To check this, we calculated the arrival time difference between NORESS and ARCESS for mining explosions with accurate locations determined from satellite imagery. This difference is compared to the theoretical difference in arrival time based on travel time tables for Fennoscandia. The use of arrival time difference between two stations eliminates the need for accurate estimates of event origin time. This method also facilitates separation of measurement error (from the consistency of arrival time difference for repeated events in the same mine) from modeling error (by comparing the mean arrival time difference between NORESS and ARCESS for each mine to the theoretical arrival time difference based on travel time tables for Fennoscandia).

To simulate detection capability we need parameters to describe frequency-dependent attenuation of regional phases, source scaling relations, and noise spectra for primary and secondary phases. In a previous project we estimated *Pn* and *Lg* attenuation for paths to NORESS [*Sereno et al.*, 1988]. However, it is not possible to resolve trade-offs among source and attenuation parameters using data recorded by only one station. In this study, parameter trade-off resolution is improved by adding data from a second array and by inverting spectra from up to four seismic phases simultaneously. The data are *Pn*, *Pg*, *Sn*, and *Lg* spectra recorded at NORESS and ARCESS from nearly 100 regional events with magnitudes between 2.0 and 3.6, and epicentral distances between 200 and 1600 km. The results are *Pn* and *Lg* attenuation models with better parameter trade-off resolution, and new models for frequency-dependent *Pg* and *Sn* attenuation in Fennoscandia. It is also important to determine noise spectra for primary and secondary phases. It is straight-forward to estimate the ambient noise spectra (for primary phases), but the noise for secondary phases is complicated by the coda of earlier arrivals. In this study, we relate the noise spectra for secondary phases to the amplitude spectrum of earlier arrivals. We validate our normalization by comparing the detection and location capabilities predicted by *NetSim* to those actually achieved by NORESS and ARCESS.

The ultimate objective is to simulate the detection and location capability of networks of seismic stations in Eurasia. It is important to include lateral variations in propagation characteristics to obtain accurate simulations for such a large area. For example, it is well known that first order variations in regional wave propagation are related to

geologic and tectonic features. Therefore, we used a tectonic map of Eurasia to develop a propagation grid on a 5° × 5° scale. We associate orogenic zones with higher attenuation than areas characterized as continental plateaus. Source coupling is also important for accurate simulations. However, variations in surface geology occur at a much smaller scale than the 5° × 5° grid that we use in *NetSim*. Therefore, we use a map of the surface geology of Eurasia only as a guide to identify potential sites for cavity decoupling (e.g., regions of bedded or domed salt).

1.3 Outline of the Report

This report is divided into seven sections, including the introduction and summary. The five main technical sections address the following issues:

- **Section 2.** Arrival time and azimuth uncertainty for regional phases recorded by small aperture arrays.

- **Section 3.** Frequency-dependent attenuation, source scaling, and amplitude variance for regional phases in Fennoscandia.

- **Section 4.** Noise spectra for primary and secondary phases.

- **Section 5.** Detection and location capability of the NORESS and ARCESS arrays, and validation of the normalization.

- **Section 6.** Propagation and source medium grids for Eurasia.

(THIS PAGE INTENTIONALLY LEFT BLANK)

2. AZIMUTH AND ARRIVAL TIME UNCERTAINTY

Estimates of the uncertainty of arrival time and azimuth measurements for regional phases are needed to simulate the location capability of regional seismic networks [e.g., *Bratt et al.*, 1987; *Sereno et al.*, 1990]. In this section, we estimate these uncertainties for data recorded by the NORESS and ARCESS arrays in Norway.

2.1 Data

The data include azimuth and arrival time estimates for regional phases recorded at NORESS and ARCESS during the period October 1989 to March 1990. Each array includes 25 short-period instruments in concentric rings with a maximum diameter of 3 km [*Mykkeltveit*, 1983; *Mykkeltveit et al.*, 1987]. The data include measurements from over 400 regional events. Each event was recorded by both arrays, and the location is constrained by at least four defining phases. Figure 2.1 displays the event epicenters on a map. The epicentral distances are between 200 and 2500 km, and the event magnitudes are between 1.3 and 3.1. These data were published in the *Bulletin of the Intelligent Monitoring System (IMS)* produced at the Center for Seismic Studies (CSS) where they are stored in an on-line relational database. Event detection and location are determined automatically by the *IMS* and the solutions are validated by a seismic analyst [*Bache et al.*, 1990a; *Bratt et al.*, 1990]. In this report, we refer to the *IMS location* as the event location determined after analyst review (e.g., the location reported in the *Bulletin of the Intelligent Monitoring System*).

2.2 Azimuth Uncertainty

The azimuths are estimated automatically for each detection by the *IMS* using a wide band frequency-wavenumber (*f–k*) algorithm [*Kvaerna and Doornbos*, 1986]. The *f–k* power spectrum is computed for a 3-s window staring 1.1 s before the onset time. The calculation is done using all available vertical channels (up to 25 array elements for NORESS and ARCESS) after band-pass filtering [*Bache et al.*, 1990b].

The azimuth residual is defined as the measured azimuth (from the *f–k* analysis) minus the station-to-event azimuth determined from the event location estimated by *IMS*. Since the measured azimuths are used to constrain the *IMS* locations [*Bratt and Bache*, 1988], it is possible that the residuals calculated in this way are biased low. To avoid this, we only consider events that are recorded by both arrays and whose locations are constrained by at least four defining phases (arrival times and azimuths). It is unlikely that the measured azimuths provide a significant constraint on the *IMS* locations of these events (particularly for events that are farther than 500 km from either array). To check this, we compared the azimuth residual for each phase when that phase was included in the *IMS* location to the azimuth residual when that phase was not included. We found that the average absolute difference in the residuals for 66 phases from 14 events was only 0.3° and that this difference was greater than 1° for only three of the

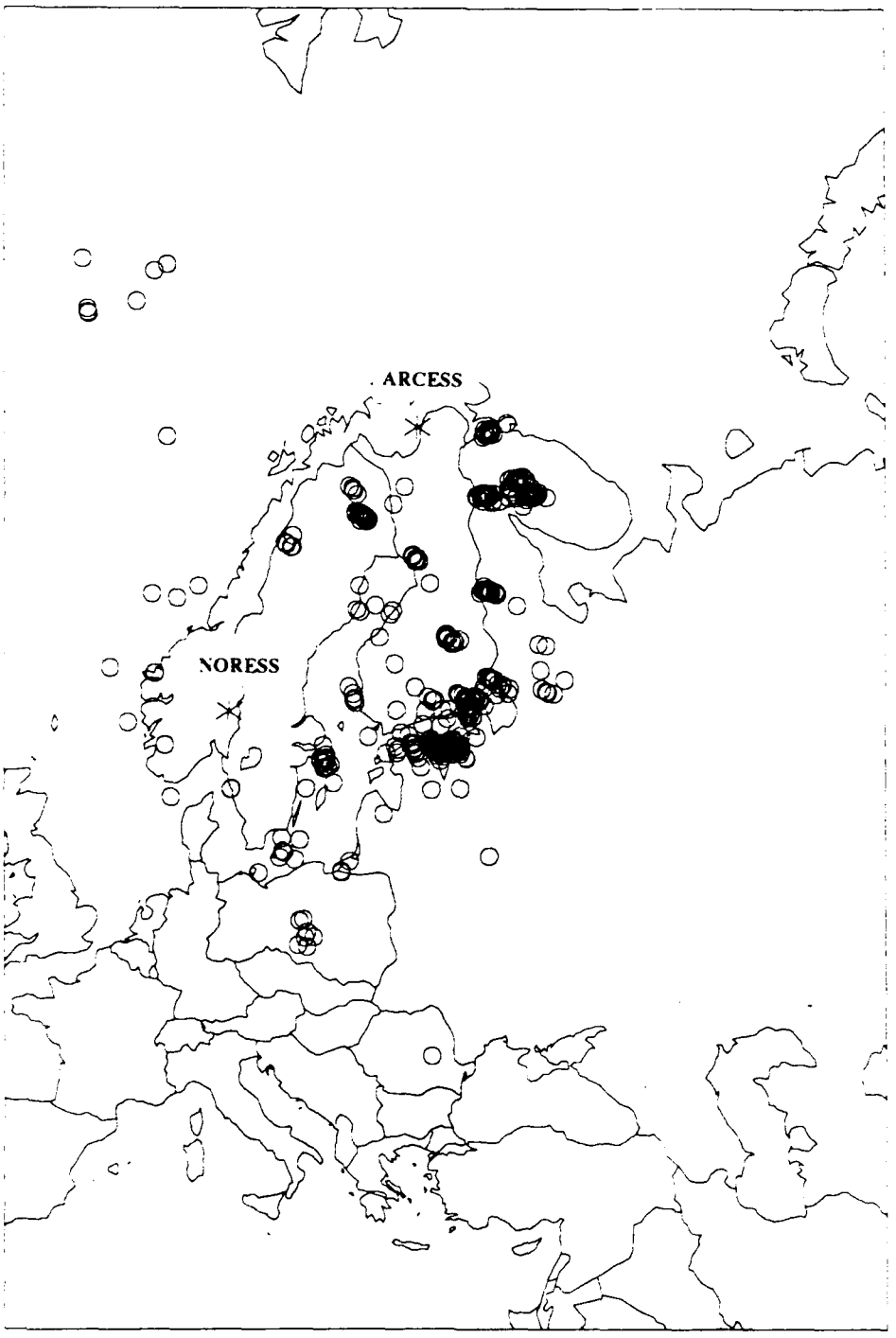

Figure 2.1. Epicenters of the events used to estimate arrival time and azimuth uncertainty for regional phases. The locations of the NORESS and ARCESS arrays are indicated.

66 phases. This suggests that use of the *IMS* locations does not introduce significant bias in the azimuth residuals for events with four or more defining phases.

Table 2.1 lists the mean, $<\Delta\alpha>$, and standard deviation, σ_α, of the azimuth residuals for *Pn*, *Pg*, *Sn*, and *Lg*. Figures 2.2–2.5 are histograms of the azimuth residuals for each phase. The top panel in each figure plots the residuals at NORESS, the middle panel plots the residuals at ARCESS, and the lowest panel plots the residuals combined from both arrays. The average azimuth standard deviation (using data from both arrays) is about 7° for *Pn*, *Sn*, and *Lg*, and it is about 6° for *Pg*. With the exception of *Lg*, the azimuth standard deviations are considerably larger at NORESS than they are at ARCESS. *Bratt et al.* [1990] came to this same conclusion using residuals computed relative to locations published in a bulletin produced by the University of Helsinki (we will call this the Helsinki Bulletin). Their estimates of the azimuth standard deviations for *Pn* at ARCESS, *Lg* at NORESS, and *Sn* at both arrays are within 1° of our estimates in Table 2.1. However, their estimates of the azimuth standard deviations for *Pn* at NORESS (11.1°) and *Lg* at ARCESS (11.0°) are larger than ours. This is probably caused by a difference in the signal-to-noise ratio (*snr*) of the data used in the two studies. For example, we found that the *Lg* azimuth standard deviation is almost 3° greater for arrivals with $snr < 3$ than it is for arrivals with $snr > 3$.

2.3 Arrival Time Uncertainty

The arrival time of each detection is estimated automatically by the *IMS*. These arrival times are reviewed (and modified as required) by a seismic analyst. In Section 2.3.1, we define the *arrival time residual* as the observed arrival time (after analyst review) minus the theoretical arrival time relative to the *IMS* location and origin time. As is the case for the azimuth residuals, arrival time residuals calculated in this way may be biased low since the observed arrival times are used to constrain the event location. The potential for this bias is particularly high for compressional waves because each input datum to the *IMS* location algorithm is weighted by an "a priori" estimate of its standard deviation [*Bratt and Bache*, 1988], and this standard deviation is typically a factor of two smaller for *P* waves than it is for *S* waves. This means that *P* wave arrival times are generally four times more important for constraining the *IMS* locations than are *S* wave arrival times.

In Section 2.3.2 we use a different approach to estimate arrival time uncertainty. Here we consider only events that are explosions in mines with accurate locations determined from satellite imagery. We define the *arrival time difference residual* as the observed difference in arrival time between NORESS and ARCESS minus the theoretical difference based on travel time tables for Fennoscandia. This relative arrival time approach eliminates the effects of errors in the event origin time estimate, and it facilitates separation of measurement errors (from the consistency of the arrival time difference for repeated events in the same mine) from modeling errors (by comparing the mean arrival time difference for each mine site to the theoretical arrival time difference). These results are compared to the results of Section 2.3.1 to estimate the bias introduced by using the *IMS* locations and origin times.

Table 2.1 Mean and standard deviation of azimuth residuals relative to *IMS* locations.

Phase	Station	Number	$\langle\Delta\alpha\rangle$ (°)	σ_α (°)
Pn	NORESS	354	1.2	8.5
	ARCESS	397	0.7	5.3
	BOTH	**751**	**0.9**	**7.0**
Pg	NORESS	22	0.3	7.4
	ARCESS	27	1.0	4.4
	BOTH	**49**	**0.7**	**5.9**
Sn	NORESS	144	-0.8	9.4
	ARCESS	189	-1.1	4.3
	BOTH	**333**	**-1.0**	**7.0**
Lg	NORESS	217	-2.7	6.3
	ARCESS	242	1.6	7.2
	BOTH	**459**	**-0.5**	**7.1**

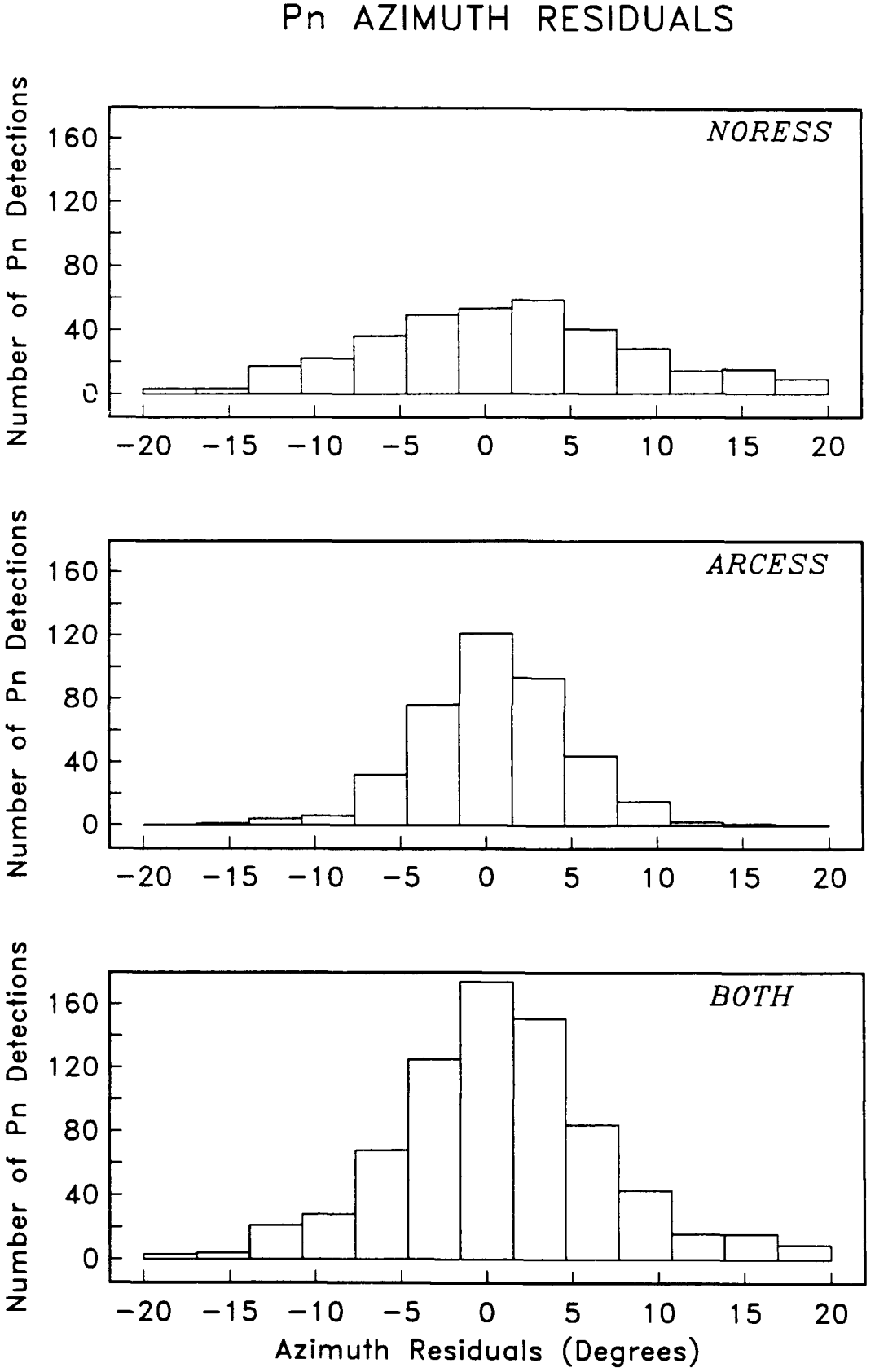

Figure 2.2. Histograms of *Pn* azimuth residuals relative to the *IMS* locations. The residuals are plotted between -20° and 20°. Note that 9 residuals were outside this range (7 from NORESS and 2 from ARCESS).

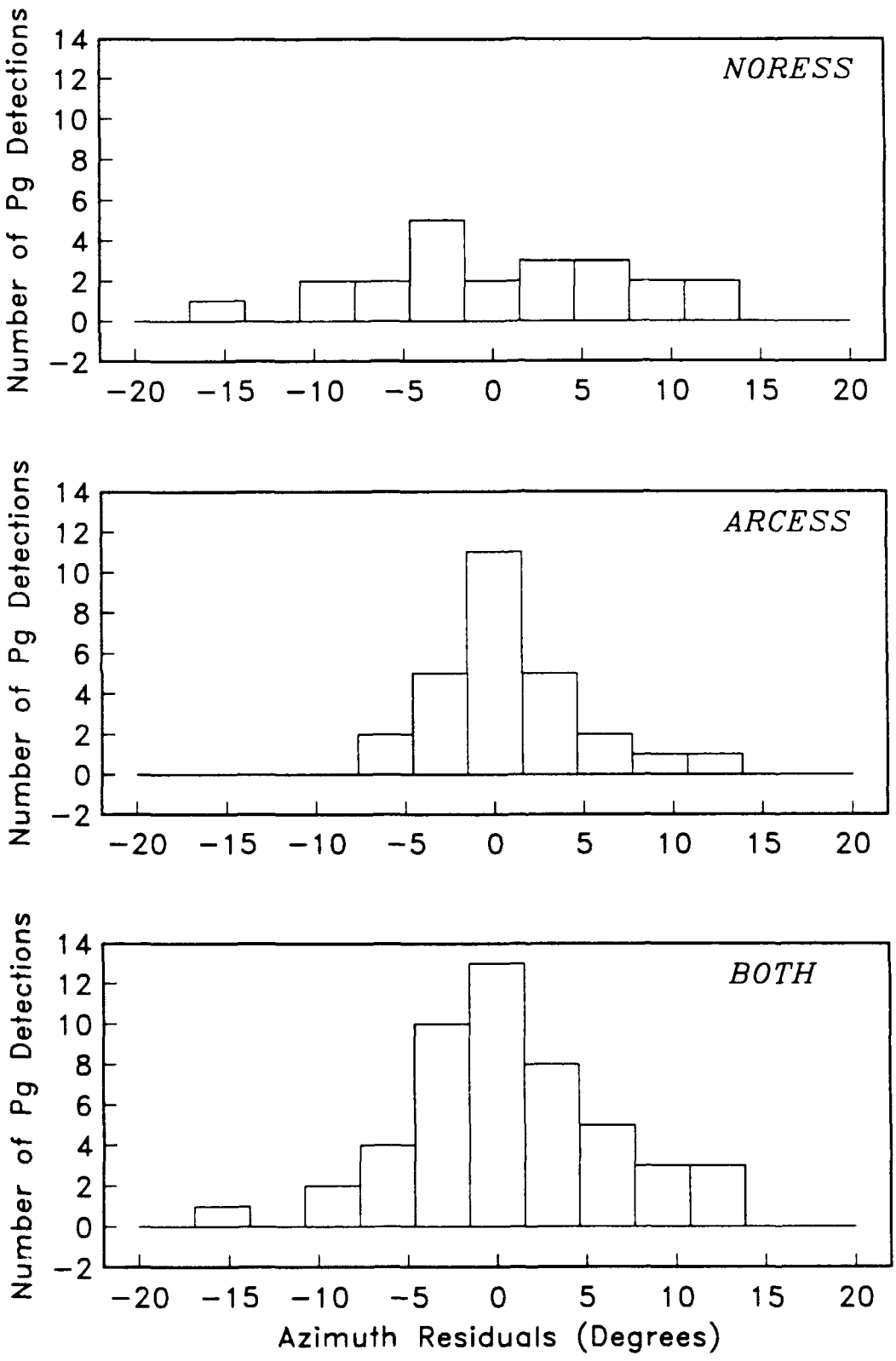

Figure 2.3. Histograms of *Pg* azimuth residuals relative to the *IMS* locations.

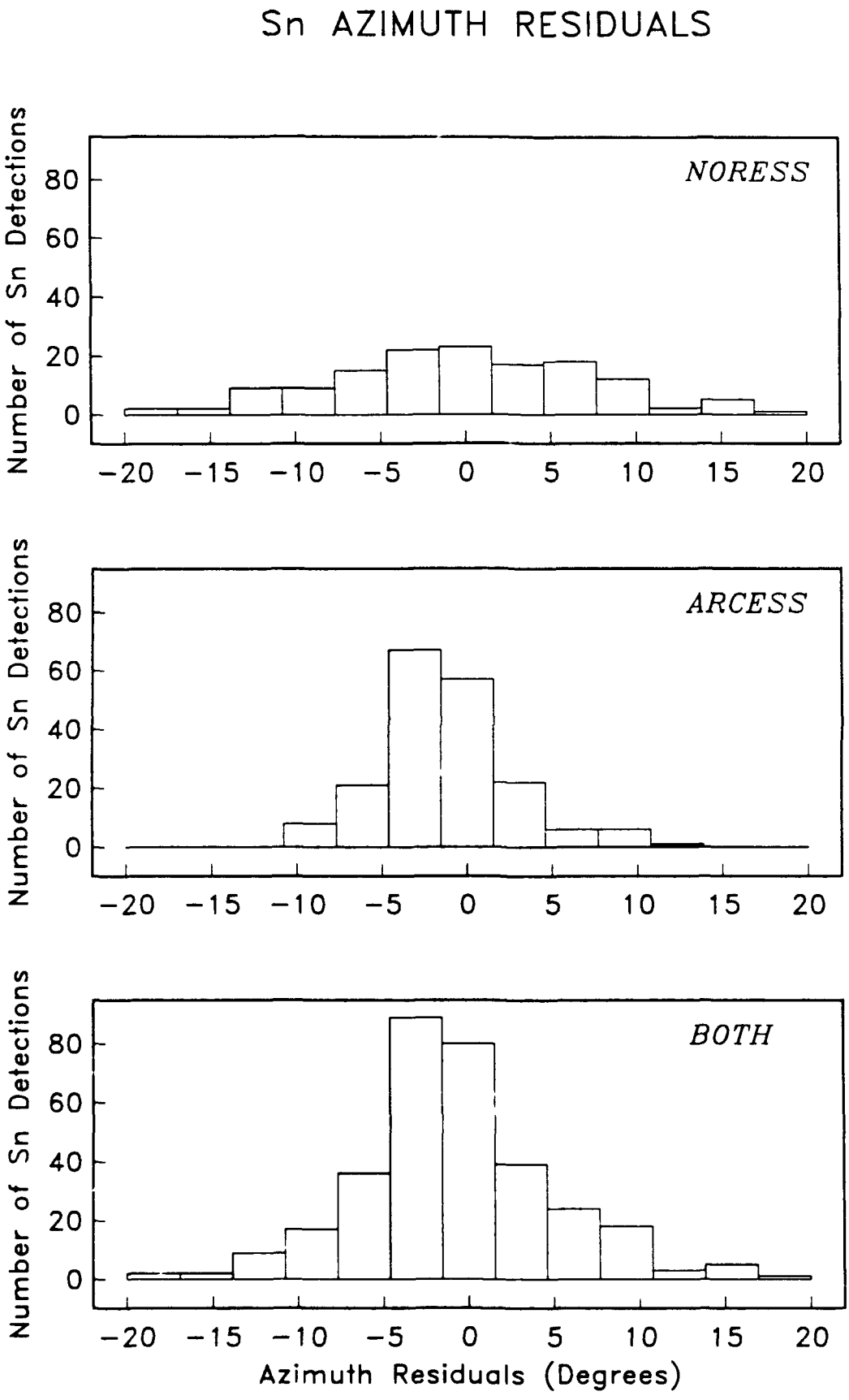

Figure 2.4. Histograms of *Sn* azimuth residuals relative to the *IMS* locations. The residuals are plotted between -20° and 20°. Note that 8 residuals were outside this range (7 from NORESS and 1 from ARCESS).

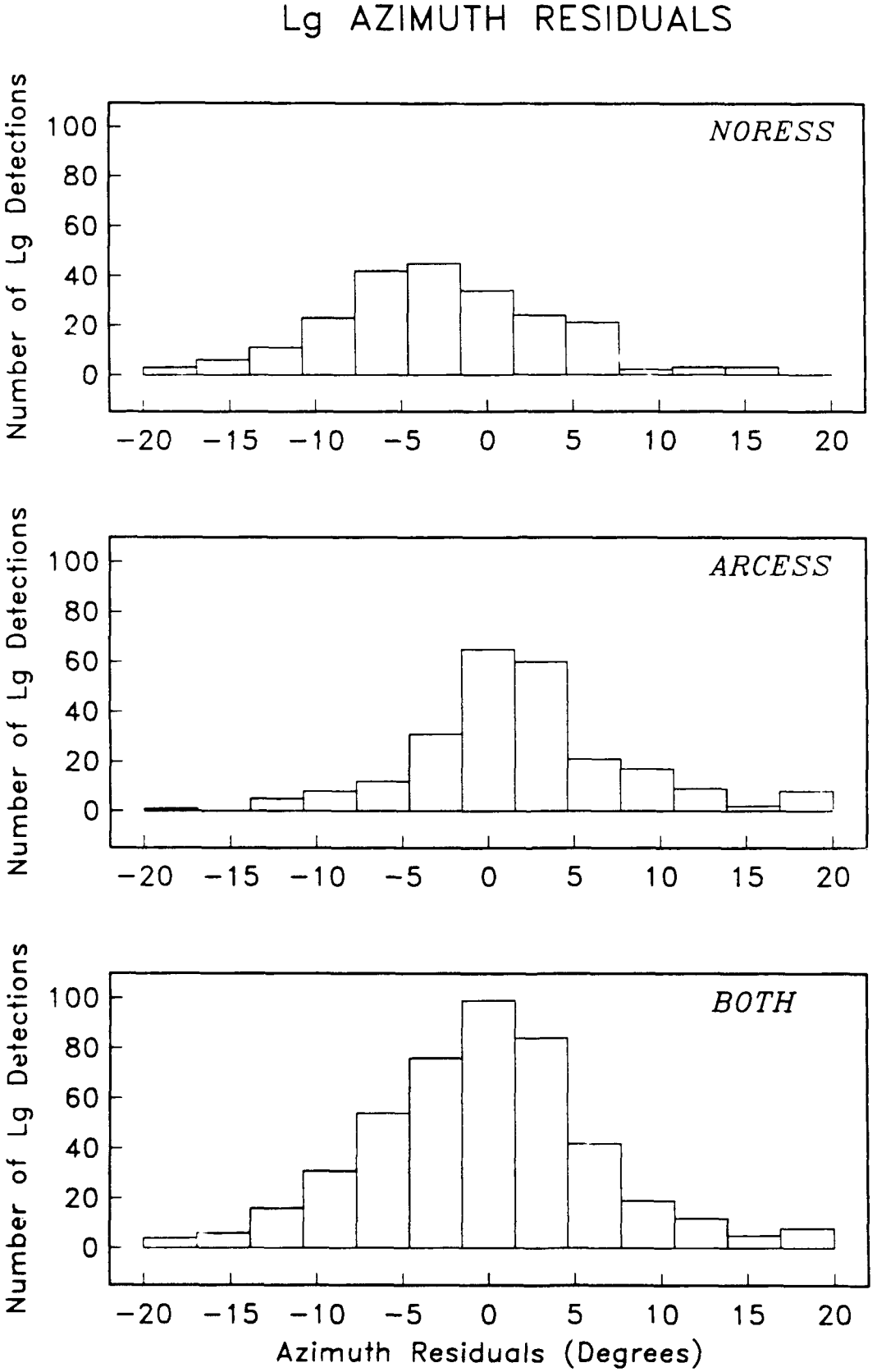

Figure 2.5. Histograms of *Lg* azimuth residuals relative to the *IMS* locations. The residuals are plotted between -20° and 20°. Note that 3 residuals were outside this range (all from ARCESS).

2.3.1 *Uncertainty Based on IMS Locations*

Table 2.2 lists the mean, Δt, and standard deviation, σ_t, of the arrival time residuals for *Pn*, *Pg*, *Sn*, and *Lg* relative to the *IMS* locations and origin times. The arrival time standard deviation is 0.7 s for *Pn* and *Pg* and it is 2.3 s for *Sn* and *Lg*. As discussed above, it is likely that these estimates are biased low for compressional waves. For example, the mean arrival time residuals for *Pn* at NORESS and ARCESS are equal and opposite, which is expected since the event locations determined by the *IMS* minimize these residuals.

There are no significant distance dependencies in the residuals for any of the phases that would indicate errors in the *IMS* travel time tables. However, the mean residual for *Sn* is slightly positive at both arrays, which suggests that the *IMS* value for the shear wave velocity of the upper mantle is too high. An alternative explanation for this positive bias is that *Sn* is picked late for arrivals with low *snr*. For example, we found that the mean residual at ARCESS for arrivals with *snr* < 3 is 1.1 s, but for arrivals with higher *snr* it is only 0.4 s. The arrival time standard deviations also depend on *snr*. For example, the *Sn* and *Lg* standard deviations are 2.4 s and 2.8 s, respectively, for arrivals with *snr* < 3. However, these standard deviations are only 1.5 s and 1.9 s for *snr* > 3.

2.3.2 *Uncertainty Based on Locations from Satellite Imagery*

In this section, we estimate the arrival time variance from the difference between the NORESS arrival time and the ARCESS arrival time for repeated events at known mines sites. This is different from the more conventional approach taken by *Bratt et al.* [1990] who calculated arrival time residuals at NORESS and ARCESS relative to the origin times and locations in the Helsinki Bulletin (in the same way that we used the *IMS* locations in the previous section). Most of the events used in their study are explosions which are assigned directly to mine locations in the Helsinki Bulletin (that is, the arrival times are not inverted for the listed location). Table 2.3 compares the Helsinki mine locations to mine locations determined from satellite imagery. Note that the average offset between the two is 11 km. This difference could cause a bias in the *P* wave residuals calculated relative to the Helsinki mine locations of more than 1 s and a bias in the *S* wave residuals of more than 2 s. Therefore, in this study we use events that are identified as mining explosions in the Helsinki Bulletin, but we calculate the arrival time difference residuals relative to mine locations determined from satellite imagery. The uncertainties of these mine locations are less less than 1 km.

It is difficult to define a unique mapping (such as Table 2.3) between the mine locations in the Helsinki Bulletin and actual mine sites identified on satellite imagery. This is partly because of the high density of mines in some of the regions studied, and partly because some of the Helsinki mine locations are far (> 15 km) from any mines that can be identified on satellite images. For example, Figure 2.6 is a satellite image of a mining region in Estonia. The mine locations used in the Helsinki Bulletin and

Table 2.2 Mean and standard deviation of arrival time residuals relative to *IMS* locations.

Phase	Station	Number	Δt (s)	σ_t (s)
Pn	NORESS	416	0.1	0.7
	ARCESS	427	-0.1	0.7
	BOTH	**843**	**0.0**	**0.7**
Pg	NORESS	28	-0.1	0.6
	ARCESS	31	0.3	0.9
	BOTH	**59**	**0.1**	**0.7**
Sn	NORESS	302	0.4	2.3
	ARCESS	282	0.8	2.2
	BOTH	**584**	**0.6**	**2.3**
Lg	NORESS	350	-0.1	2.5
	ARCESS	348	-0.7	2.0
	BOTH	**698**	**-0.4**	**2.3**

Table 2.3 Mine locations.

Univ. of Helsinki			Satellite Imagery			Offset
Mine ID	Location		Mine ID	Location		(km)
HB5	59.5	26.5	SB5	59.446	26.486	6.1
HB6	59.3	27.2	SB6	59.327	27.070	8.0
HB9	59.2	27.6	SB9	59.269	27.732	10.7
HB10	59.3	27.6	SB10	59.306	27.626	1.6
HB11	59.3	28.1	SB11	59.243	27.833	16.4
HB13	59.4	28.5	SB13	59.370	28.428	5.3
HC1	60.7	28.7	SC1	60.749	28.836	9.2
HC2	60.7	29.0	SC2	60.700	29.181	9.8
HC3	60.6	29.2	SC3	60.581	29.065	7.7
HC4	60.8	29.3	SC4	60.846	28.990	17.6
HC5	60.9	29.3	SC5	61.008	29.038	18.6
HC6	60.9	29.4	SC6	60.953	29.176	13.5
HC7	60.8	29.5	SC7	60.902	29.348	14.0
HC11	61.1	30.2	SC11	61.142	29.870	18.3
HC15	61.4	34.3	SC15	61.558	34.533	21.5
HC17	64.7	30.7	SC17	64.685	30 660	2.5
HD2	69.4	30.8	SD2	69.409	30.955	6.1

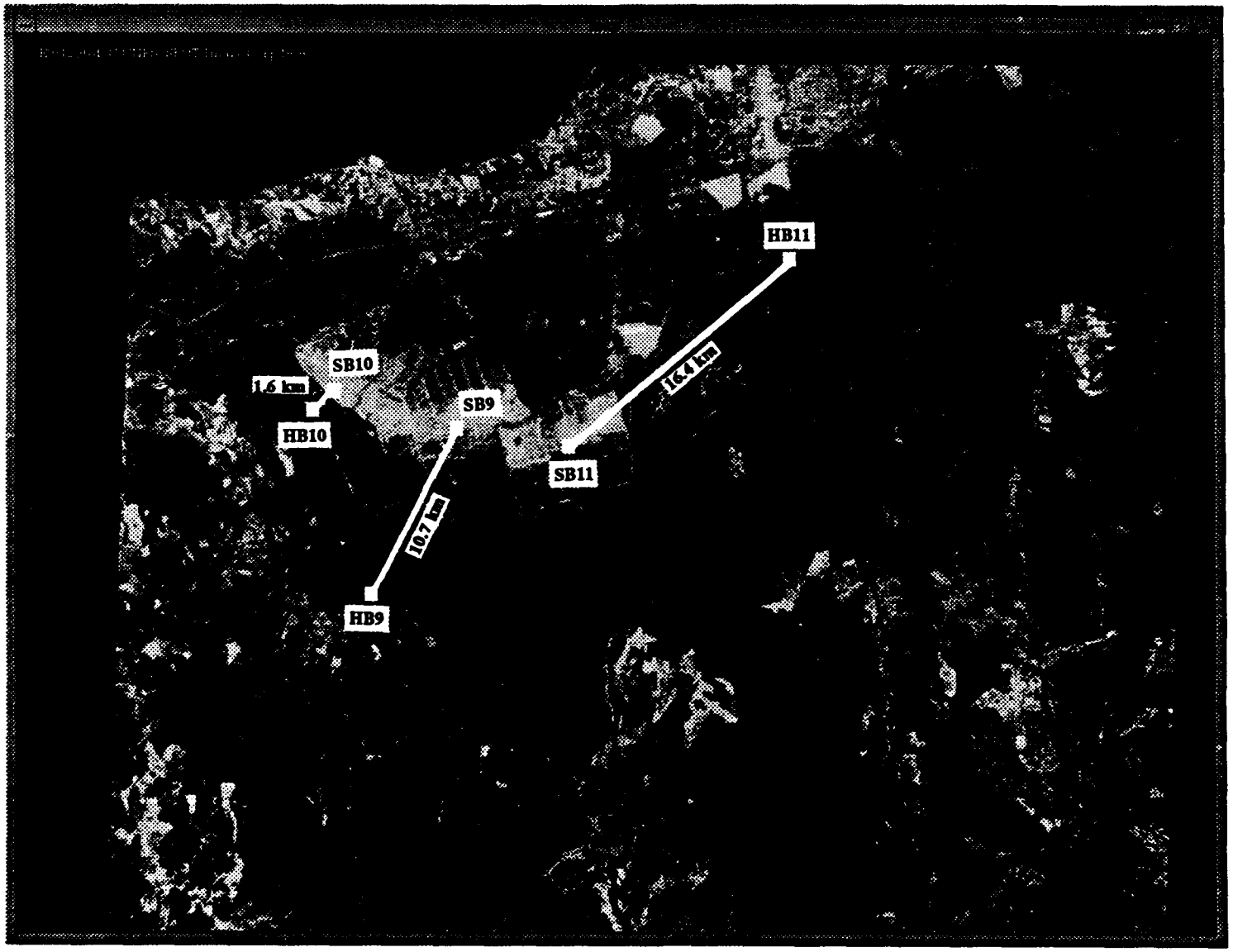

Figure 2.6. Satellite imagery for a mining region in Estonia. Three open pit oil shale mines appear near the center of the image. The mine locations determined from this image are labeled SB9, SB10, and SB11. The three nearest mine locations in the Helsinki Bulletin are labeled HB9, HB10, and HB11.

the mine site locations determined from this image are indicated. The three large open pit oil shale mines are each about 5 km in diameter. There is not a clear correspondence between these actual mine sites and the Helsinki mine locations. For example, an event identified in the Helsinki Bulletin as a mining explosion at site HB9 is just as likely to originate from any of the three open pit mines in Figure 2.6 (SB9, SB10, and SB11). Therefore, the mapping between Helsinki mine locations and mines identified on the satellite imagery (Table 2.3) is considered only to be an approximation. We actually compute arrival time difference residuals using the mine location determined from satellite imagery that minimizes the residuals for all phases (unless the residual is reduced for only one phase).

Figures 2.7–2.9 compare the arrival time difference residuals relative to the mine locations determined from satellite imagery to the residuals relative to the Helsinki mine locations. Indicated on each plot is an estimate of the arrival time standard deviation. This estimate is the standard deviation of the data in the histogram divided by $\sqrt{2}$ (i.e., assume that NORESS and ARCESS observations are independent). The arrival time standard deviation relative to the locations determined from satellite imagery is 1.0 s for *Pn*, 2.1 s for *Sn*, and 2.8 s for *Lg*. As expected, the arrival time standard deviations computed from the less accurate Helsinki mine locations are consistently higher.

The arrival time difference residual can be expressed as a sum of a measurement error and a modeling error. The measurement error can be estimated from the consistency of the arrival time difference for events in the same mine, and the modeling error can be estimated from the mean arrival time difference between NORESS and ARCESS for each mine site. We express the total arrival time variance, σ_t^2, as

$$\sigma_t^2 = \sigma_{meas}^2 + \sigma_{mod}^2 \tag{2.1}$$

where σ_{meas}^2 is the measurement variance and σ_{mod}^2 is the modeling variance. The unbiased estimate of the measurement variance is determined from the arrival time difference between NORESS and ARCESS for repeated events in the same mine. Specifically:

$$2\,\sigma_{meas}^2 = \frac{\sum_{k=1}^{Nmines} \sum_{i=1}^{Nobs} [\Delta T_{obs_{ik}} - \langle \Delta T_{obs} \rangle_k]^2}{(Nobs - Nmines)} \tag{2.2}$$

where $\Delta T_{obs_{ik}}$ is the *ith* observation of the NORESS arrival time minus the ARCESS arrival for the *kth* mine; $\langle \Delta T_{obs} \rangle_k$ is the mean arrival time difference for the *kth* mine; *Nobs* is the total number of observations (at all mines); and *Nmines* is the number of mines. The factor of two on the left side of (2.2) is based on the assumption that the measurement errors at NORESS and ARCESS are independent. Note that mines with only one observation do not contribute to the estimate of the measurement variance.

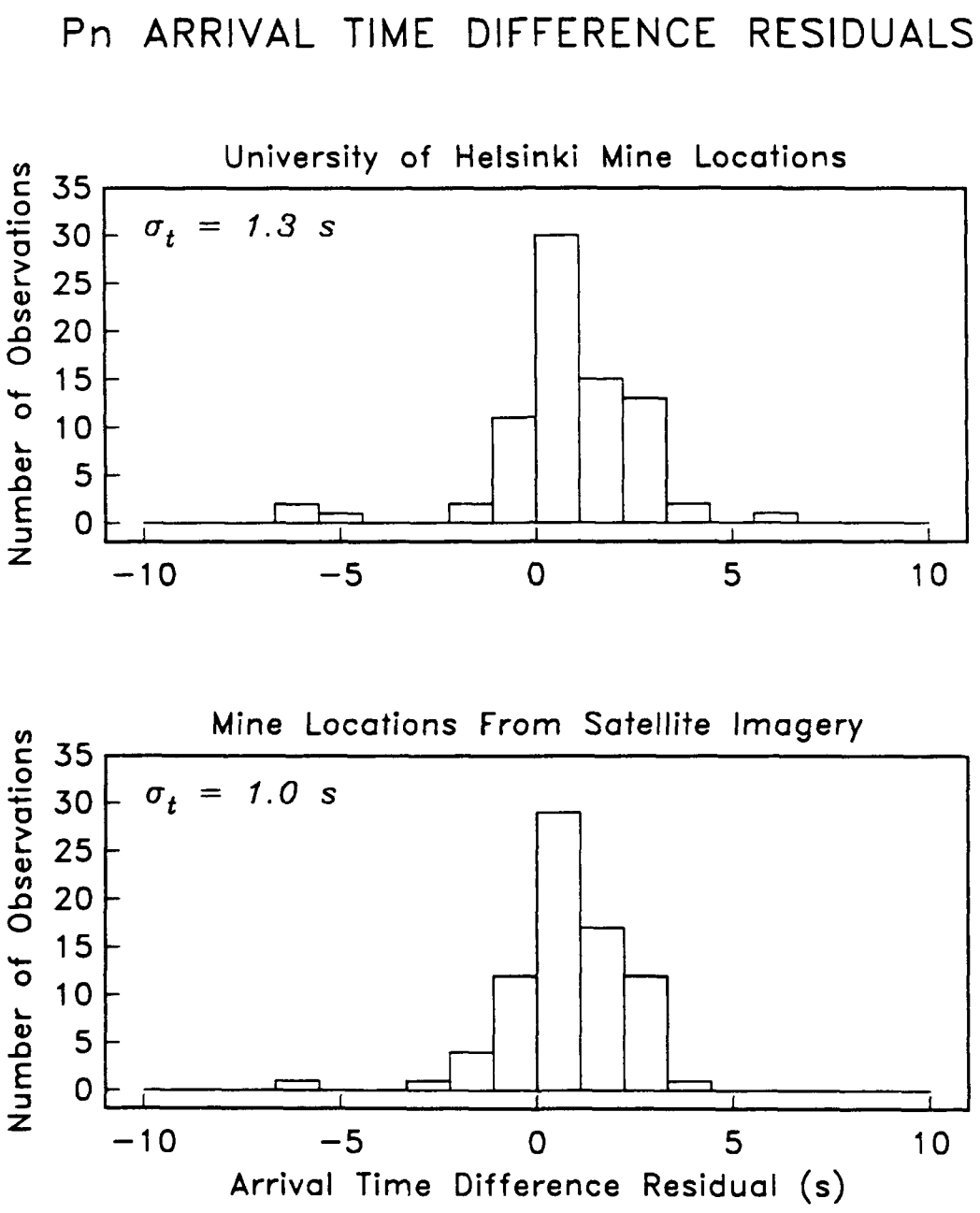

Figure 2.7. Histograms of *Pn* arrival time difference residuals. The top panel plots residuals relative to the mine locations in the Helsinki Bulletin. The lower panel plots residuals relative to the mine locations determined from satellite imagery.

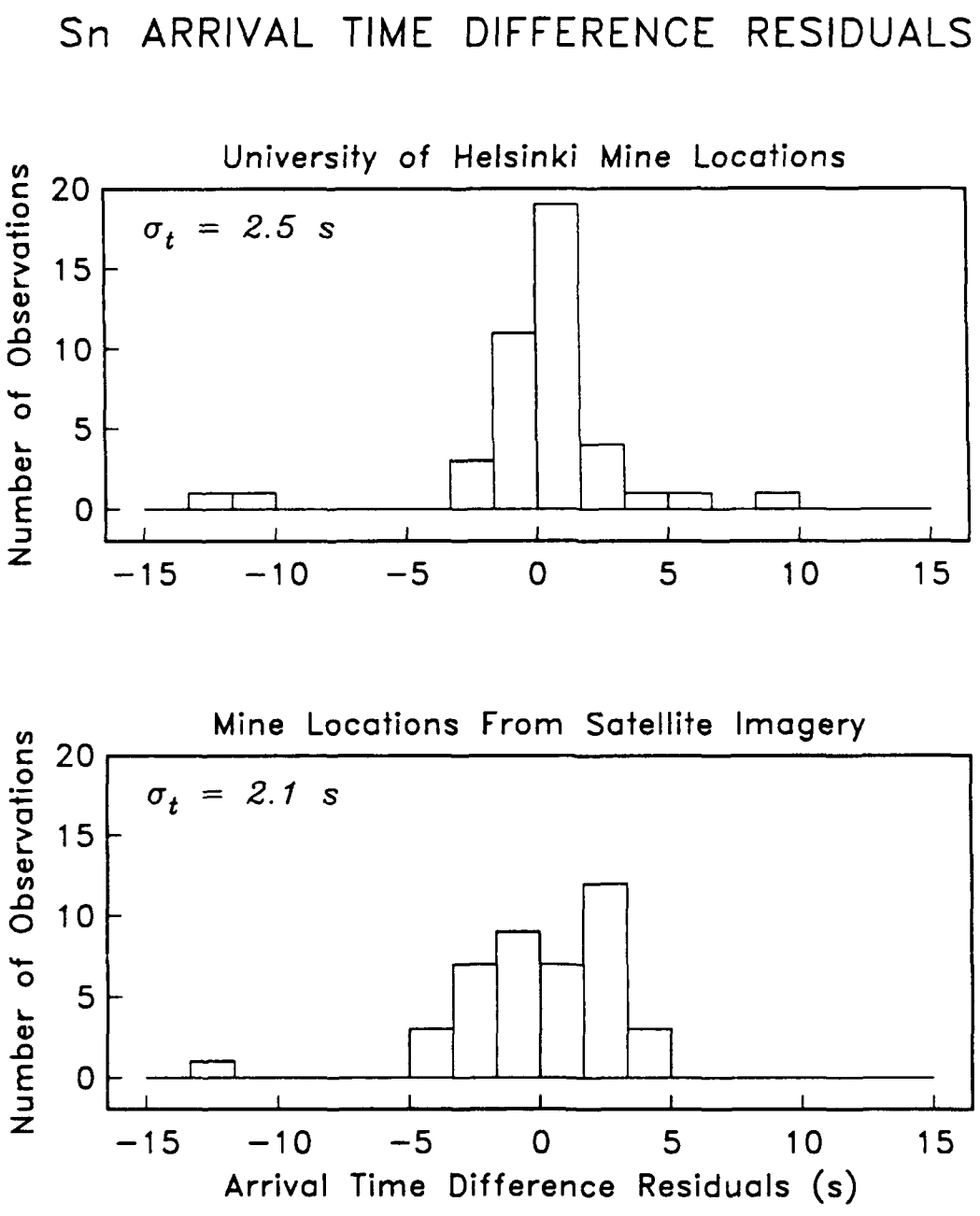

Figure 2.8. Histograms of *Sn* arrival time difference residuals. The top panel plots residuals relative to the mine locations in the Helsinki Bulletin. The lower panel plots residuals relative to the mine locations determined from satellite imagery.

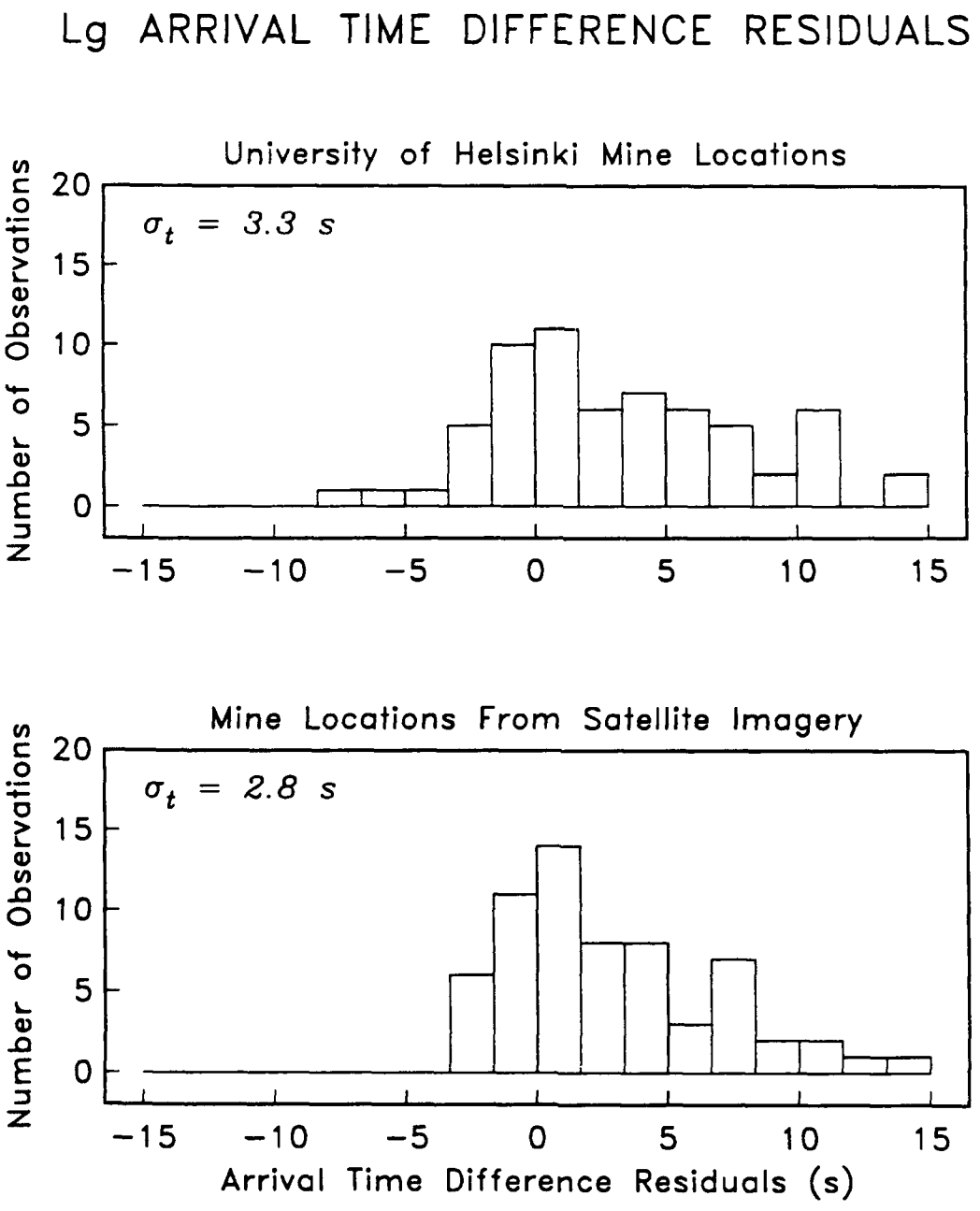

Figure 2.9. Histograms of *Lg* arrival time difference residuals. The top panel plots residuals relative to the mine locations in the Helsinki Bulletin. The lower panel plots residuals relative to the mine locations determined from satellite imagery.

The modeling errors are estimated from the mean arrival time difference for each mine and the theoretical arrival time difference computed from the *IMS* travel time tables. However, there is an uncertainty in the estimate of the mean arrival time difference for each mine that depends on the number of events in that mine. That is, the measurement variance for the mean arrival time difference for each mine ($<\Delta T_{obs}>_k$) is equal to the measurement variance for each observation ($2\sigma^2_{meas}$) divided by the number of events from that mine. To account for this we solve the following equation for the modeling variance:

$$\sum_{k=1}^{Nmines} \frac{[<\Delta T_{obs}>_k - \Delta T_k]^2}{(2\,\sigma^2_{meas} / Nev_k) + 2\,\sigma^2_{mod}} = Nmines \qquad (2.3)$$

where ΔT_k is the theoretical difference in arrival time at NORESS and ARCESS for an event at the *kth* mine site; and Nev_k is the number of events from the *kth* mine. Note that if there is only one event for a given mine, then modeling and measurement variance cannot be separated. However, if the number of events for a given mine is large, the arrival time difference residual depends only on the modeling variance.

Tables 2.4–2.6 list the mean and standard deviation, $\sigma_{\Delta T}$, of the arrival time difference between NORESS and ARCESS for up to 17 mines. The variance, $\sigma^2_{\Delta T}$, is twice the variance for individual stations (assuming the measurement errors at NORESS and ARCESS are independent). The fifth column lists the theoretical arrival time difference between the two stations, ΔT_k, and the last column is the mean arrival time difference for each mine minus the theoretical arrival time difference (e.g., the arrival time difference residuals for each mine). Table 2.7 summarizes the arrival time standard deviations for each phase. The measurement error is estimated from (2.2) using the data in Tables 2.4–2.6. The modeling error for *Pn* is estimated from (2.3). Equation (2.3) does not have a positive solution for σ^2_{mod} for *Sn* or *Lg*. Apparently the modeling error is much less than the measurement error for these phases. The total arrival time standard deviations listed in the last column of Table 2.7 are computed using (2.1). For *Sn* and *Lg* we simply assume that the modeling error is the same as the modeling error for *Pn* since it can't be resolved with these few data (this is probably a lower bound). Note that the estimates of σ_t in Table 2.7 are close to the approximate values estimated from the histograms in Figures 2.7–2.9.

We estimate the arrival time standard deviations to be 1.0 s for *Pn*, 2.2 s for *Sn*, and 2.5 s for *Lg*. These estimates for *Sn* and *Lg* are similar to the results obtained from the much larger *IMS* database (Section 2.3.1), but the *Pn* estimate is significantly higher. This indicates that the *Pn* residuals computed relative to the *IMS* locations are biased low (as was expected from the "a priori" standard deviations used by the location algorithm). Our estimates of the arrival time standard deviations for *Sn* and *Lg* are about 0.3–0.4 s lower than estimates reported by *Bratt et al.* [1990]. This is probably because they computed residuals relative to the Helsinki mine locations (this is the approximate difference between the standard deviations that we computed relative to the Helsinki locations and the locations determined from satellite imagery).

Table 2.4 *Pn* arrival time difference residuals relative to locations determined from satellite imagery.

Mine ID	Nev_k	$\langle \Delta T_{obs} \rangle_k$	$\sigma_{\Delta T}$	ΔT_k	$\langle \Delta T_{obs} \rangle_k - \Delta T_k$
SB5	6	-33.2	0.4	-34.5	1.3
SB6	13	-31.2	1.0	-32.0	0.8
SB9	4	-26.8	1.1	-28.4	1.6
SB10	1	-30.3	–	-28.7	-1.6
SB11	2	-26.7	0.5	-28.1	1.4
SB13	3	-20.7	0.3	-23.3	2.6
SC1	1	-7.7	–	-6.3	-1.4
SC2	3	-7.8	2.9	-4.9	-2.9
SC3	2	-6.7	1.1	-6.9	0.2
SC4	2	-2.5	1.9	-4.3	1.8
SC5	1	-2.4	–	-2.1	-0.3
SC6	3	-1.8	0.5	-2.0	0.2
SC7	6	-1.3	0.8	-1.6	0.3
SC11	1	4.8	–	4.0	0.8
SC15	4	31.8	1.8	30.8	1.0
SC17	11	60.5	0.8	58.4	2.1
SD2	14	134.4	0.6	134.3	0.1

Table 2.5 *Sn* arrival time difference residuals relative to locations determined from satellite imagery.

Mine ID	Nev_k	$\langle \Delta T_{obs} \rangle_k$	$\sigma_{\Delta T}$	ΔT_k	$\langle \Delta T_{obs} \rangle_k - \Delta T_k$
SB5	8	-59.2	1.4	-60.6	1.4
SB6	9	-55.8	2.1	-56.2	0.4
SB9	2	-49.6	0.1	-50.0	0.4
SB10	1	-55.1	–	-50.5	-4.6
SB11	1	-46.4	–	-49.4	3.0
SC2	2	-8.7	2.5	-8.6	-0.1
SC3	1	-14.0	–	-12.2	-1.9
SC4	1	-11.5	–	-7.5	-4.0
SC5	1	-6.5	–	-3.7	-2.8
SC6	1	-5.5	–	-3.5	-2.0
SC7	4	-3.7	1.9	-2.9	-0.8
SC11	1	9.8	–	7.1	2.7
SC15	2	54.6	5.5	54.2	0.4
SC17	7	101.8	4.9	102.7	-0.9
SD2	1	236.6	–	236.2	0.4

Table 2.6 *Lg* arrival time difference residuals relative to locations determined from satellite imagery.

Mine ID	Nev_k	$\langle \Delta T_{obs} \rangle_k$	$\sigma_{\Delta T}$	ΔT_k	$\langle \Delta T_{obs} \rangle_k - \Delta T_k$
SB5	8	-79.3	3.2	-80.0	0.7
SB6	12	-72.4	3.3	-74.1	1.7
SB9	5	-66.5	0.9	-65.9	-0.6
SB10	2	-58.8	7.9	-66.6	7.8
SB11	2	-62.7	3.7	-65.1	2.4
SB13	2	-49.9	4.3	-54.0	4.1
SC1	1	-13.2	–	-14.6	1.4
SC2	3	-7.0	6.2	-11.4	4.4
SC3	2	-8.1	0.2	-16.1	8.0
SC4	1	-10.4	–	-9.9	-0.5
SC5	1	2.6	–	-4.9	7.5
SC6	2	5.6	2.4	-4.6	10.2
SC7	6	0.8	2.0	-3.8	4.6
SC11	1	13.6	–	9.4	4.2
SC15	3	75.1	0.9	71.4	3.7
SC17	7	138.8	4.3	135.4	3.4
SD2	5	311.9	3.1	310.3	1.6

Table 2.7 Summary of arrival time residuals relative to locations determined from satellite imagery.

Phase	# Observations	# Mines	σ_{meas} (s)	σ_{mod} (s)	σ_t (s)
Pn	77	17	0.7	0.7	1.0
Sn	42	15	2.1	0.7†	2.2
Lg	63	17	2.4	0.7†	2.5

† Assumed values.

However, their estimates of *Pn* arrival time standard deviation are much larger than ours (2.5 s at NORESS and 1.9 s at ARCESS). We don't know why this difference is so large, but it may be related to the average *snr* of *Pn* arrivals in the two data sets.

2.4 Summary

The estimated azimuth and arrival time standard deviations for regional phases recorded by NORESS and ARCESS are summarized in Table 2.8. The arrival time variance for *Pg* is assumed to be the same as the variance for *Pn* since we don't have enough data to estimate it with confidence. The arrival time variance for each of the other phases is estimated in two ways: (1) relative to the *IMS* locations and origin times, and (2) relative to mine locations determined from satellite imagery. These methods give similar results for *Sn* and *Lg* (we find that the uncertainty in arrival time for these phases is dominated by measurement error), but the results for *Pn* are different. We attribute this difference to a bias in the *Pn* arrival time residuals relative to the *IMS* locations.

Thomas J. Sereno, Jr.
Henry J. Swanger
Donna J. Williams

Table 2.8 Summary of arrival time and azimuth standard deviation for regional phases.

Phase	σ_α (°)	*IMS* Locations σ_t (s)	Satellite Imagery σ_t (s)
Pn	7.0	0.7	1.0
Pg	5.9	0.7	1.0†
Sn	7.0	2.3	2.2
Lg	7.1	2.3	2.5

† Assumed value.

(THIS PAGE INTENTIONALLY LEFT BLANK)

3. GENERALIZED INVERSION

Estimates of frequency-dependent source and attenuation parameters for regional phases are needed to simulate the detection capability of seismic networks that include regional stations and arrays. We estimate these parameters using regional wave spectra for *Pn*, *Pg*, *Sn*, and *Lg* recorded at NORESS and ARCESS with generalized inverse techniques. In a previous project we used a similar method to estimate *Pn* and *Lg* attenuation for paths to NORESS [*Sereno et al.*, 1988]. However, it was not possible to resolve trade-offs among source and attenuation parameters using data recorded by only one station. In this study, parameter trade-off resolution is improved by including spectra from four regional phases recorded by two arrays. With the improved parameter trade-off resolution, we improve upon our previous results for *Pn* and *Lg* and add estimates of frequency-dependent *Pg* and *Sn* attenuation in Fennoscandia.

3.1 Method

The instrument-corrected amplitude spectrum $A_{ijk}(f)$ of the *kth* wave recorded at the *ith* station from the *jth* source is parameterized as

$$\log A_{ijk}(f) = \log A^0_{jk}(f) + B_k(\Delta_{ij}, \Delta^0, f) + \delta_{ik} \tag{3.1}$$

where $A^0_{jk}(f)$ is the amplitude spectrum at a reference distance Δ^0, $B_k(\Delta_{ij}, \Delta^0, f)$ is the attenuation from the reference distance to the epicentral distance Δ_{ij}, and δ_{ik} is a station correction. The amplitude, A^0_{jk}, is expressed in terms of source parameters as

$$\log A^0_{jk}(f) = \log S_{0j} + \log s_j(f) + \log \kappa_k + \gamma_k \log f \tag{3.2}$$

where S_{0j} is the long-period level (proportional to seismic moment), $s_j(f)$ is the shape of the source spectrum, κ_k is a wave-dependent excitation factor, and γ_k accounts for different pulse shapes of crustal and mantle phases at the reference distance. For example, if the reference distance is close to the critical distance, then *Pn* and *Sn* can be approximated as head waves at Δ^0 and their pulse shapes are integrals of the direct or turning rays [e.g., *Aki and Richards*, 1980]. Therefore, γ_k is set to -1 for *Pn* and *Sn*, and it is set to zero for *Pg* and *Lg*.

The source spectrum is assumed to decay as f^{-2} beyond a corner frequency that scales inversely with the cube root of the long-period level. We use the explosion source model from *Mueller and Murphy* [1971]. The source spectrum is parameterized as

$$s(f) = \frac{f_c{}^2}{[f_c{}^4 + (1 - 2\beta) f_c{}^2 f^2 + \beta^2 f^4]^{1/2}} \tag{3.3}$$

$$f_c = cS_0^{-1/3} \tag{3.4}$$

where f_c is the corner frequency, c is a scaling parameter that relates corner frequency and long-period level for all events in the data set, and β determines the amount of overshoot [*Mueller and Murphy*, 1971]. Figure 3.1 plots a family of these source spectra for $\beta = 0.6$ (which is the value we used for the inversion). Seismic moment M_0 can be estimated from the long-period level using

$$M_0 = \frac{S_0\, 4\pi\, (\rho_s\, \rho_r\, v_s^5\, v_r)^{1/2}\, G(\Delta^0)}{F\, R\, V} \tag{3.5}$$

where F is the free-surface amplification, R is the radiation pattern, V is the vector wavefield decomposition, ρ_r and ρ_s are the densities at the receiver and source, respectively, v_r and v_s are the compressional wave velocities at the receiver and source, respectively, and $G(\Delta^0)$ is the geometrical spreading at the reference distance.

The attenuation is parameterized in terms of a power law distance dependence with a frequency-dependent exponent. Our previous parameterization included geometrical spreading and anelasticity as separate terms [*Sereno et al.*, 1988]. That is, we assumed that the geometrical spreading was independent of frequency, and that it could be described by a power law distance dependence. However, the geometrical spreading of *Pn* and *Sn* are known to be frequency-dependent, even for very simple models of the upper mantle [e.g., *Sereno and Given*, 1990]. Since this complicated geometrical spreading is not accurately known for regional phases and separating it from anelasticity is not necessary to simulate detection capability, we parameterize the total attenuation (both geometrical spreading and anelasticity) as

$$B_k(\Delta_{ij}, \Delta^0, f) = -\log e\ \alpha_k^0 f + n_k(f) \log(\Delta_k^0 / \Delta_{ij}) \tag{3.6}$$

$$n_k(f) = a_k f + b_k \tag{3.7}$$

where the first term in (3.6) accounts for anelastic attenuation from the source to the reference distance, and the second term describes the total attenuation from the reference distance to Δ_{ij}. *Chun et al.* [1989] used this parameterization to estimate *Pn* attenuation in the Canadian Shield.

Of course, it is possible that the attenuation of regional phases cannot be accurately represented by a power law at any frequency. In fact *Pn* and *Sn* amplitude may increase over limited distance ranges (depending on the velocity gradient in the upper mantle). To check this, we plotted log amplitude minus magnitude (from the Helsinki Bulletin) as a function of distance for each phase at several frequencies. This is within a constant scale factor of $B(\Delta)$ if log moment scales linearly with magnitude, and if the frequencies considered are less than the event corner frequency. Figure 3.2 shows examples of these plots for *Pn* and *Sn* at 5.0 Hz, and *Lg* at 2.0 Hz. A power law

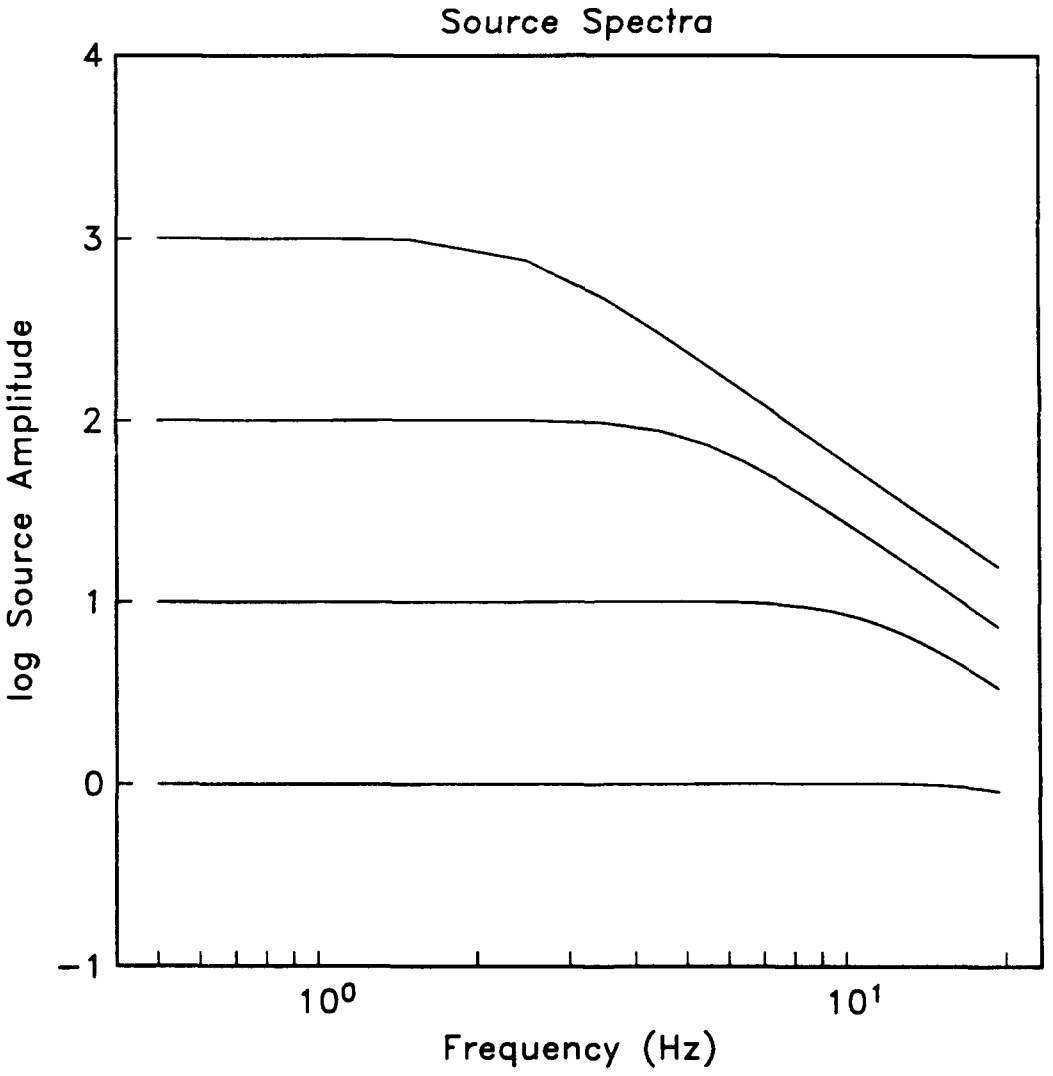

Figure 3.1. Explosion source spectra defined by (3.3) and (3.4).

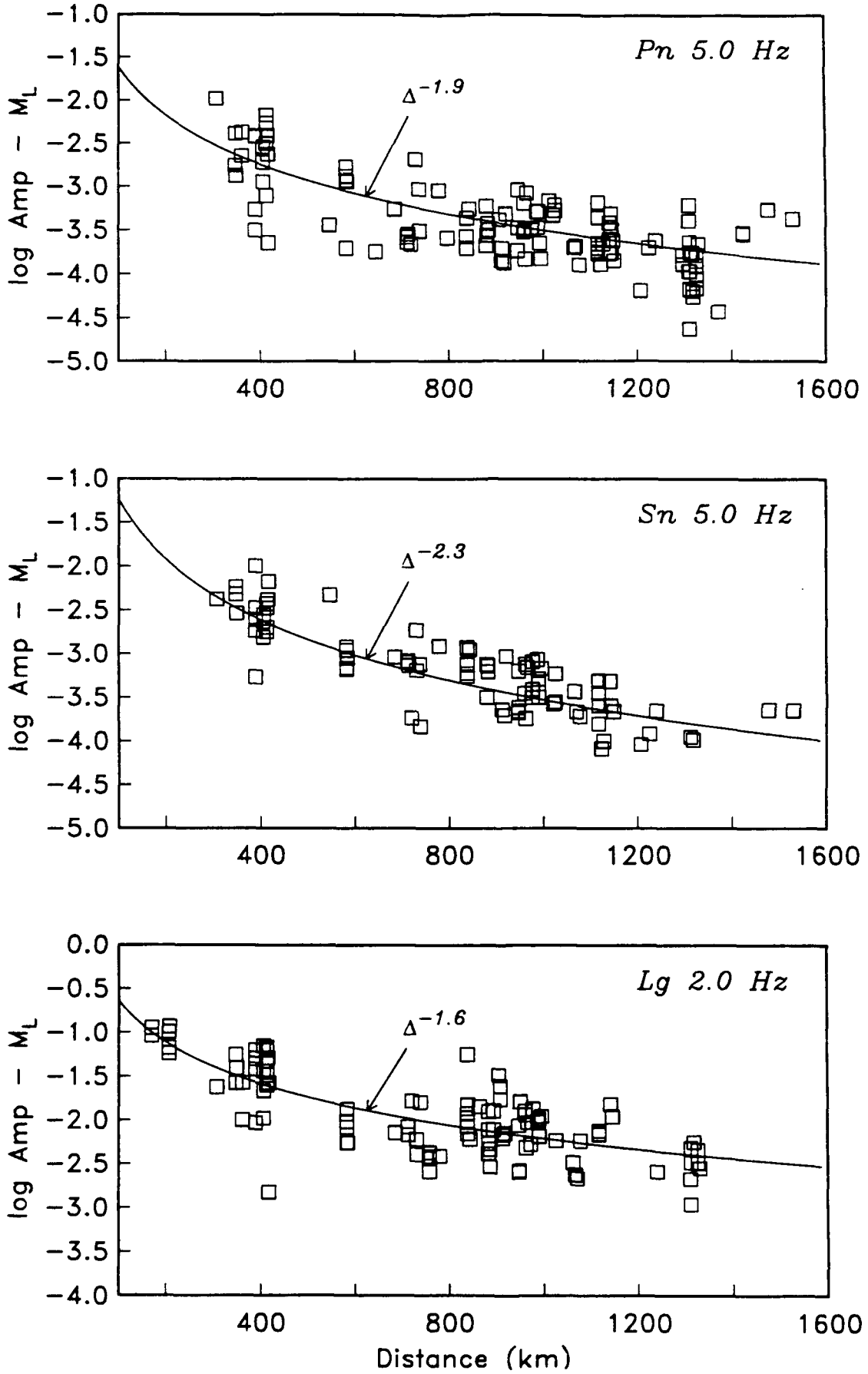

Figure 3.2. Approximate *Pn* and *Sn* attenuation at 5.0 Hz (top two panels) and *Lg* attenuation at 2.0 Hz (bottom panel). This approximate attenuation is defined as log amplitude minus event magnitude. The attenuation of each phase is compared to a power law distance dependence.

approximation to the attenuation is superimposed as a solid curve in each panel These plots suggest that a parameterization such as (3.6) is adequate to describe the attenuation of regional phases in Fennoscandia.

The system of equations governing the relationship between the data (log amplitude spectra) and model parameters is linearized by subtracting theoretical data (computed from an assumed starting model) from the observed data and solving iteratively for the model perturbations that minimize the data residuals in the least squares sense. We express the relationship between the data residuals, Δd, and model perturbations, Δm, as

$$\Delta d = \boldsymbol{A}\, \Delta m \tag{3.8}$$

where $\boldsymbol{A}$ is a matrix of partial derivatives of the log amplitude spectra with respect to the model parameters. The source parameters estimated by the inversion are the long-period level for each event, S_{0j}, the corner frequency scaling parameter,c, and the excitation factor for each wave, κ_k. The attenuation parameters for each wave are α_k^0, a_k and b_k from (3.6) and (3.7). The station corrections are determined relative to a reference station. The absolute corrections are obtained by applying the constraint that the sum of the station corrections is zero for each wave. Figure 3.3 lists the analytical form of the partial derivatives of the log amplitudes with respect to each model parameter (e.g., the elements of the matrix $\boldsymbol{A}$).

The system of equations defined by (3.8) is overdetermined. The damped least squares solution for damping factor λ is

$$\Delta m = (\boldsymbol{A}^T\boldsymbol{A} + \lambda I)^{-1}\, \boldsymbol{A}^T \Delta d \tag{3.9}$$

where I is the identity matrix. In practice we find it necessary to include damping to stablize the solution (at least for the first few iterations). However, the damping factor can be set to zero for the final iterations and the solution converges to the solution given by the normal equations. To avoid "ill-conditioning" caused by different scales in the model parameters, each column of the matrix $\boldsymbol{A}$ is normalized as

$$A_{ij} = \frac{A_{ij}}{\left[\sum_{i=1}^{N} A_{ij}^2\right]^{1/2}} \tag{3.10}$$

where N is the number of data used in the inversion. Of course, the model parameters estimated using the normalized matrix, $\boldsymbol{A}$, must also be divided by the denominator in (3.10).

PARTIAL DERIVATIVES

SOURCE

$$\frac{\partial \log A(f)}{\partial \log S_0} = 1 - \frac{S_0}{3}\left[\frac{2\,\beta^2 f^4 S_0^{1/3} + (1-2\beta)\,c^2 f^2 S_0^{-1/3}}{c^4 + (1-2\beta)\,c^2 f^2 S_0^{2/3} + \beta^2 f^4 S_0^{4/3}}\right]$$

$$\frac{\partial \log A(f)}{\partial c} = \frac{2\log e}{c}\left[1 - \left[\frac{2c^3 + (1-2\beta)\,c f^2 S_0^{2/3}}{c^4 + (1-2\beta)\,c^2 f^2 S_0^{2/3} + \beta^2 f^4 S_0^{4/3}}\right]\right]$$

$$\frac{\partial \log A(f)}{\partial \log \kappa} = 1$$

ATTENUATION

$$\frac{\partial \log A(f)}{\partial \alpha^0} = -\log e\, f$$

$$\frac{\partial \log A(f)}{\partial a} = f \log (\Delta^0 / \Delta)$$

$$\frac{\partial \log A(f)}{\partial b} = \log (\Delta^0 / \Delta)$$

STATION CORRECTIONS

$$\frac{\partial \log A(f)}{\partial \delta} = 1$$

Figure 3.3. Analytical form of the partial derivatives of the data (log amplitudes) with respect to each model parameter.

3.2 Data

The data are array-averaged log amplitude spectra computed from regional phases recorded at NORESS and ARCESS from 97 regional events that occurred between November 1987 and April 1988. Each event is reported in the Helsinki Bulletin. The magnitudes range from 2.0 to 3.6, and the epicentral distances are 200 to 1600 km. Table 3.1 lists the event parameters and Figure 3.4 displays the epicenters on a map. The mine codes in Table 3.1 are labels that we assigned to the mine locations given in the Helsinki Bulletin. The events include 82 mining explosions, 3 earthquakes, and 12 events of unknown origin (these are probably explosions).

3.2.1 Data Processing

The first step in the data processing is the interactive picking of regional phases. We start with the event location given in the Helsinki Bulletin. Theoretical arrival times of regional phases are displayed on filtered traces recorded at NORESS and ARCESS using the *Seismic Analysis Code* (*SAC*) developed by J. Tull at Lawrence Livermore National Laboratories. The theoretical arrival times are used as a guide for interactive picking of regional *Pn*, *Pg*, *Sn*, and *Lg* phases. In addition, we use the signal processing module of the *IMS* to estimate phase velocity and azimuth for each detection [*Bache et al.*, 1990a]. The dominant period and array-averaged time domain amplitude are estimated for each phase.

Next, the array-averaged signal and noise spectra are computed for each phase [*Bache et al.*, 1985]. A 10% cosine taper is applied to each vertical component waveform prior to computing the spectra. In most cases the *Pn*, *Pg*, and *Sn* spectra are computed for a 10-s window starting 0.3 s before the arrival time. For close events, where *Pn* and *Pg* or *Sn* and *Lg* arrive within the same 10-s window, the *Pn* and *Sn* spectra are computed for a shorter time window that depends on group velocity to exclude the later phase. The *Lg* spectra are computed for a fixed group velocity window 3.0–3.6 km/s starting 0.3 s before picked arrival time. The noise spectra are computed for a 5-s window starting 5.5 s before each signal window. These noise spectra are normalized to the signal window length, and they are used to estimate the *snr* as a function of frequency. Frequencies for which this *snr* exceeds several pre-determined thresholds (2.0, 3.5, 6.0, 8.0, and 9.5 dB) are determined for each phase.

The signal spectra are inverted for source and attenuation parameters. The frequency bands considered are 1–15 Hz for *Pn* and *Pg*, 1–10 Hz *Sn*, and 0.5–7 Hz for *Lg*. However, the *snr* (where the noise for secondary phases includes the coda of previous arrivals) is required to be above one of the pre-selected thresholds for each phase. The results presented here are for thresholds of 3.5 dB for *Pn* and *Sn* and 2.0 dB for *Pg* and *Lg*. The spectra are sampled every 0.25 Hz for each phase. The total number of data used in the inversion is 10,801 and the number of parameters is 114.

Table 3.1 Events used in the generalized inversion.

Event	Date	Origin Time	Location Lat (°N)	Location Lon (°E)	Type	Mine Code	M_L
1	1-18-88	12:18:36	59.50	26.50	CHEM	HB5	2.7
2	1-20-88	12:43:39	69.40	30.80	CHEM	HD2	2.7
3	1-20-88	13:14:06	61.40	31.60	CHEM	HC14	2.7
4	1-29-88	12:07:47	64.70	30.70	CHEM	HC17	2.8
5	1-29-88	12:54:34	69.60	29.90	CHEM	HF1	3.0
6	3-15-88	11:34:36	59.50	26.50	CHEM	HB5	2.5
7	1-15-88	16:03:03	67.60	34.20	CHEM	HD10	3.1
8	1-16-88	12:39:04	68.10	33.20	CHEM	HD6	2.8
9	1-19-88	11:50:50	59.30	24.40	CHEM	HB1	2.5
10	1-19-88	11:55:35	59.30	27.20	CHEM	HB6	2.5
11	1-20-88	12:23:06	59.30	27.20	CHEM	HB6	2.5
12	1-20-88	13:20:39	61.90	30.60	CHEM	HC13	2.7
13	1-23-88	13:04:03	62.93	34.82			2.6
14	1-29-88	11:43:38	67.60	34.20	CHEM	HD10	3.0
15	1-29-88	13:22:35	61.67	31.32			2.7
16	1-31-88	10:47:48	68.10	33.20	CHEM	HD6	2.8
17	2- 3-88	11:33:11	61.10	30.20	CHEM	HC11	2.9
18	2- 3-88	12:02:07	63.20	27.80	CHEM	HA15	2.5
19	2-12-88	9:29:28	69.20	33.30	CHEM	HD7	2.6
20	2-12-88	11:15:04	60.80	29.30	CHEM	HC4	2.5
21	2-12-88	11:42:40	67.60	34.20	CHEM	HD10	2.9
22	2-16-88	12:45:49	60.70	29.00	CHEM	HC2	2.8
23	2-22-88	12:23:01	59.50	26.50	CHEM	HB5	2.6
24	2-24-88	9:31:46	61.10	29.90	CHEM	HC10	2.8
25	2-25-88	10:13:26	61.10	29.90	CHEM	HC10	2.6
26	2-26-88	12:12:34	64.70	30.70	CHEM	HC17	2.9
27	2-26-88	12:31:20	59.50	25.00	CHEM	HB3	2.5
28	2-26-88	14:36:51	61.65	31.41			2.7
29	2-27-88	9:01:49	68.10	33.20	CHEM	HD6	2.8
30	1-11-88	11:56:18	59.50	26.50	CHEM	HB5	2.3
31	1-15-88	9:25:50	67.60	34.00	CHEM	HD9	2.0
32	1-15-88	11:25:34	61.40	34.30	CHEM	HC15	2.5
33	1-15-88	12:33:38	69.40	30.80	CHEM	HD2	2.4
34	1-16-88	12:24:26	61.90	30.60	CHEM	HC13	2.4
35	1-18-88	9:44:19	59.30	27.60	CHEM	HB10	2.5
36	1-18-88	12:04:55	59.30	27.20	CHEM	HB6	2.3
37	1-19-88	9:31:25	59.30	27.60	CHEM	HB10	2.3
38	1-19-88	12:09:04	63.20	27.80	CHEM	HA15	2.4
39	1-20-88	10:00:21	64.70	30.70	CHEM	HC17	2.4

Event	Date	Origin Time	Location Lat (°N)	Location Lon (°E)	Type	Mine Code	M_L
40	1-25-88	13:57:06	60.70	29.00	CHEM	HC2	2.5
41	1-26-88	12:54:14	67.60	30.50	CHEM	HD1	2.4
42	1-27-88	13:27:00	60.90	29.30	CHEM	HC5	2.3
43	1-28-88	12:42:58	59.50	26.50	CHEM	HB5	2.5
44	1-29-88	9:25:12	60.90	29.40	CHEM	HC6	2.3
45	1-31-88	3:31:36	67.60	34.00	CHEM	HD9	2.5
46	2- 5-88	10:00:52	64.70	30.70	CHEM	HC17	2.3
47	2- 9-88	12:36:18	59.30	27.60	CHEM	HB10	2.3
48	3- 3-88	17:37:52	72.56	13.52	EQ		3.1
49	3-15-88	10:31:30	59.24	27.37			2.5
50	3-15-88	14:20:59	60.93	29.19			2.4
51	3-20-88	14:39:35	70.69	-6.59	EQ		3.6
52	11-15-87	3:55:58	67.70	33.70	CHEM	HD8	3.2
53	11-18-87	10:25:19	61.50	30.40	CHEM	HC12	2.9
54	11-18-87	19:59:51	65.80	24.70	CHEM	HA25	2.0
55	12-23-87	12:39:49	59.60	30.00	CHEM	HB16	2.4
56	12-23-87	12:48:45	59.40	28.50	CHEM	HB13	2.0
57	12-23-87	12:59:30	69.40	30.80	CHEM	HD2	3.1
58	12-25-87	9:46:51	61.90	30.60	CHEM	HC13	2.4
59	12-25-87	11:59:59	59.50	26.50	CHEM	HB5	2.0
60	12-25-87	12:03:54	67.60	34.20	CHEM	HD10	2.9
61	12-25-87	12:12:45	61.40	31.60	CHEM	HC14	2.6
62	12-25-87	13:34:35	60.90	29.40	CHEM	HC6	2.4
63	1- 8-88	11:57:56	67.60	34.00	CHEM	HD9	
64	1- 9-88	11:22:29	67.60	30.50	CHEM	HD1	
65	2- 6-88	10:53:22	67.60	30.50	CHEM	HD1	
66	2- 6-88	11:03:50	68.10	33.20	CHEM	HD6	
67	2-14-88	6:03:07	67.70	33.70	CHEM	HD8	2.5
68	2-16-88	12:45:49	60.70	29.00	CHEM	HC2	2.8
69	3- 5-88	9:55:17	67.60	34.20	CHEM	HD10	2.9
70	3- 5-88	10:51:10	59.50	26.50	CHEM	HB5	2.6
71	3-14-88	13:10:52	59.50	25.00	CHEM	HB3	2.6
72	3-16-88	11:45:36	63.20	27.80	CHEM	HA15	2.5
73	3-17-88	10:21:17	69.60	29.90	CHEM	HF1	2.9
74	3-18-88	5:16:20	69.20	34.70	CHEM	HD12	2.6
75	3-18-88	10:37:01	67.60	34.00	CHEM	HD9	2.6
76	3-18-88	12:35:55	69.40	30.80	CHEM	HD2	2.7
77	4- 1-88	7:57:35	67.60	34.20	CHEM	HD10	2.9
78	4- 1-88	8:26:54	59.50	25.00	CHEM	HB3	2.5
79	4- 2-88	9:00:00	64.70	30.70	CHEM	HC17	2.6
80	4- 3-88	3:47:07	67.70	33.70	CHEM	HD8	2.8
81	4- 6-88	11:29:11	59.30	27.20	CHEM	HB6	2.6
82	4-14-88	17:20:07	69.20	34.70	CHEM	HD12	2.9

Event	Date	Origin Time	Location Lat (°N)	Location Lon (°E)	Type	Mine Code	M_L
83	4-17-88	4:17:35	67.70	33.70	CHEM	HD8	2.9
84	4-21-88	6:24:06	59.45	24.29			3.0
85	4-22-88	11:11:15	59.40	24.60	CHEM	HB2	3.1
86	4-22-88	11:40:13	61.40	34.30	CHEM	HC15	2.5
87	4-24-88	5:22:23	67.60	34.00	CHEM	HD9	2.9
88	4-24-88	21:12:51	67.88	10.15	EQ		3.3
89	4-26-88	9:11:41	59.22	23.49			2.8
90	4-28-88	9:29:52	59.30	27.20	CHEM	HB6	2.5
91	4-28-88	9:36:18	58.98	18.15			3.0
92	4-28-88	10:36:48	59.50	25.00	CHEM	HB3	2.5
93	4-28-88	12:22:09	55.92	21.26			2.8
94	4-29-88	12:50:27	61.68	31.33			2.7
95	4-29-88	15:36:39	56.40	21.02			3.0
96	4-29-88	15:41:26	56.34	21.07			2.9
97	4-30-88	20:20:26	67.70	33.70	CHEM	HD8	2.6

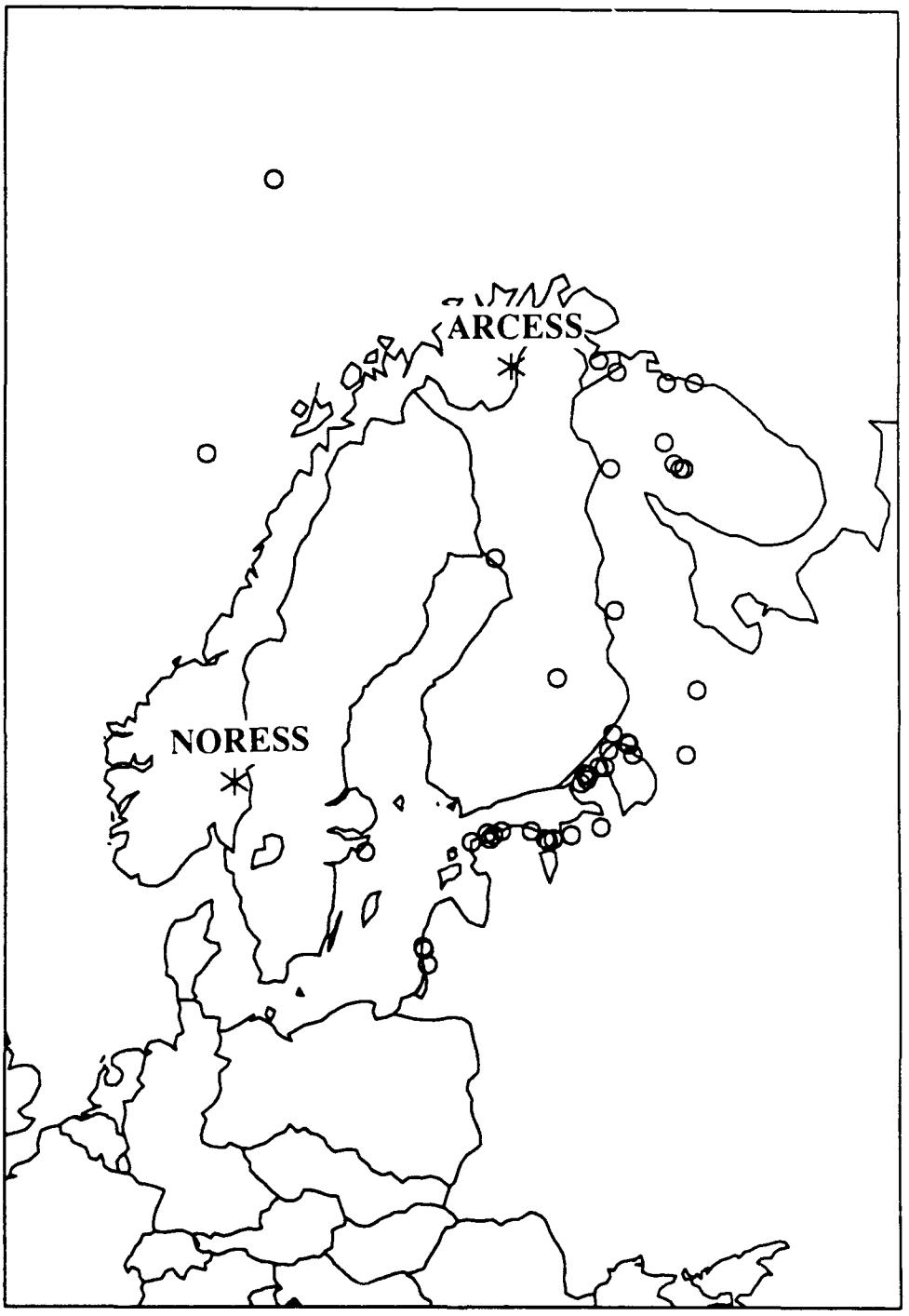

Figure 3.4. The epicenters of events used in the inversion are plotted using event locations from a bulletin produced by the University of Helsinki.

3.3 Attenuation of Regional Phases

The attenuation parameters and station corrections for each phase are listed in Table 3.2. Figures 3.5–3.8 plot the attenuation, $B(\Delta)$, for each wave at several frequencies. *Lg* attenuation has the strongest frequency dependence, and *Pg* attenuates more rapidly with distance than the other phases. Note that meaningful estimates of *Pg* attenuation are obtained from the relatively few data because the source parameters are constrained by spectra for other phases. Also, *Sn* attenuates more rapidly with distance than *Pn*, and it has a stronger frequency dependence. This suggests that the anelastic attenuation is greater for shear waves than for compressional waves in the upper mantle. The small values of α^0 for *Pn* and *Sn* indicate that the shape of these spectra at the reference distance (200 km) are very similar to the shape of the source spectrum. The larger values of α^0 for *Pg* and *Lg* indicate greater attenuation of these phases from the source to the reference distance. Similar results are obtained if the station corrections are constrained to be zero for each phase (Table 3.3). Appendix A gives examples of the fit to the observed spectra for several events recorded at distances between 200 and 1600 km.

The attenuation estimates for *Pn* and *Lg* presented here are lower than the preferred model presented in our earlier paper where a similar method was used for data recorded at one array [*Sereno et al.*, 1988]. For example, Figure 3.9 plots theoretical *Pn* and *Lg* spectra at 400 km and 1000 km for this previous attenuation model and for our current attenuation model. Note that the maximum frequency considered for *Lg* was 7 Hz, so that differences beyond that are not meaningful. The "preferred" model from *Sereno et al.* [1988] was one of a suite of models that fit the data with nearly equal fidelity. There are other models in the suite with lower attenuation and lower source amplitudes that are similar to the model derived here with the more complete data set. Figure 3.9 also plots theoretical spectra for the *Pn* attenuation model derived by *Chun et al.* [1989] for the Canadian Shield. They parameterize total *Pn* attenuation as $\Delta^{-n(f)}$, and they estimate $n(f) = 0.02\,f + 2.2$. Their model gives spectra that are nearly identical to ours at 400 km, but that differ at 1000 km because of the weaker frequency dependence of their *Pn* attenuation model.

3.4 Source Parameters

The source parameters are the long-period level for each event, S_0, the corner frequency scaling parameter, c, and the excitation factor for each wave, κ. The long-period levels are plotted versus the magnitude in the Helsinki Bulletin in Figure 3.10. The solid line indicates the least-squares linear fit assuming the slope is one, and the dashed lines indicate one standard deviation (0.17). Seismic moment is estimated from the long-period level using (3.5) and assuming the near-surface density is 2500 kg/m^3, the compressional-wave velocity is 5000 m/s, $G(\Delta^0) = \Delta^0$, and $F\,R\,V = 1$. This gives $\log M_0 = M_L + 17.2$, which is generally consistent with results obtained from near-field studies [e.g., *Bungum et al.*, 1982; *Hasegawa*, 1983]. The corner frequency scaling parameter is estimated to be 24.1, which means that an M_L 3.0 event has an approximate corner frequency of 9 Hz. The long-period level and corner frequency are listed

Table 3.2 Attenuation parameters and station corrections.

Phase	# Data	Δ^0 (km)	α (s)	$n(f) = af + b$ a	b	Station Corrections† NORESS	ARCESS
Pn	5827	200	-0.02	0.072	1.40	-0.03	0.03
Pg	954	200	0.11	0.122	2.33	-0.09	0.09
Sn	2595	200	-0.03	0.125	1.62	-0.04	0.04
Lg	1425	200	0.19	0.630	0.29	-0.01	0.01

† Station corrections constrained to sum to zero for each phase.

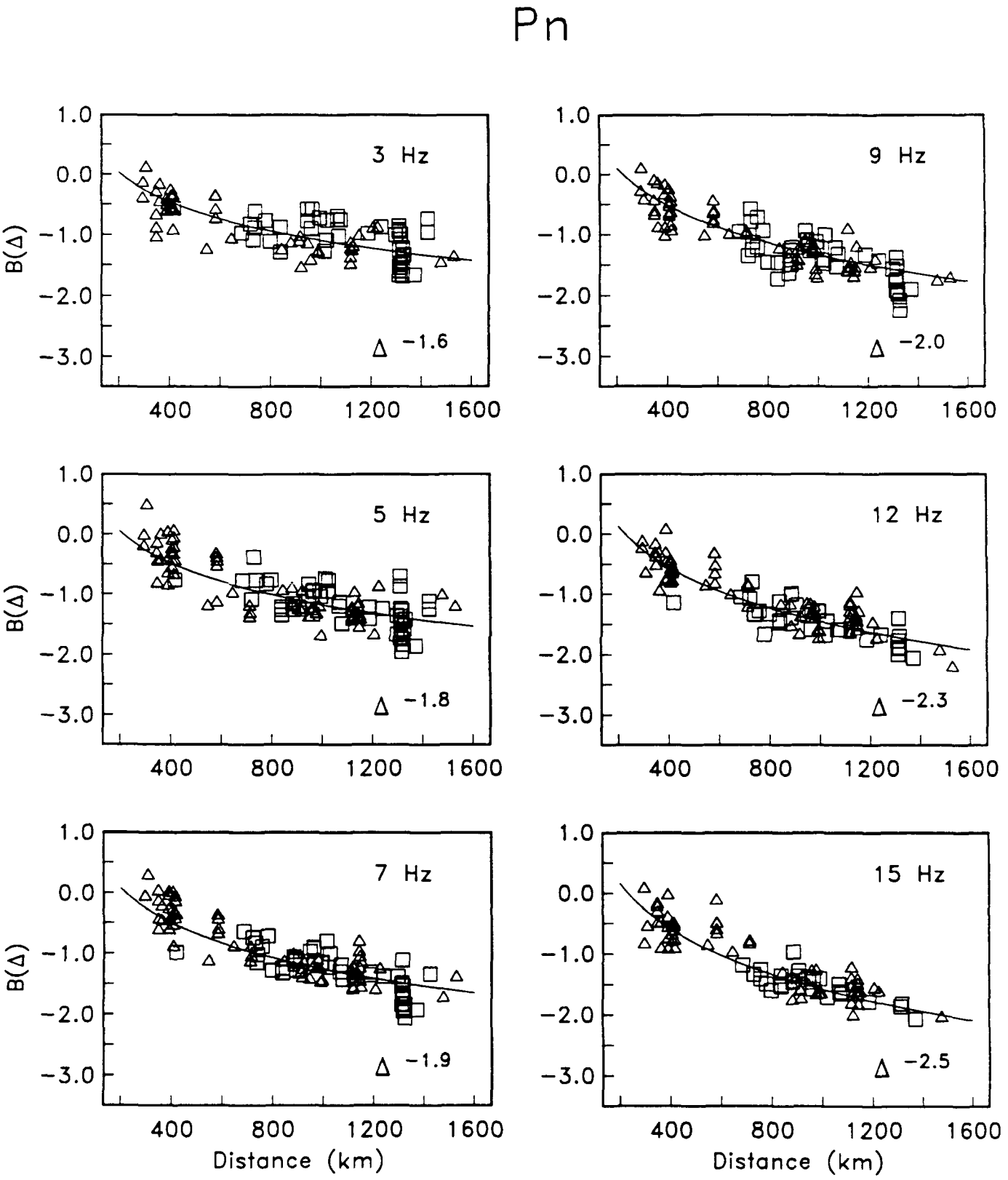

Figure 3.5. *Pn* attenuation is plotted at six frequencies (upper right corner) between 3 and 15 Hz. The solid curves plot the power law attenuation estimated by the inversion (listed in the lower right corner). The symbols plot observed log amplitude minus our estimates of the station correction and log A_{jk}^{0}. Triangles are used for data recorded at ARCESS, and squares are used for data recorded at NORESS.

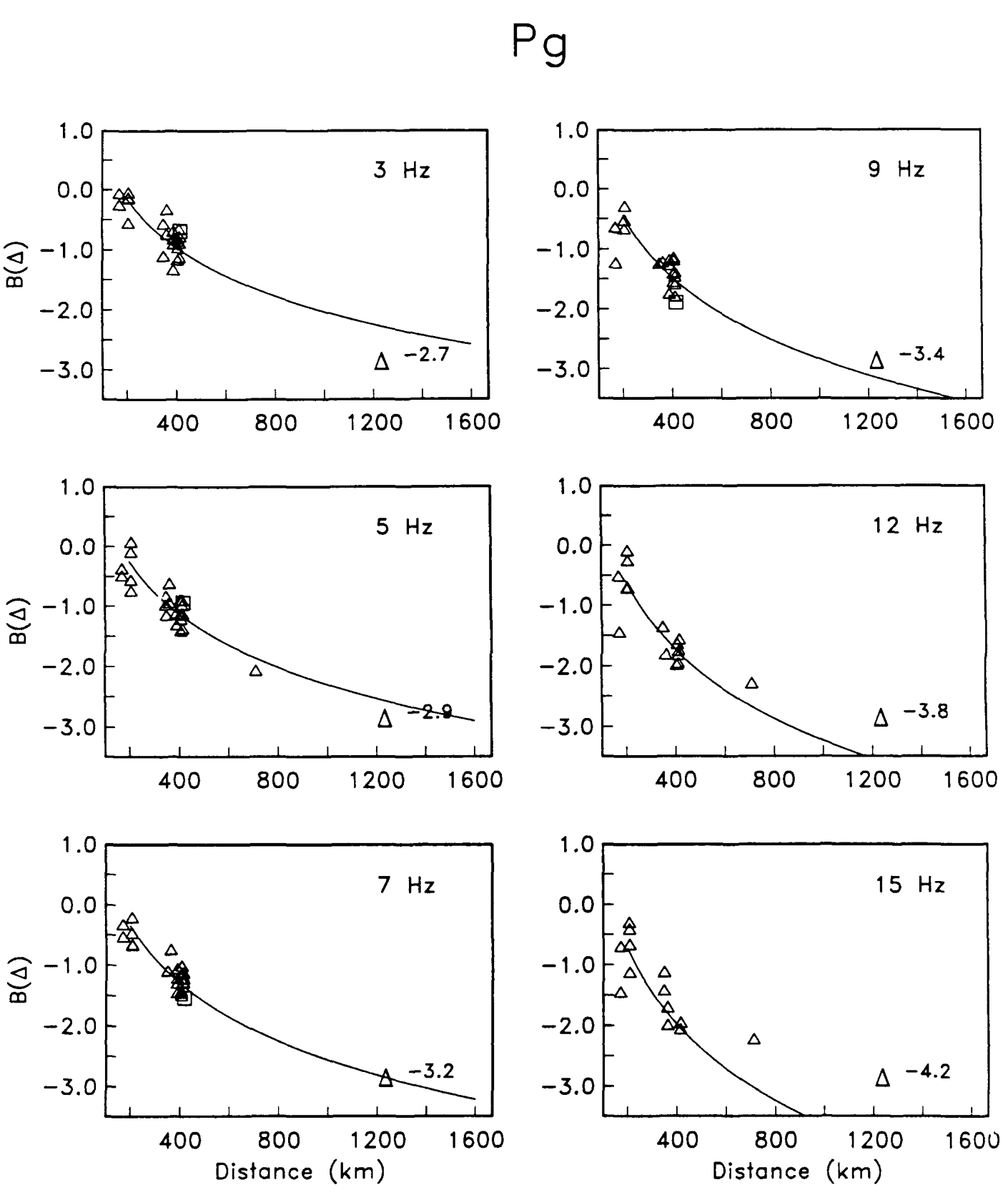

Figure 3.6. *Pg* attenuation is plotted at six frequencies between 3 and 15 Hz (see the caption for Figure 3.5).

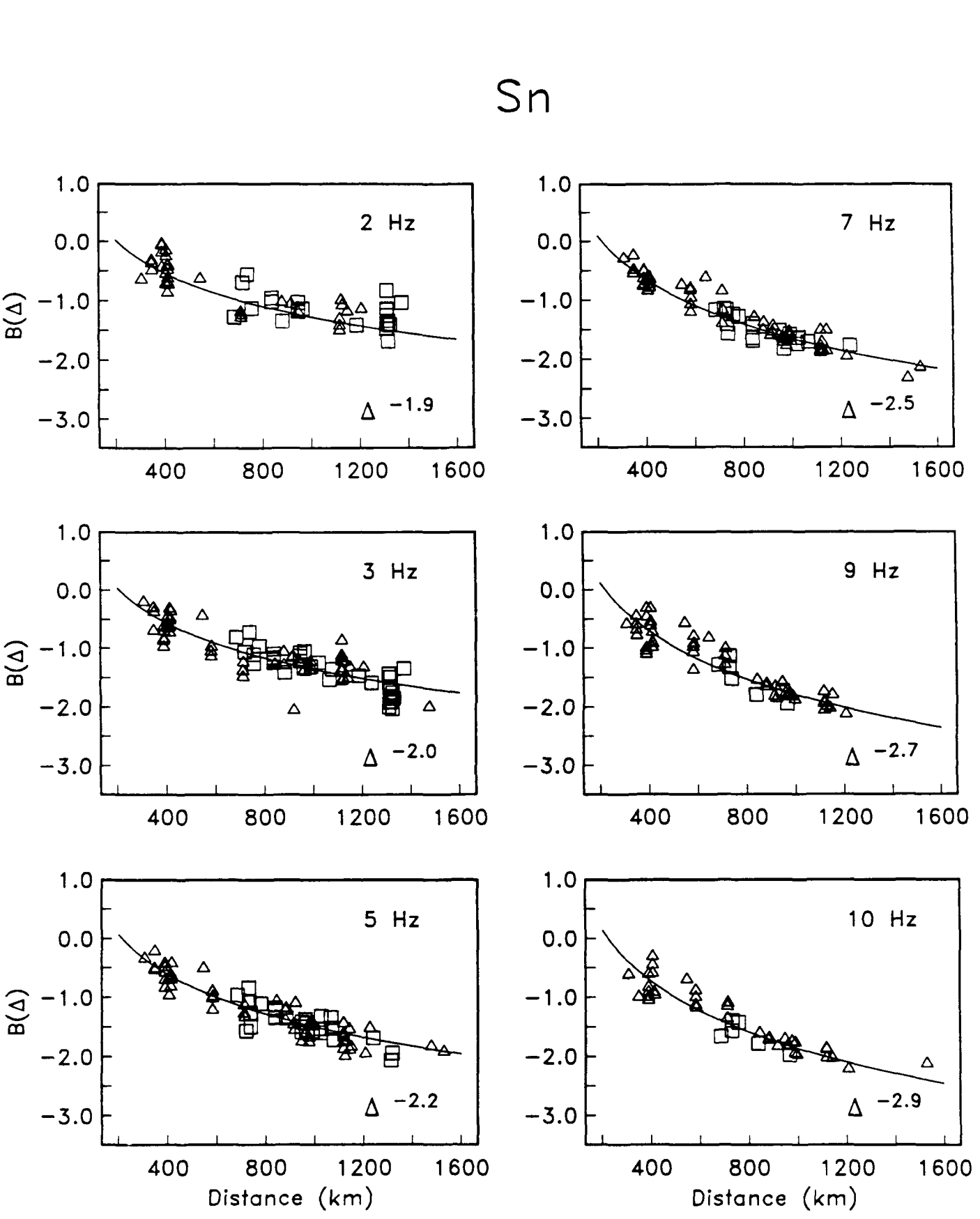

Figure 3.7. *Sn* attenuation is plotted at six frequencies between 2 and 10 Hz (see the caption for Figure 3.5).

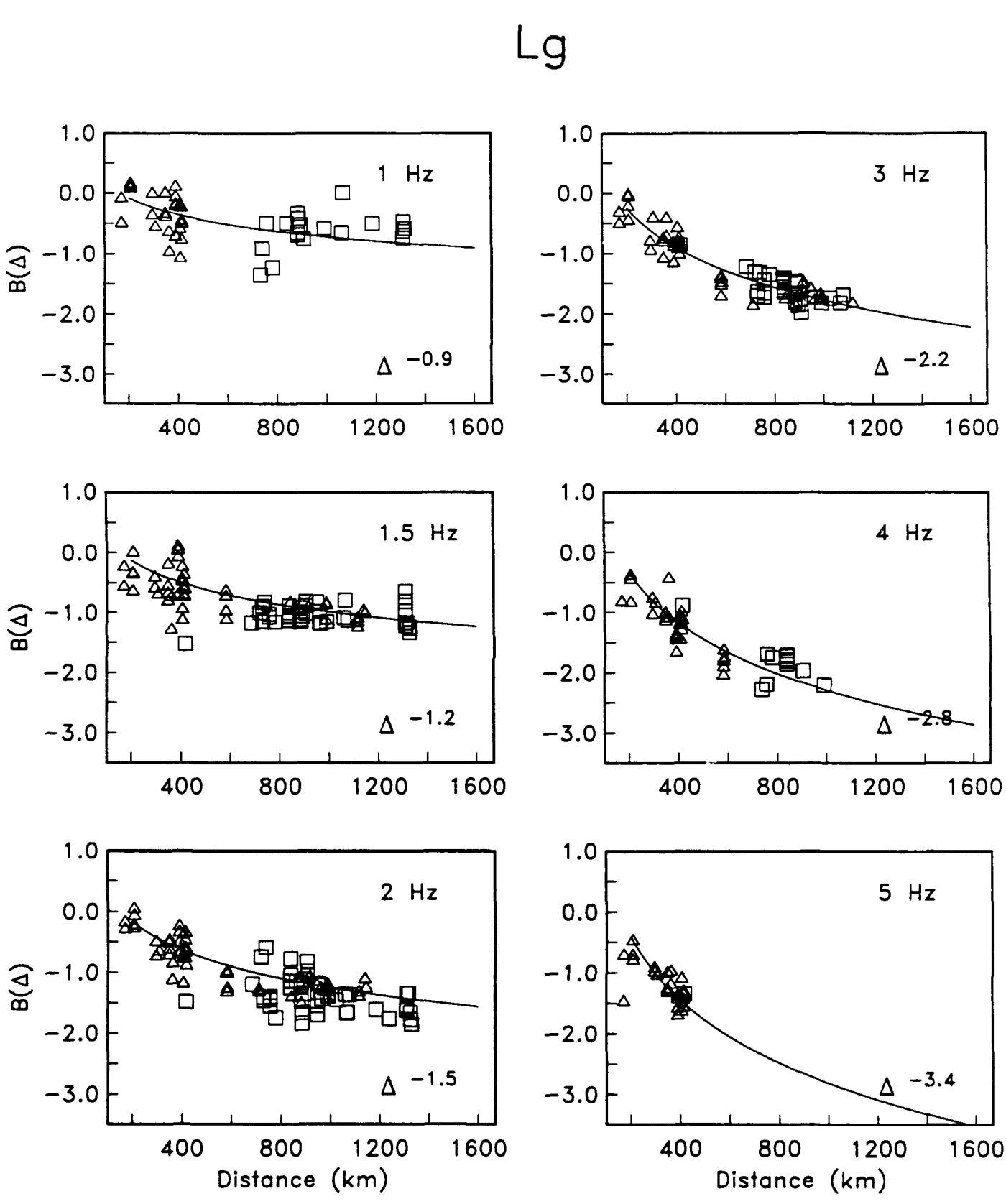

Figure 3.8. *Lg* attenuation is plotted at six frequencies between 1 and 5 Hz (see the caption for Figure 3.5).

Table 3.3 Attenuation parameters (station corrections constrained to be zero for all phases).

Phase	# Data	Δ^0 (km)	α (s)	$n(f) = af + b$ a	b
Pn	5827	200	-0.02	0.068	1.51
Pg	954	200	0.11	0.116	2.45
Sn	2595	200	-0.02	0.112	1.76
Lg	1425	200	0.19	0.632	0.33

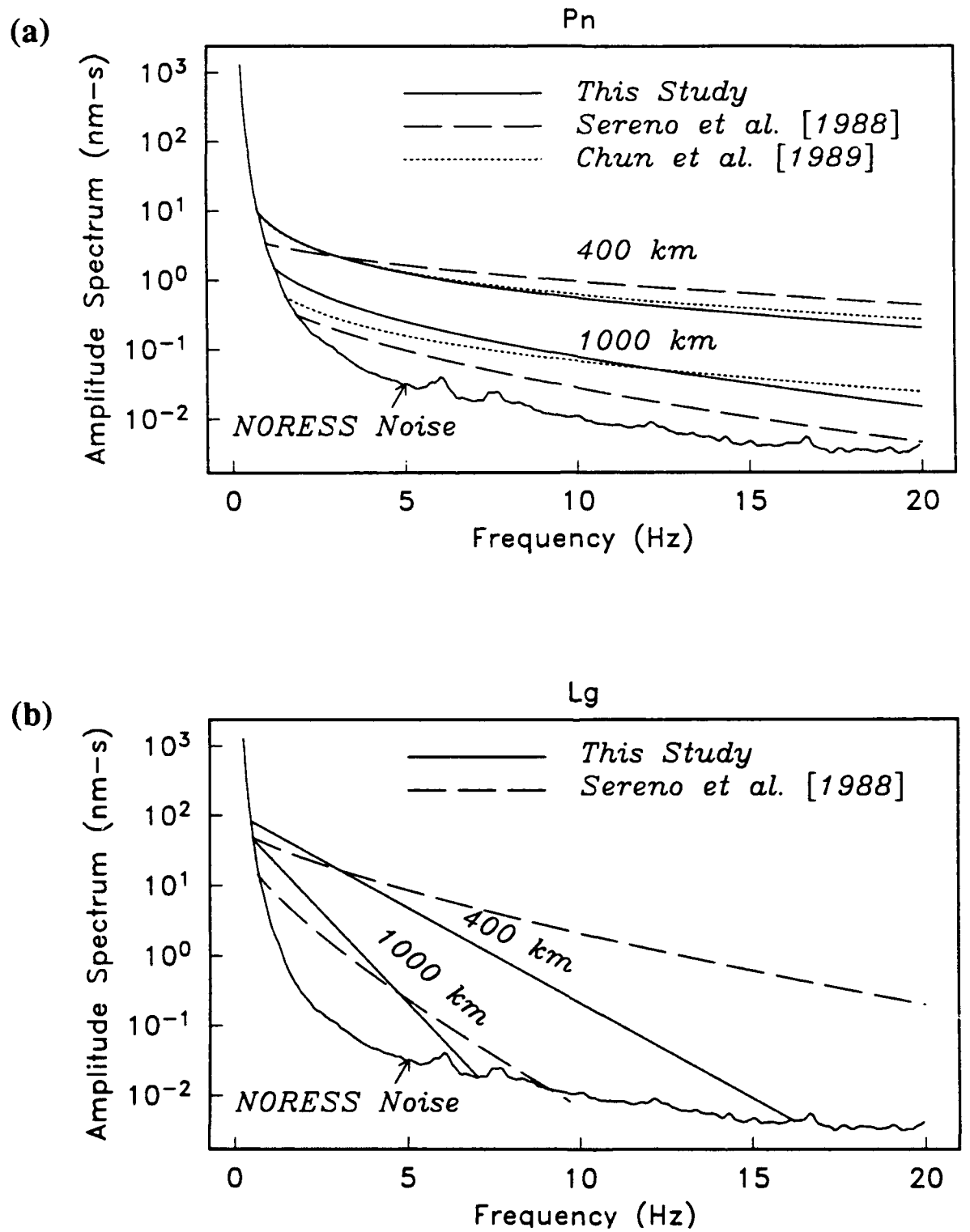

Figure 3.9. Theoretical *Pn* (top) and *Lg* (bottom) spectra at 400 and 1000 km. The solid curves are based on the inversion results obtained in this study. The dashed curves are based on the results of our previous analysis of NORESS data [*Sereno et al.*, 1988]. The dotted curves are based on *Pn* attenuation in the Canadian Shield [*Chun et al.*, 1989]. The theoretical spectra are normalized to the same amplitude at 400 km and 3 Hz. The bottom curve in each panel is an estimate of the average ambient noise spectrum at NORESS [*Suteau-Henson and Bache*, 1988].

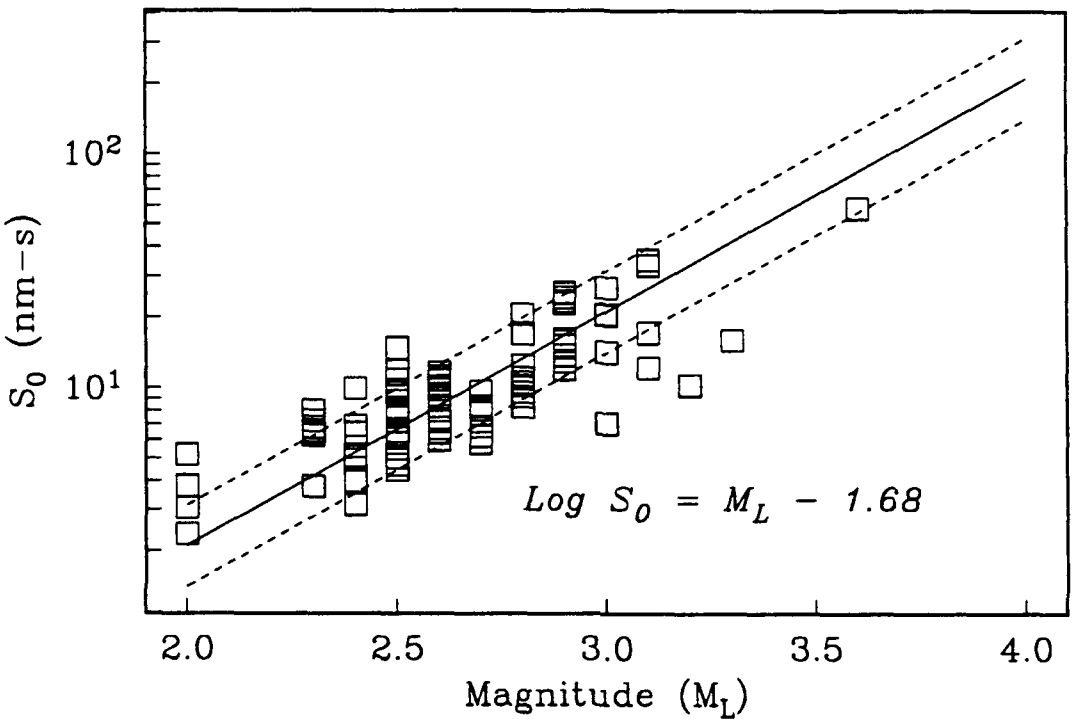

Figure 3.10. Long-period level versus the magnitude determined by the University of Helsinki. The solid line indicates the least-squares fit assuming the slope is one, the dashed lines indicate one standard deviation.

for each event in Table 3.4. Note that the corner frequency in Table 3.4 is based on cube root scaling (it was not determined separately for each event).

Table 3.5 lists the wave-dependent source parameters (for fixed and free station corrections). It is not possible to determine these parameters independently for all phases, so κ_{Pn} is fixed and the excitation factors for the other phases are determined relative to *Pn*. If the source generates both compressional and shear waves, then the amplitude of the shear waves should be about a factor of five greater than the amplitude of the compressional waves (e.g., assuming that the compressional wave velocity at the source is a factor of $\sqrt{3}$ larger than the shear wave velocity). This gives log κ equal to 0.7 for shear phases. Our estimate for κ_{Sn} is less than this, and our estimate for κ_{Lg} is slightly greater than this. However, most of the events used in the inversion are surface mining explosions with unknown radiation patterns, so deviations in κ of this order are not surprising.

3.5 Signal Variance

The unbiased estimate of the variance of log amplitude for each phase, σ_k^2, is estimated from the data residuals using

$$\sigma_k^2 = \frac{1}{N_k} \sum_{i=1}^{N_k} (\Delta d_k)_i^2 \left[\frac{N}{N - L - m} \right] \tag{3.12}$$

where N_k is the number of data for the *kth* wave, Δd_k is the residual (the difference between the observed and theoretical log amplitude) for the *kth* wave, N is the total number of data (all phases), L is the total number of events, and m is the number of inversion parameters. The standard deviation of log amplitude is 0.25–0.28 for *Pn*, *Pg*, and *Lg*, and it is 0.19 for *Sn* (Table 3.6).

3.6 Summary

A method is presented for estimating source, attenuation, and site parameters for regional phases recorded at multiple stations. This method is applied to data from 97 events recorded at NORESS and ARCESS. The main conclusions are:

- Attenuation (including geometrical spreading and anelasticity) is accurately described by $\Delta^{-n(f)}$ with:

$$Pn: \quad n(f) = 0.072 f + 1.40$$
$$Pg: \quad n(f) = 0.122 f + 2.33$$
$$Sn: \quad n(f) = 0.125 f + 1.62$$
$$Lg: \quad n(f) = 0.630 f + 0.29$$

Table 3.4 Long-period levels and corner frequencies.

Event	S_0 (nm-s)	f_c (Hz)	M_L
1	9.6	11.4	2.70
2	8.1	12.0	2.70
3			2.70
4	9.5	11.4	2.80
5	20.3	8.9	3.00
6	8.0	12.1	2.50
7	35.1	7.4	3.10
8	10.5	11.0	2.80
9	5.0	14.1	2.50
10	9.8	11.3	2.50
11	7.8	12.2	2.50
12	6.8	12.7	2.70
13	9.0	11.6	2.60
14	20.6	8.8	3.00
15	6.2	13.1	2.70
16	17.0	9.4	2.80
17			2.90
18	8.3	11.9	2.50
19	6.4	13.0	2.60
20	11.8	10.6	2.50
21	24.2	8.3	2.90
22	9.1	11.6	2.80
23	10.1	11.2	2.60
24	8.2	12.0	2.80
25	9.8	11.3	2.60
26	11.9	10.6	2.90
27	4.7	14.4	2.50
28	6.2	13.2	2.70
29	11.0	10.9	2.80
30	8.0	12.1	2.30
31	2.4	18.1	2.00
32	7.6	12.3	2.50
33	5.1	14.0	2.40
34	4.9	14.2	2.40
35	9.2	11.5	2.50
36	6.6	12.9	2.30
37	7.2	12.5	2.30
38	6.9	12.7	2.40
39	3.2	16.5	2.40
40	10.8	10.9	2.50

Event	S_0 (nm-s)	f_c (Hz)	M_L
41			2.40
42	6.3	13.1	2.30
43	6.5	12.9	2.50
44	6.5	13.0	2.30
45	7.8	12.2	2.50
46	3.8	15.5	2.30
47	6.8	12.7	2.30
48	33.3	7.5	3.10
49	8.2	12.0	2.50
50	4.0	15.2	2.40
51	58.4	6.2	3.60
52	10.2	11.1	3.20
53	16.1	9.6	2.90
54	3.1	16.6	2.00
55	6.4	13.0	2.40
56	3.8	15.5	2.00
57	17.1	9.4	3.10
58	5.6	13.6	2.40
59	5.2	13.9	2.00
60	25.3	8.2	2.90
61	8.3	11.9	2.60
62	9.9	11.2	2.40
63	41.8	7.0	
64	17.6	9.3	
65	5.6	13.6	
66	13.7	10.1	
67	14.8	9.8	2.50
68	12.4	10.4	2.80
69	23.3	8.5	2.90
70	9.3	11.5	2.60
71	6.0	13.3	2.60
72	6.1	13.2	2.50
73	25.5	8.2	2.90
74	11.2	10.8	2.60
75	10.8	10.9	2.60
76	8.3	11.9	2.70
77	13.7	10.1	2.90
78	5.8	13.4	2.50
79	6.7	12.8	2.60
80	10.2	11.1	2.80
81	11.6	10.7	2.60
82	15.8	9.6	2.90
83	12.9	10.3	2.90
84	14.1	10.0	3.00

Event	S_0 (nm-s)	f_c (Hz)	M_L
85	12.1	10.5	3.10
86	8.1	12.0	2.50
87	15.1	9.8	2.90
88	15.9	9.6	3.30
89	11.0	10.9	2.80
90	6.3	13.1	2.50
91	7.0	12.6	3.00
92	4.4	14.7	2.50
93	20.6	8.8	2.80
94	5.8	13.5	2.70
95	26.6	8.1	3.00
96	22.9	8.5	2.90
97	7.2	12.5	2.60

Table 3.5 Wave-dependent source parameters.

Phase	# Data	γ†	δ_{ik} Free log κ	δ_{ik} Fixed log κ
Pn	5827	-1.0	0.0†	0.0†
Pg	954	0.0	0.10	0.15
Sn	2595	-1.0	0.41	0.43
Lg	1425	0.0	0.82	0.78

† Fixed value.

Table 3.6 Standard deviation of log amplitude for regional phases.

Phase	# Data	σ_k
Pn	5827	0.26
Pg	954	0.25
Sn	2595	0.19
Lg	1425	0.28

- The relationship between seismic moment and magnitude is approximately:

$$\log M_0 = M_L + 17.2$$

and the corner frequency of an M_L 3.0 event is estimated to be 9 Hz (assuming cube root scaling).

- The site response is estimated to be slightly larger at ARCESS than it is at NORESS for all four phases. However, a model with the same site response for both arrays gives a similar fit (the difference in variance is less than 2%).

- The standard deviation of log amplitude is between 0.25 and 0.28 for *Pn*, *Pg*, and *Lg*, and it is 0.19 for *Sn*.

(THIS PAGE INTENTIONALLY LEFT BLANK)

4. NOISE SPECTRA

Estimates of the noise spectra for primary and secondary phases are needed to simulate the detection capability of regional seismic networks. It is straightforward to estimate the ambient noise spectra for primary phases, and this is done in Section 4.1 for NORESS and ARCESS. However, detection of secondary phases depends on the ambient noise and the level of the coda of earlier arrivals. *Rivers et al.* [1985] compiled "noise" estimates to be used in simulations with the original *SNAP/D* program. The noise level for secondary phases was simply assumed to be 2.5 times the ambient noise level. However, this simple approximation does not properly account for the magnitude and frequency dependence of the signal-generated coda which contributes to the "noise." A simple approximation that does account for these dependencies is that the signal-generated noise for secondary phases is equal to the signal spectrum of an earlier arrival multiplied by a scaling factor that depends on distance. This is the approximation used by our network simulation program, *NetSim*, to determine the noise levels for secondary phases [*Sereno et al.*, 1990]. Sections 4.2–4.4 give estimates of this scaling factor for pre-*Pg*, pre-*Sn*, and pre-*Lg* noise.

4.1 Ambient Noise

The ambient noise spectrum at NORESS has been extensively studied by others [e.g., *Bungum et al.*, 1985; *Fyen*, 1986, 1987; *Suteau-Henson and Bache*, 1988]. Less work has been done to estimate the ambient noise spectrum at ARCESS, although there has been one preliminary study [*Mykkeltveit et al.*, 1987]. We compute noise spectra from samples taken prior to *Pn* detections as part of our routine signal processing. In this section we compare these noise spectra to results from other studies of NORESS and ARCESS noise.

The top two panels in Figure 4.1 plot the mean and standard deviation of the ambient noise spectra at NORESS and ARCESS computed from 78 five-second time windows taken prior to *Pn*. These spectra are corrected for the short-period instrument response. Our estimate for the noise spectrum at NORESS is generally consistent with results from earlier studies. For example, *Bungum et al.* [1985] estimate the noise level in southern Norway to be −140 to −100 dB (relative 1 m^2/Hz) for frequencies between 0.2 and 0.3 Hz, and −170 to −180 dB at 1 Hz. They note a change in the slope of the noise power spectrum near 2–3 Hz. Above that, they approximate the noise power, P_N, as:

$$\log P_N = -5 \log f - 18 \qquad (4.1)$$

which gives a noise level of −230 dB at 10 Hz. These estimates are within one standard deviation of our estimate of the mean NORESS noise spectrum shown in Figure 4.1. Note that the variance of the noise at NORESS is greater than the variance of the noise at ARCESS (the average standard deviation of the log noise is 0.22 at NORESS,

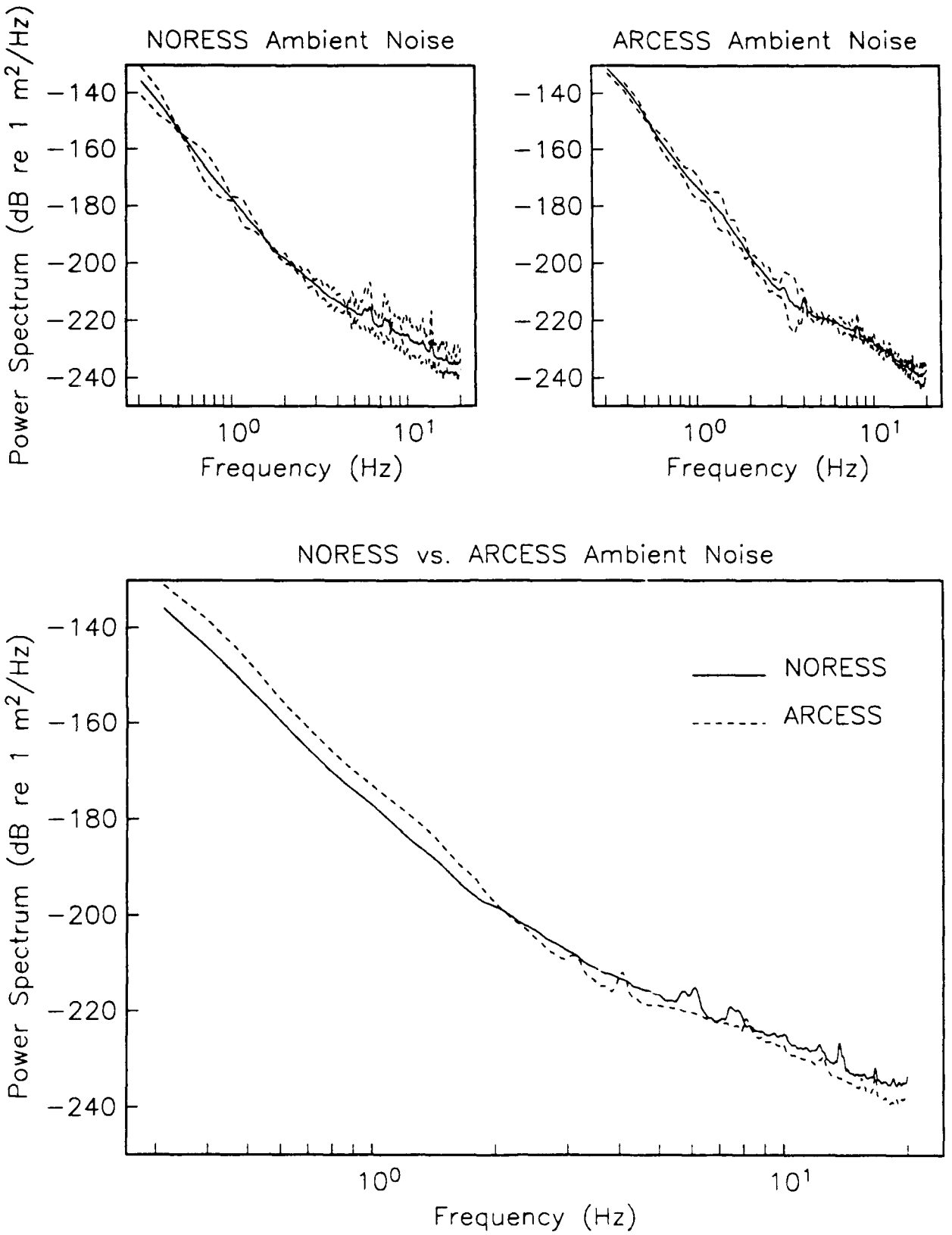

Figure 4.1. Estimates of the ambient noise spectra at NORESS and ARCESS are plotted in the top two panels. The lowest panel compares the mean noise spectrum at NORESS to the mean noise spectrum at ARCESS.

and it is 0.14 at ARCESS). The large noise variance at NORESS occurs primarily for frequencies greater than 5 Hz, and it is probably related to cultural activity.

The mean ambient noise spectra for the two arrays are compared in the bottom panel of Figure 4.1. The NORESS noise is about 4 dB lower than the ARCESS noise for frequencies less than 2 Hz, but is it about 3–5 dB higher than the ARCESS noise for frequencies greater than 2 Hz. This supports the preliminary conclusions of *Mykkeltveit et al.* [1987], from a much smaller dataset. They attribute the higher noise levels at ARCESS for $f < 2$ Hz to the closer proximity of this array to the coastline, and the higher noise levels at NORESS for $f > 2$ Hz to differences in cultural noise (since the NORESS array is located in a region with higher population density).

4.2 Pre-Pg Noise

The noise preceding *Pg* is equal to the ambient noise for distances less than the *Pn* critical distance. However, at larger distances the pre-*Pg* noise also includes *Pn* coda. Our dataset does not include many *Pg* phases, so it is difficult to determine an accurate relationship between the pre-*Pg* noise and the *Pn* signal spectrum. For a first approximation, we use the time-domain amplitude ratio of the pre-*Pg* noise and the *Pn* signal for mining explosions in the Kola Peninsula recorded at ARCESS. Since *Pg* attenuates much more rapidly than other regional phases in Fennoscandia (see Section 3), the simulations of detection capability presented in the next section are not very sensitive to the assumed relationship between pre-*Pg* noise and *Pn* signal amplitude. Therefore, the approximation presented here should be adequate to produce accurate simulations.

Figure 4.2 plots examples of *Pn* and *Pg* envelope functions for representative explosions in four mines located in the Kola Peninsula. The event number and mine code from Table 3.1 and the distance to ARCESS are listed in the upper right corner of each panel. More than half the *Pg* phases in our dataset are recorded at ARCESS from events in one of these four mines. The *Pn* and pre-*Pg* amplitudes are indicated on each trace. The average ratio of the pre-*Pg* noise amplitude to the *Pn* signal amplitude for events with *Pn snr* > 4 is 0.30. We don't have enough *Pg* data to determine the dependence on epicentral distance. Therefore, the simulations in Section 5 assume that the signal-generated component of the pre-*Pg* noise is equal to 0.30 times *Pn* signal spectrum for all distances.

4.3 Pre-Sn Noise

The signal-generated noise prior to *Sn* includes waves that propagate in the crust and upper mantle. For the purpose of simulating detection capability, the most important effect to be included is the magnitude dependence. For this, we relate the pre-*Sn* noise to the signal amplitude for *Pn*. We don't use *Pg* because it attenuates much more rapidly in Fennoscandia than *Pn*, and it is rarely observed at distances beyond 500–600 km.

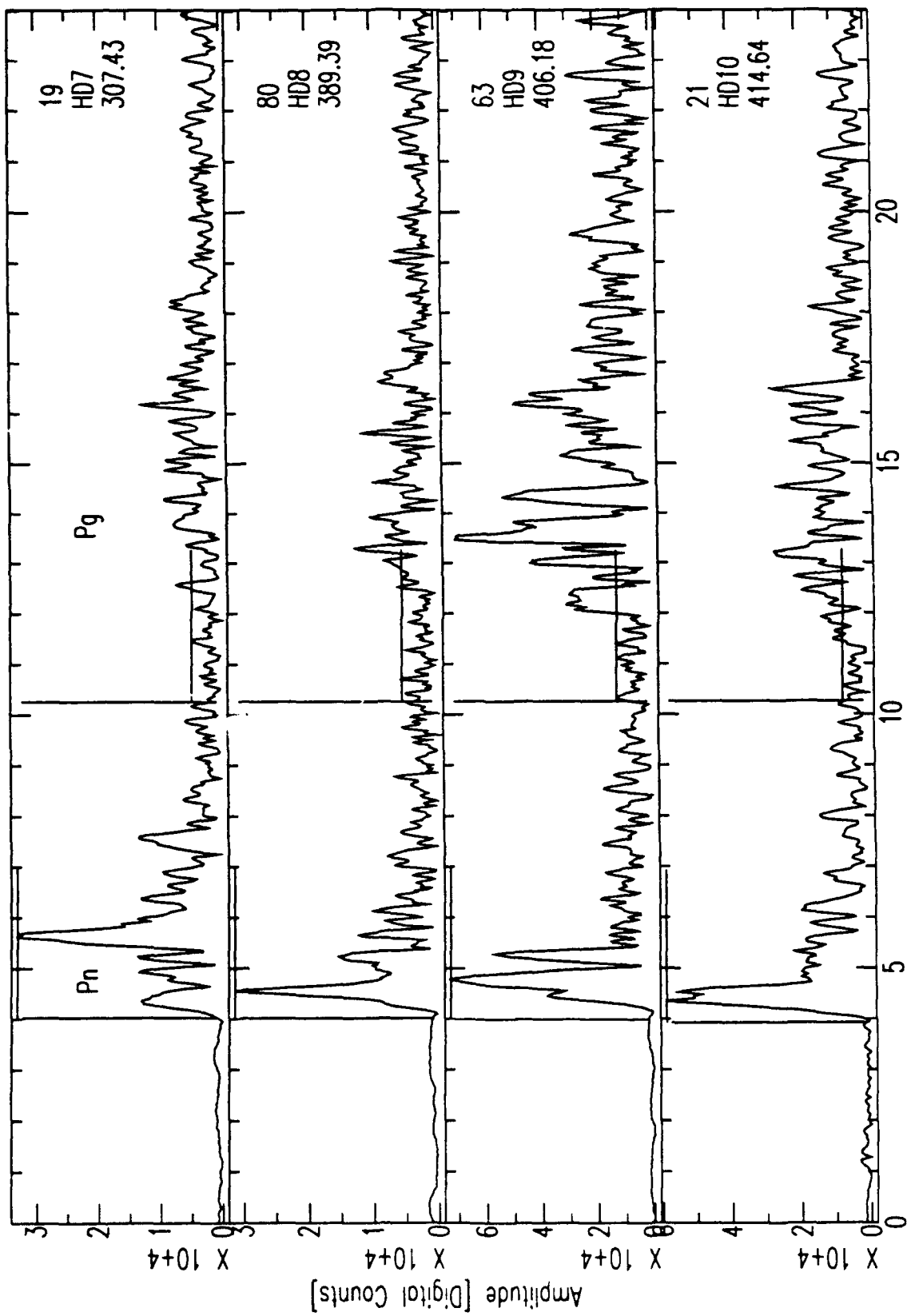

Figure 4.2. Envelopes of *Pn* and *Pg* are plotted for four mining explosions recorded at ARCESS. The *Pn* signal and pre-*Pg* noise amplitudes are indicated by horizontal lines.

We approximate the relationship between pre-*Sn* noise and *Pn* signal amplitude by the ratio of the *Sn lta* (long-term average) and the *Pn sta* (short-term average) measured on a 2–4 Hz incoherent beam. The *Pn sta* is the average absolute amplitude in a 1-s window centered around *Pn*. The *Sn lta* is equal to a weighted average of the amplitude in a 30-s window prior to *Sn*. Figure 4.3 plots histograms of this ratio for events processed by the *IMS* between October 1989 and March 1990. The median ratio is 0.34 for distances < 600 km, and it is 0.28 for distances > 600 km. For the simulations, we approximate the distance dependence of this ratio as:

$$\frac{\text{pre}-Sn}{Pn}(\Delta) = -10^{-4}\,\Delta + 0.38 \qquad (4.2)$$

where Δ is the epicentral distance in kilometers. This equation was derived by setting the ratio equal to 0.34 at 390 km (which is the median distance for Δ < 600 km), and to 0.28 at 970 km (which is the median distance for Δ > 600 km). We assume that the ratio is zero for distances greater than 3800 km.

4.4 Pre-Lg Noise

The effect of signal-generated noise on detection capability is particularly important for *Lg* because the *Sn* coda decays very slowly. For example, Figure 4.4 plots *Lg snr* in four distance ranges as a function of magnitude (these data are from the *IMS* database at CSS). Note that the *Lg snr* is essentially independent of magnitude for M_L between 2.0 and 3.0. The solid line in each figure indicates the expected dependence of the log signal amplitude on magnitude. Clearly, the pre-*Lg* noise and *Lg* signal amplitudes have nearly the same dependence on M_L. This means that the capability to detect *Lg* in Fennoscandia is nearly independent of event magnitude between 2.0 and 3.0.

Figure 4.5 plots histograms of the ratio of *Lg lta* and *Sn sta* for events in the *IMS* database. Note that the median ratio is larger for the more distant events (Δ > 600 km). One explanation is that the dominant contribution to the *Sn* coda consists of surface multiples with one or more extra crustal delays. These phases can have amplitudes that are even larger than the *Sn* amplitude [*Kennett*, 1985], but they arrive after *Lg* for distances less than 400 km. For example, Figure 4.6 plots travel time curves for *Sn*, *Lg*, and two surface multiples (*SSn* and *SSSn*). A schematic ray path for *SSn* is shown at the top of Figure 4.6 (note that the surface reflection may occur near the source or near the receiver). *Kennett* [1985] explains that the larger amplitude of *SSn* over *Sn* is due to reduced geometrical spreading because the path length in the mantle is smaller, and because the reflection at the Moho is very efficient for near-critical incidence. Therefore, the *Sn* coda decay rate is higher for distances < 400 km than it is at farther distances.

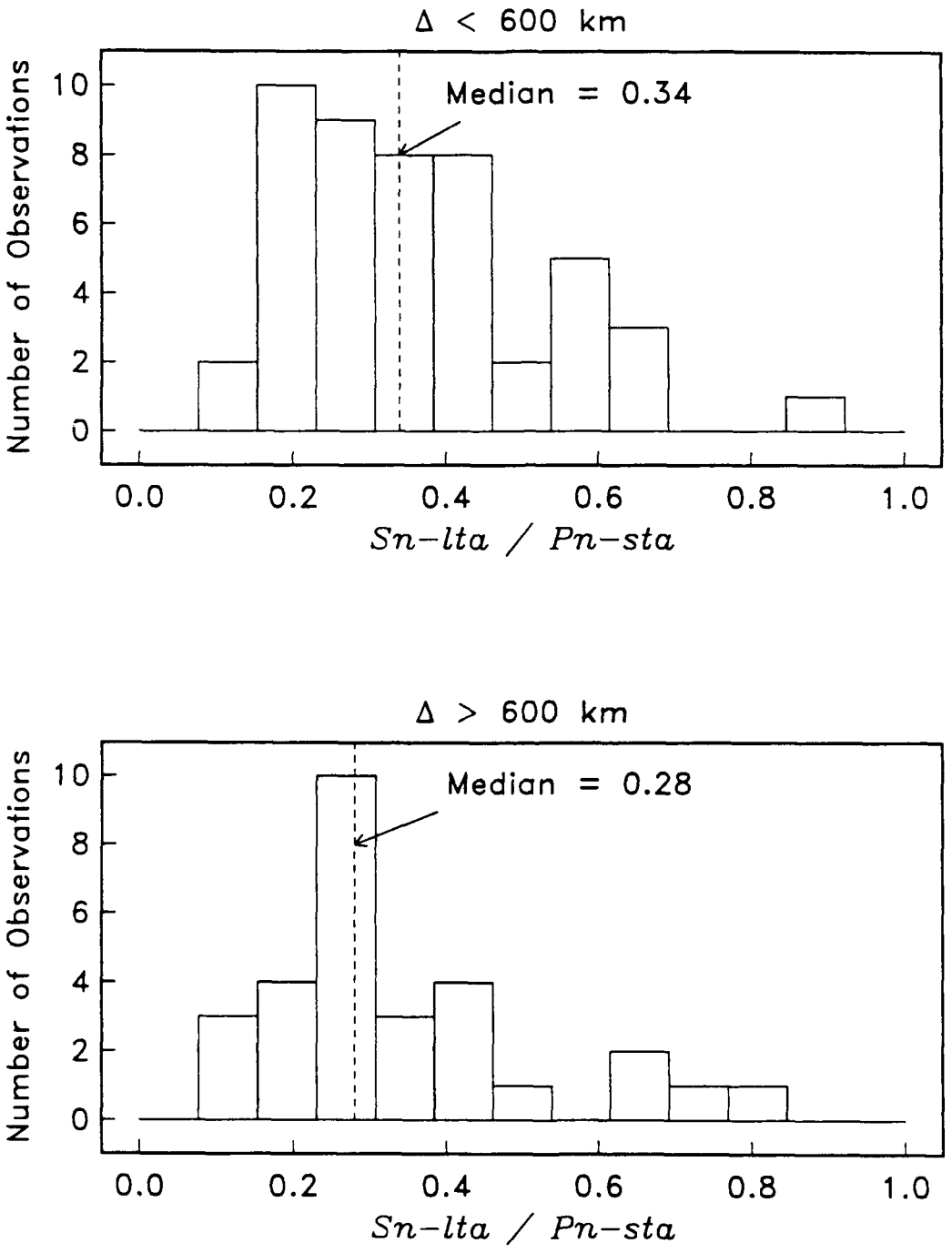

Figure 4.3. Histograms of the ratio of *Sn lta* and *Pn sta* for events in the *IMS* database with *Pn snr* > 4. The amplitudes are measured on a 2–4 Hz incoherent beam. The median ratio is indicated for Δ < 600 km, and for Δ > 600 km.

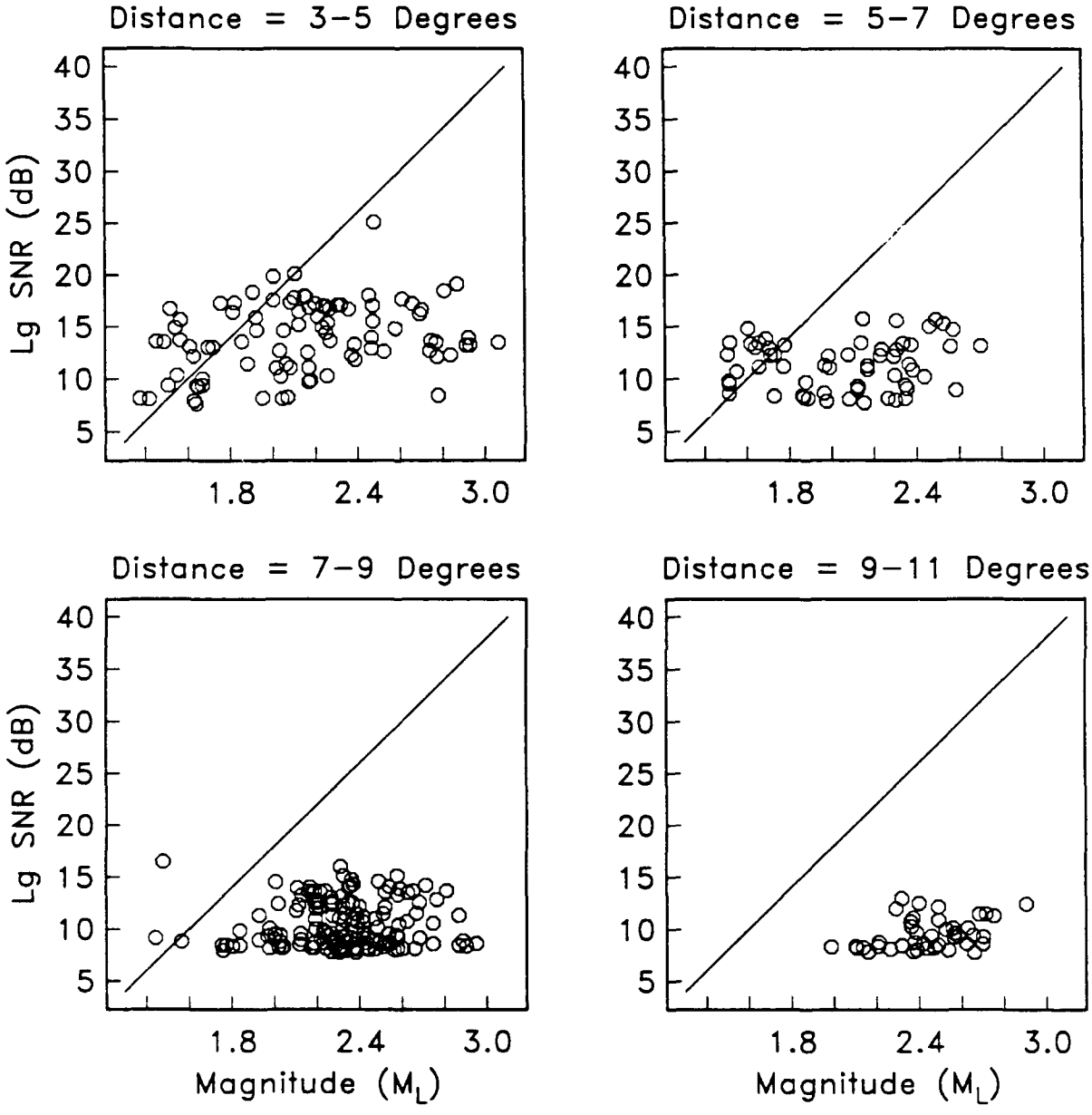

Figure 4.4. *Lg snr* measured on a 2–4 Hz incoherent beam is plotted for four distances ranges as a function of local magnitude. The solid line in each panel indicates the expected dependence of the log *Lg* signal amplitude on M_L. The *snr* threshold used for detection on this beam is 7.6 dB, so there are no *Lg* phases with *snr* less than this.

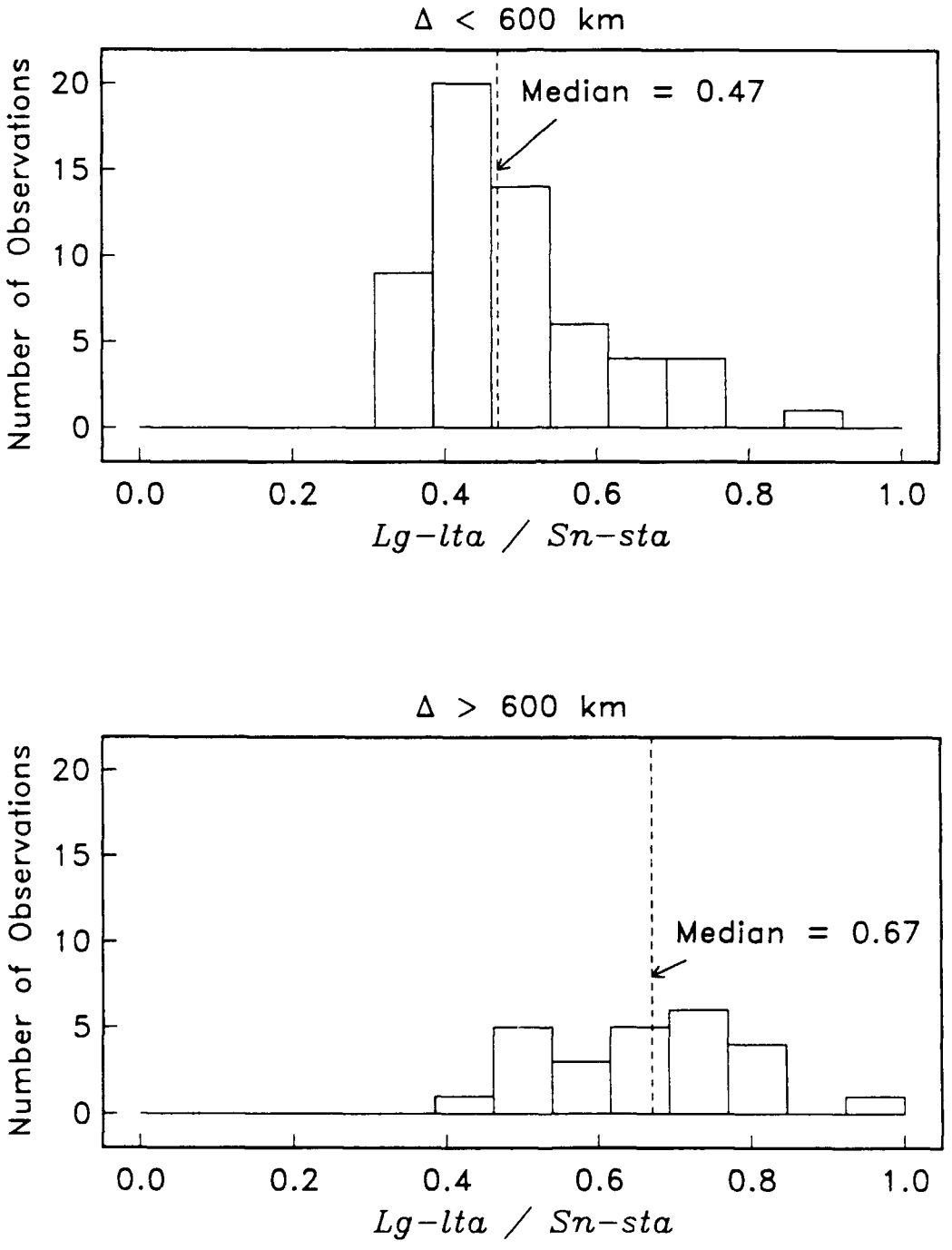

Figure 4.5. Histograms of the ratio of *Lg lta* and *Sn sta* for events in the *IMS* database with *Sn snr* > 2.5. The amplitudes are measured on a 2–4 Hz incoherent beam. The median ratio is indicated for Δ < 600 km., and for Δ > 600 km.

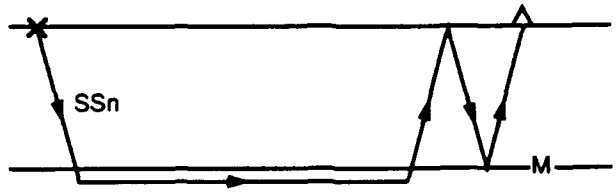

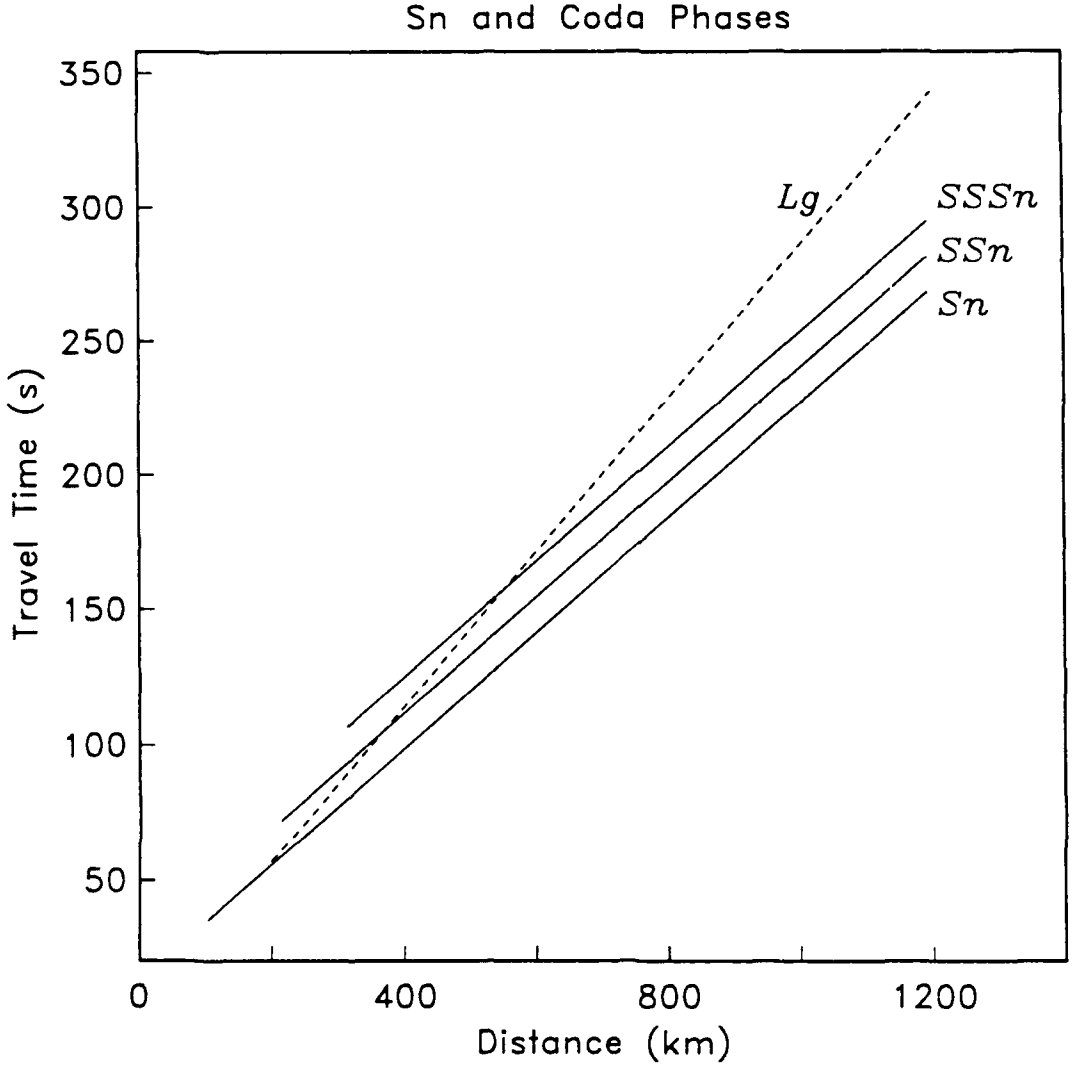

Figure 4.6. Travel time is plotted for *Sn*, *Lg*, and two surface multiples (*SSn* and *SSSn*). The top figure is a schematic ray diagram for the surface multiple, *SSn*. The surface multiples comprise a dominant contribution to the *Sn* coda, and these phases arrive after *Lg* for events at distances less than 400 km.

For the simulations in Section 5, we assume that the distance dependence of the amplitude ratio of pre-*Lg* and *Sn* is given by:

$$\frac{\text{pre}-Lg}{Sn}(\Delta) = 4\times10^{-4}\,\Delta + 0.31 \qquad (4.3)$$

which gives 0.47 at 390 km (the median distance for $\Delta < 600$ km), and 0.67 at 890 km (the median distance for $\Delta > 600$ km). We also assume that the maximum value of this ratio is 0.8.

5. DETECTION AND LOCATION CAPABILITY

This section presents simulations of the detection and location capability of the NORESS and ARCESS arrays. These simulations are normalized by estimates of the frequency-dependent source, attenuation, and station noise presented in earlier sections. The purpose is to validate the normalization by comparison to the capability actually achieved by NORESS and ARCESS.

The frequency-dependent beam gain for array stations and the *snr* thresholds required for detection are described in Section 5.1. These are the only normalization parameters not described in earlier sections of this report. Section 5.2 gives separate simulations of the detection thresholds at NORESS and ARCESS, and Section 5.3 presents simulations of the detection capability of both arrays. Simulations of the location capability of NORESS and ARCESS are given in Section 5.4. These simulations are based on the estimates of arrival time and azimuth variance given in Section 2.

5.1 Station Parameters

The frequency-dependent beam gain for *P* phases at NORESS is estimated by *Kvaerna* [1989] for frequencies between 0.5 and 10 Hz. Beam gain is defined as the ratio of the noise suppression to the loss in signal caused by a lack of coherence across the array [e.g., *Kvaerna and Mykkeltveit*, 1986]. We use the beam gain estimated by *Kvaerna* [1989] for *Pn*, and extrapolate to higher frequencies by assuming that the gain (in dB) decays linearly from the value at 10 Hz to zero at 20 Hz (Figure 5.1). *Kvaerna* [1989] considered *P* phases that are preceded by ambient noise. However, the "noise" for *Pg* beyond about 200 km includes relatively coherent *Pn* coda. To account for this, we represent the beam gain for *Pg* as the ambient noise suppression divided by the *Pg* signal loss (which should be similar to the beam gain for *Pn*), but this gain is also applied to the signal-generated component of the noise. That is, we assume that beamforming can reduce the level of the ambient noise relative to *Pg*, but it does not change the relative amplitude of *Pg* and the signal-generated component of the noise.

The beam gain for *Pg* (relative to ambient noise) can be estimated from the ratio of the *snr* measured on a 2–4 Hz coherent beam and the *snr* measured on 2–4 Hz incoherent beam (incoherent beams are formed by summing the absolute values of filtered traces recorded by the individual sensors in the array). Application of this method to 195 *Pg* phases in the *IMS* database (between October 1989 and March 1990) for events at distances > 250 km gives an average beam gain of 10 dB between 2 and 4 Hz. This method was also applied to 1135 *Pn* phases to verify that it gives accurate results. The average *Pn* beam gain determined from the *IMS* data is 12 dB between 2 and 4 Hz. This is within 1 dB of the estimate by *Kvaerna* [1989], which lends support to this method for estimating beam gain. We have not estimated the frequency dependence of the beam gain for *Pg*, but it is probably similar to that observed for *Pn*. Therefore, we assume that the beam gain for *Pg* is 10 dB between 2 and 4 Hz

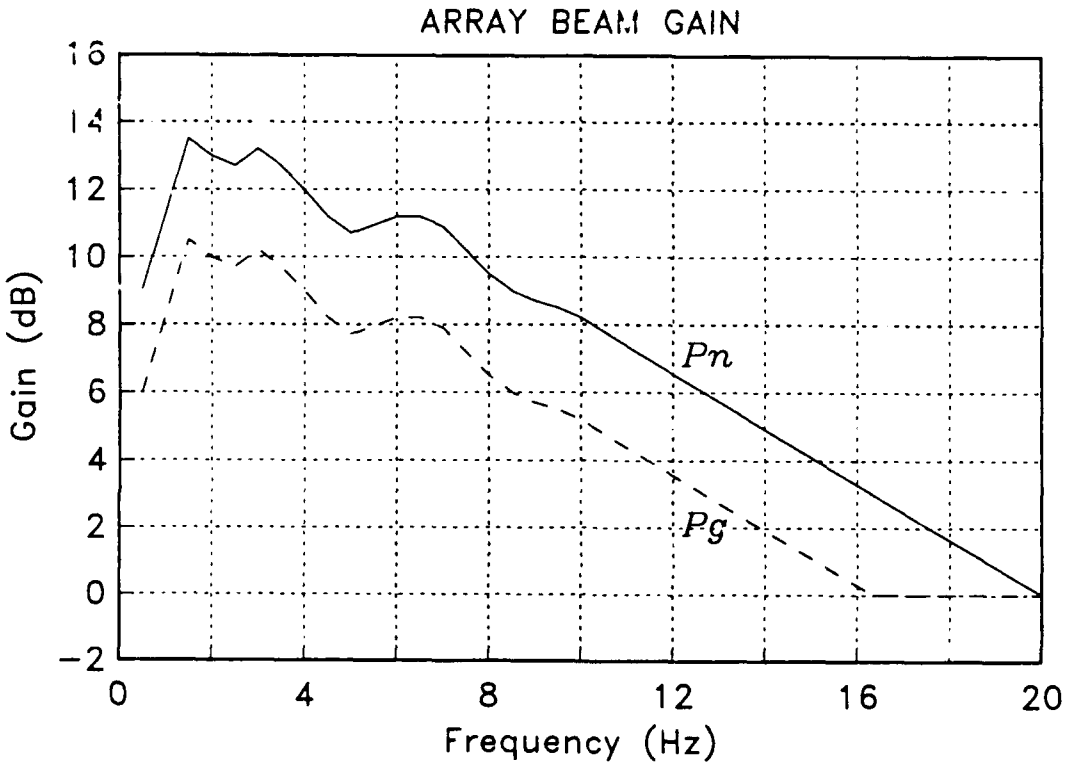

Figure 5.1. Estimates of the beam gain for array stations as a function of frequency are plotted for *Pn* and *Pg* (the beam gain is assumed to be the same for NORESS and ARCESS). The beam gain approaches 14 dB between 1.5 and 3.5 Hz (which is equal to $\sqrt{N}$ for the full array, where N is the number of array elements).

(from the analysis of the *IMS* data), and that it has the same frequency dependence as the beam gain for *Pn* (Figure 5.1).

Regional shear phases are detected often on incoherent beams. These beams are well-suited for detection of arrivals with low coherency across the array [*Ringdal*, 1985]. For example, over 70% of the *Sn* phases in the *IMS* database were detected with maximum *snr* on incoherent beams. Similarly, over half of the *Lg* phases for distances > 250 km are detected with maximum *snr* on incoherent beams. The *snr* measured on an incoherent beam is not much different from the *snr* measured on a single channel (e.g., the beam gain is close to 0 dB). The main advantage of forming incoherent beams is that the noise variance is lower. Thus, the *snr* threshold for an incoherent beam is lower than it is for single channel at a fixed rate of false alarms. [T. Kvaerna, personal communication, 1990]. For the simulations, we assume that shear phases are detected on incoherent beams. Therefore, we assume that the beam gain is 0 dB, and we use a lower *snr* threshold than we use for coherent beams (see below). However, the result is not much different if we use coherent beams. For example, we find that the average beam gain for 596 *Lg* phases in the *IMS* database is 5 dB for detections on coherent beams (the *snr* threshold required for detection on these beams is 12 dB). The gain for incoherent beams is 0 dB, but the *snr* threshold is only 6–8 dB. Therefore, detection on either beam type requires a single-channel *snr* of about 7 dB.

The *snr* thresholds for beams used in the *IMS* signal processing are based on a false alarm rate of 20–25% [*Kvaerna et al.*, 1987]. These thresholds (12 dB for coherent beams and 6–8 dB for incoherent beams) are based on time-domain amplitudes measured on filtered beams. However, our simulations are based on a parameterization of spectral amplitudes which require a different *snr* threshold to achieve the same rate of false alarms. The easiest way to determine the *snr* thresholds for our spectral parameterization is to compare the *snr* in the frequency domain to the *snr* in the time domain for a single channel. To do this, the individual sensor traces are filtered over a 2-Hz band centered at the dominant signal frequency. The time-domain *snr* is estimated for each trace and averaged across the array. The frequency-domain *snr* is measured directly from signal and noise spectra for each phase. The ratio of the frequency-domain *snr* and the time-domain *snr* is calculated for each phase used in the inversion database (Table 3.1). We find that this ratio is approximately 0.8 for *Pn*, *Pg*, and *Sn*, and 0.6 for *Lg* (the *Lg* spectra are computed for a longer time window, so a lower ratio is expected). Therefore, the frequency-domain *snr* thresholds for a false alarm rate of 20–25% are about 10 dB for *Pn* and *Pg* (assuming detection on a coherent beam). If we assume that shear phases are detected on incoherent beams, then the frequency-domain *snr* thresholds are approximately 6 dB for *Sn*, and 3.5 dB for *Lg*. Table 5.1 summarizes the beam gain and *snr* thresholds for each phase used for the simulations presented in Sections 5.2–5.4.

Table 5.1 Beam gain and *snr* thresholds.

Phase	Beam Type	Beam Gain (dB)	*snr* Threshold (dB)
Pn	Coherent	Figure 5.1	10.0
Pg	Coherent	Figure 5.1	10.0
Sn	Incoherent	0.0	6.0
Lg	Incoherent	0.0	3.5

5.2 Detection Thresholds at Individual Stations

The detection thresholds at NORESS and ARCESS are estimated from the normalization parameters described in earlier sections of this report. These estimates are compared to the observed capability to validate the normalization.

The 90% threshold for *P*-wave detection at NORESS is shown in Figure 5.2. This simulation is based on our attenuation, source, and station models for frequencies between 1 and 20 Hz. The threshold increases from about M_L 1.8 at 400 km to M_L 2.7 at 1000 km (Leningrad is about 1000 km from NORESS). The 90% detection threshold for *P* or secondary phases at NORESS is plotted in Figure 5.3. It is about 0.3 M_L lower than the *P*-wave detection threshold. *Ringdal* [1986] estimated the NORESS detection threshold by comparing detection lists to an independent bulletin produced by the University of Helsinki. He estimated the 90% detection threshold for *P* waves to be 2.7 for distances between 700 and 1400 km, and he estimated the 90% threshold for detecting either *P* or secondary phases to be M_L 2.5 for this same distance range. Most of the events used in his study were mining explosions in western Russia, about 1000 km from NORESS. In a similar study, *Gibowicz* [1987] estimated the detection threshold at NORESS for mining explosions in Lubin, Poland. These events are also about 1000 km from NORESS (Figure 5.2). He was unable to determine a distinct threshold above which all events were detected, but he found that M_L 2.7 approaches this limit. The detection threshold at shorter distances was estimated by *Mykkeltveit* [1986] by comparing detection lists at NORESS to a bulletin produced by the University of Bergen for events in western Norway. He estimates that M_L 1.8 is the 50% detection threshold for *P* waves, and the 70% threshold for detecting either *P* or secondary phases at 400 km. Our estimates of the detection threshold of the NORESS array in Figure 5.2 and 5.3 are in close agreement with these empirical studies.

Figure 5.4 shows our simulation of the 90% detection threshold for *P* waves at ARCESS. This threshold is about M_L 2.4 at 1000 km, which is 0.3 M_L less than the threshold for NORESS at this distance. We assume the same propagation characteristics for paths to both arrays, so the difference is due to a combination of the lower noise levels above 2 Hz (Figure 4.1) and larger station corrections at ARCESS (Table 3.2). *Mykkeltveit and Ringdal* [1988] estimated the detection capability of ARCESS using the same method that *Ringdal* [1986] used for NORESS. They found that the 90% detection threshold for *P* waves is M_L 2.5 for events in western Russia (800–1200 km), which is 0.2 M_L lower than the NORESS threshold estimated by *Ringdal* [1986] for events in this same region. Thus, our simulation for ARCESS agrees well with the empirical results of *Mykkeltveit and Ringdal* [1988]. Figure 5.5 shows our simulation of the 90% detection threshold for *P* or secondary phases at ARCESS. As was the case for NORESS, the detection threshold is 0.2–0.3 M_L lower if secondary phases are also included in the detection criterion.

A minimum of two detections (including arrival time and azimuth) are required to locate regional events. Therefore, we estimate the 90% thresholds for detecting one

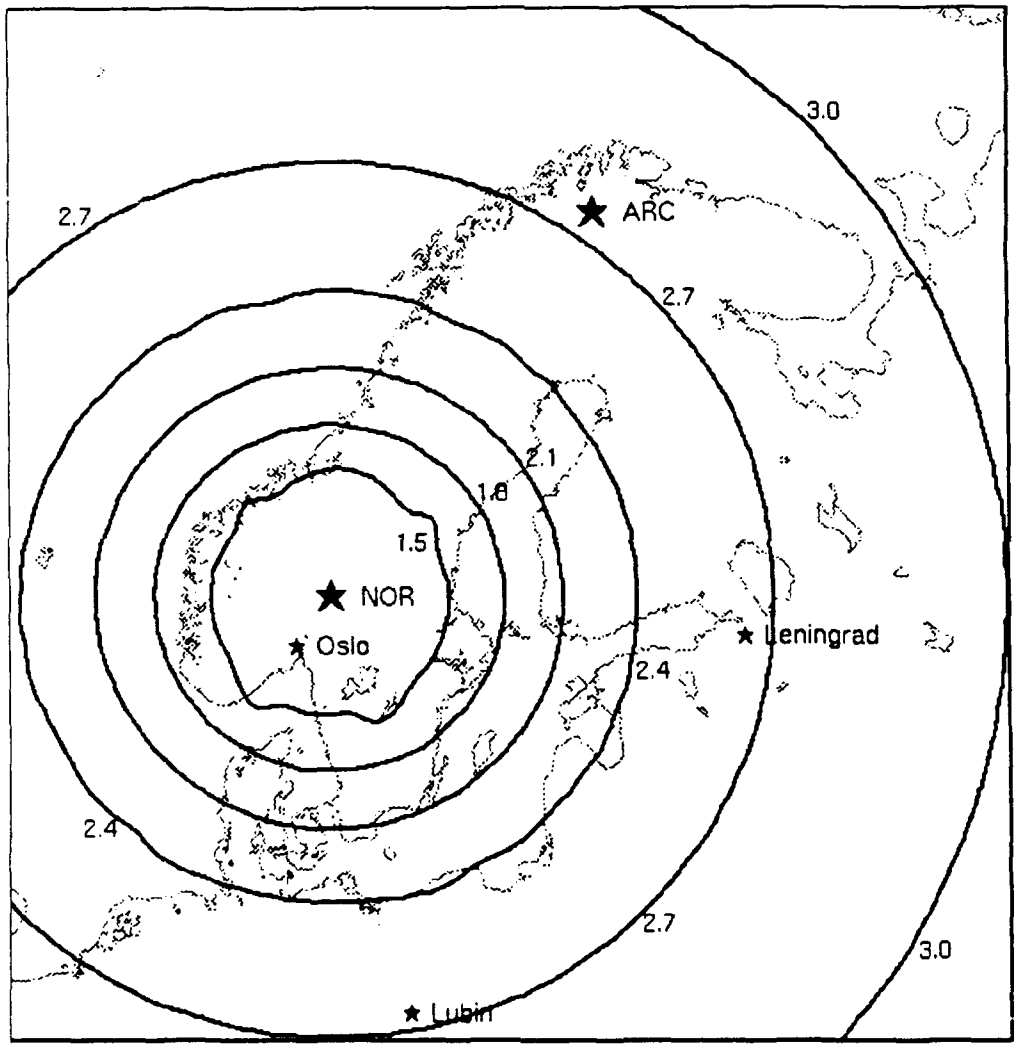

Figure 5.2. Estimate of the 90% M_L threshold for *P*-wave detection at NORESS. The irregular shape of the contour closest to the array is caused by insufficient epicenter grid sampling, and has no physical significance.

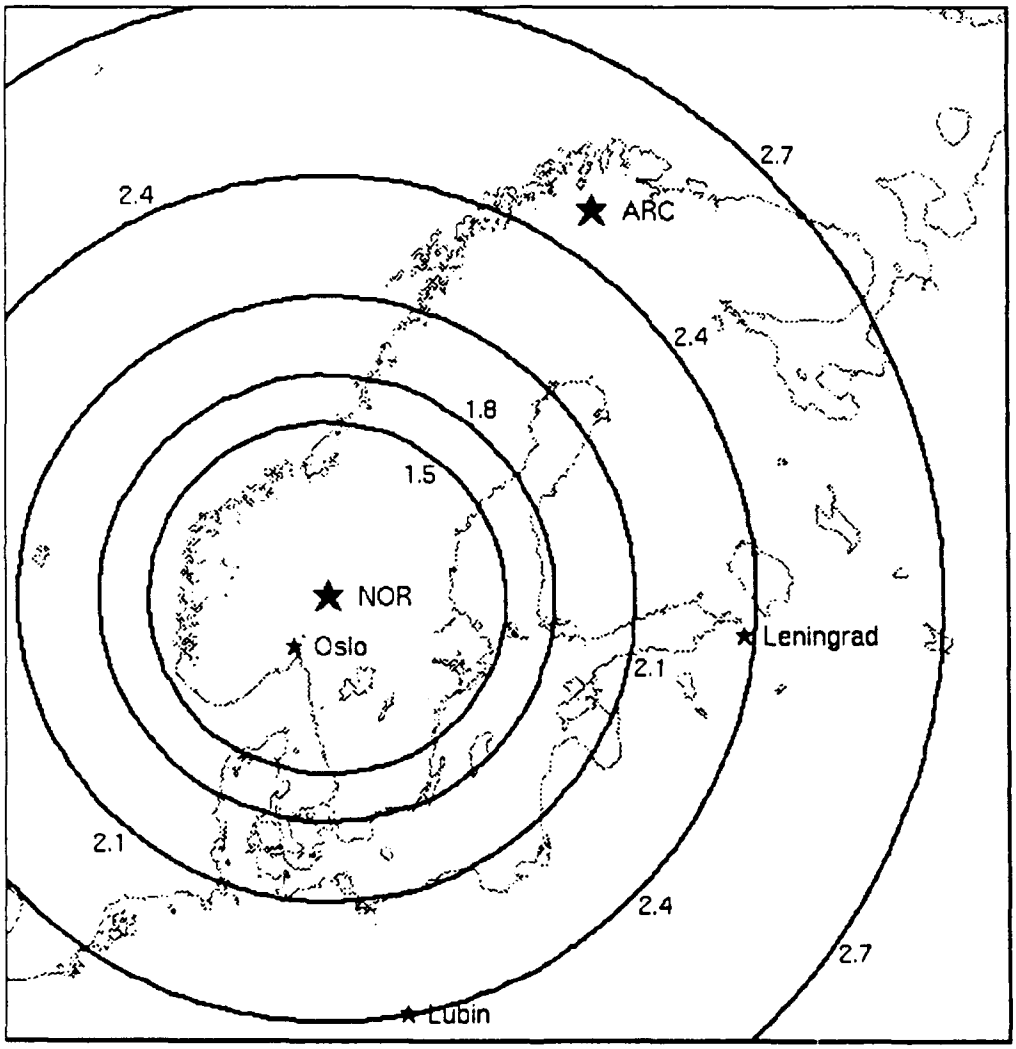

Figure 5.3. Estimate of the 90% M_L threshold for detecting P or secondary phases at NORESS.

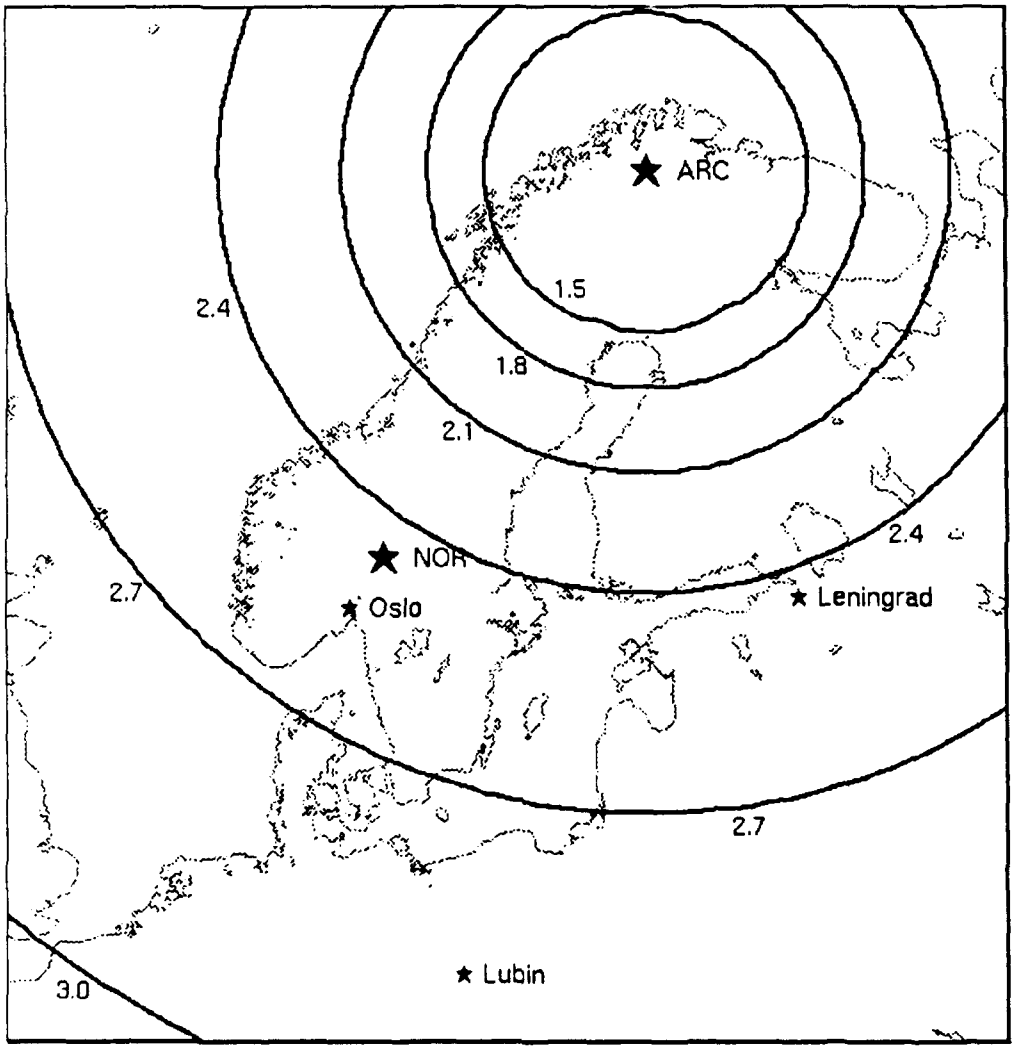

Figure 5.4. Estimate of the 90% M_L threshold for *P*-wave detection at ARCESS.

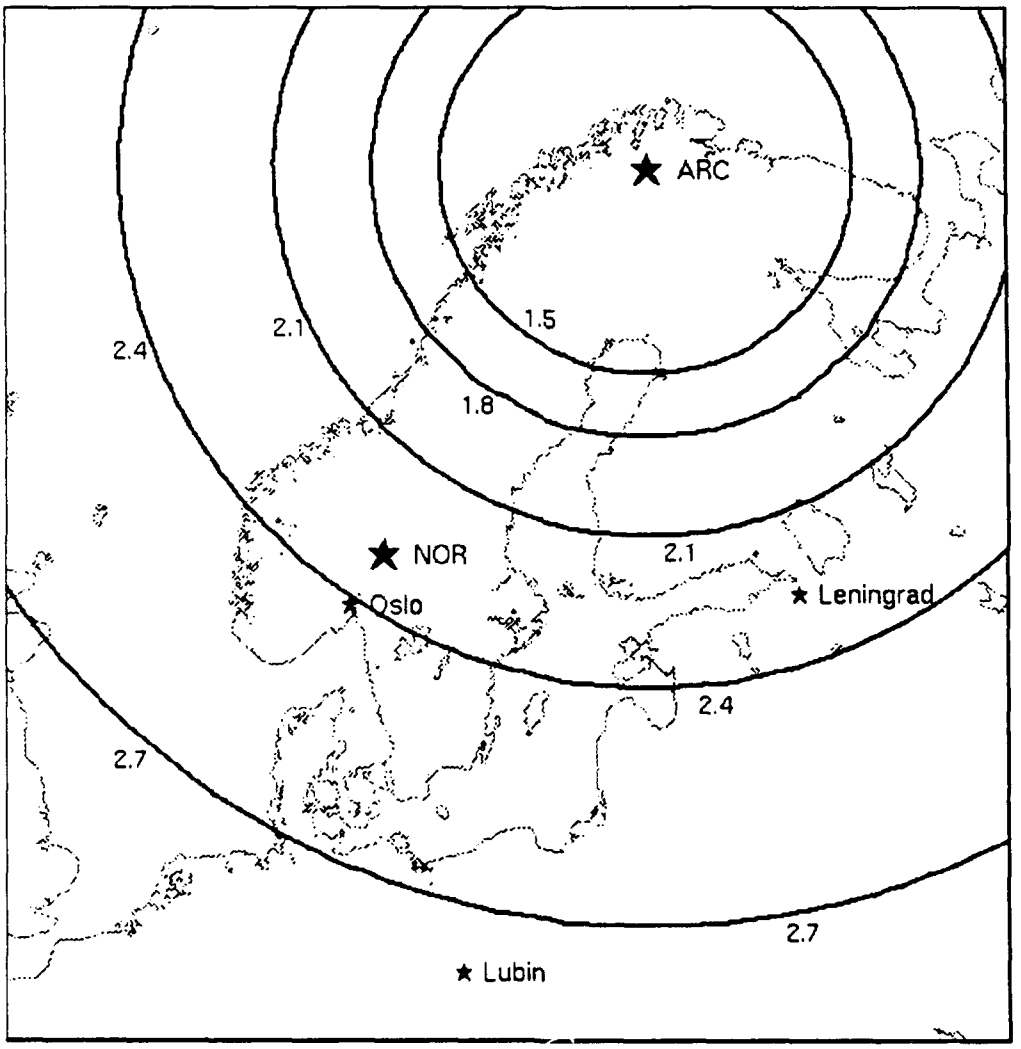

Figure 5.5. Estimate of the 90% M_L threshold for detecting P or secondary phases at ARCESS.

P-type phase (*Pn* or *Pg*) and one *S*-type phase (*Sn* or *Lg*). These are plotted in Figures 5.6 and 5.7 for NORESS and ARCESS, respectively. The 90% detection thresholds at 1000 km for events that can be located with data from one array are about M_L 2.8 at NORESS and M_L 2.5 at ARCESS.

5.3 Detection Threshold for a Regional Network in Fennoscandia

Figure 5.8 shows the simulated 90% M_L detection threshold for NORESS and ARCESS together. We require that both *Pg* and *Lg* be detected at one station for close events (≤ 200 km), or that 3 phases (at least one at each array) be detected for more distant events. These are considered to be the minimum data required for accurate location. The threshold is M_L 2.4–2.6 for events in mining regions near Estonia and Leningrad. *Bratt et al.* [1990] compared detection lists from the *IMS* at NORESS and ARCESS to the Helsinki Bulletin to estimate the capability of these arrays to detect events in the region bounded by 59–66° N and 23–31° E. Most of the events they considered were > 800 km from either array. They found that three phases are detected at NORESS and ARCESS for 83% of the events with $M_L > 2.5$, which agrees well with our simulation in Figure 5.8.

5.4 Location Capability

The location capability of NORESS and ARCESS is estimated using the probability-weighted approach described in the original *SNAP/D* documentation [*Ciervo et al.*, 1985]. Each phase has a probability of detection (≤ 100 %) at individual stations in the network, but in practice a phase is either detected and used in the location solution or it is not detected and cannot be used to constrain location. The probability-weighted approach approximates the effect of undetected phases by weighting the standard deviation of each datum σ by the square root of the probability P_{ijk} that the station in question will detect that phase. The effective standard deviations ($\sigma / \sqrt{P_{ijk}}$) are increased for phases with low probability of detection, and therefore these phases do not contribute much to constraining the event location.

The lengths of the semi-major and semi-minor axes of the location error ellipse at the 90% confidence level for events at the detection threshold of the NORESS/ARCESS network are plotted in Figures 5.9 and 5.10. These simulations are based on our estimates of the azimuth and arrival time standard deviations given in Tables 2.1 and 2.7. Note that we don't include the modeling error in the arrival time standard deviation, since this can be reduced by including station or source corrections. The simulations predict relatively large location uncertainty for events close to one array. For example, the lengths of the semi-major and semi-minor axes for events near Oslo, Norway are about 45 km and 28 km, respectively. This is because detection at close distances is based on two phases recorded at one station (*Pg* and *Lg*), whereas detection at larger distances requires three phases and at least one phase at each array. This means that fewer data are available to locate events close to one array, and azimuth data are as important as arrival times for the location solution.

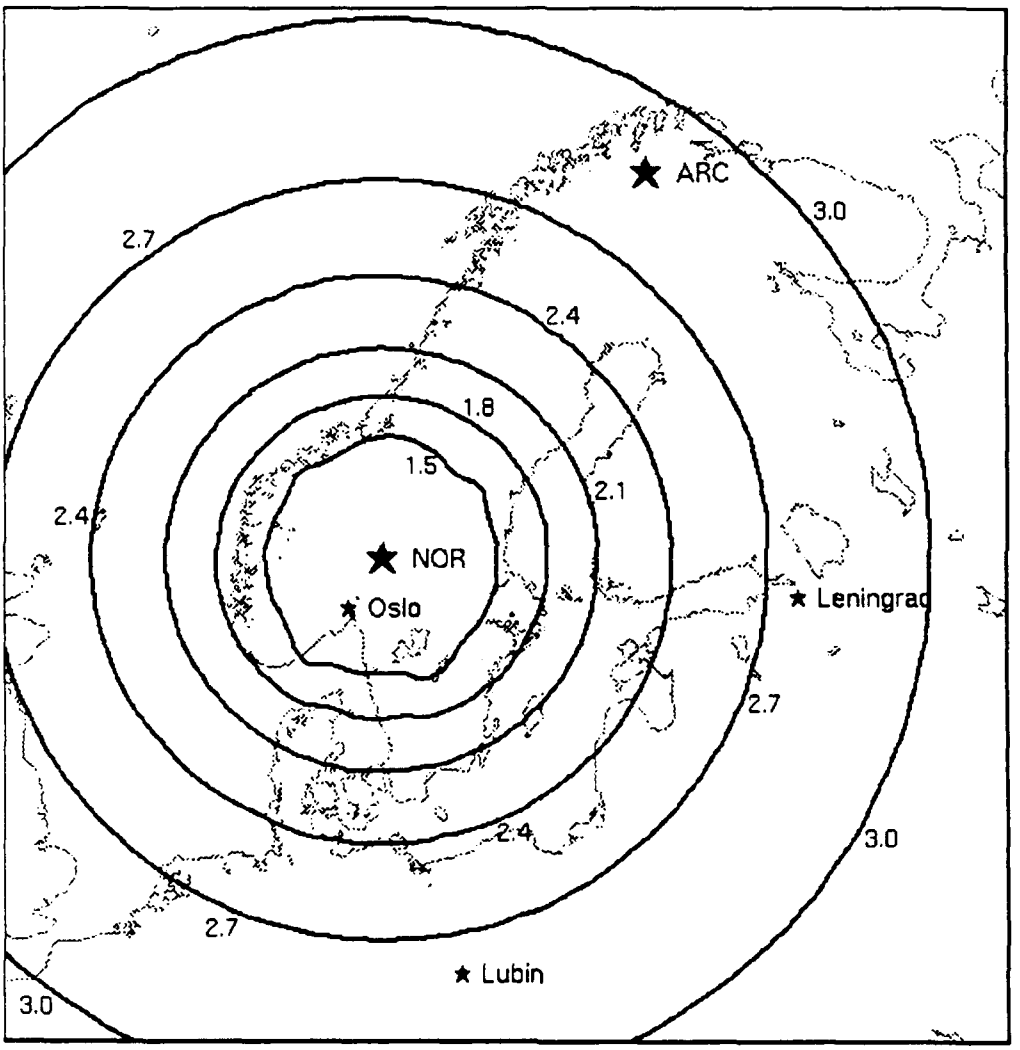

Figure 5.6. Estimate of the 90% M_L threshold for detecting one *P*-type phase (*Pn* or *Pg*) and one *S*-type phase (*Sn* or *Lg*) at NORESS. The irregular shape of the contour closest to the array is caused by insufficient epicenter grid sampling, and has no physical significance.

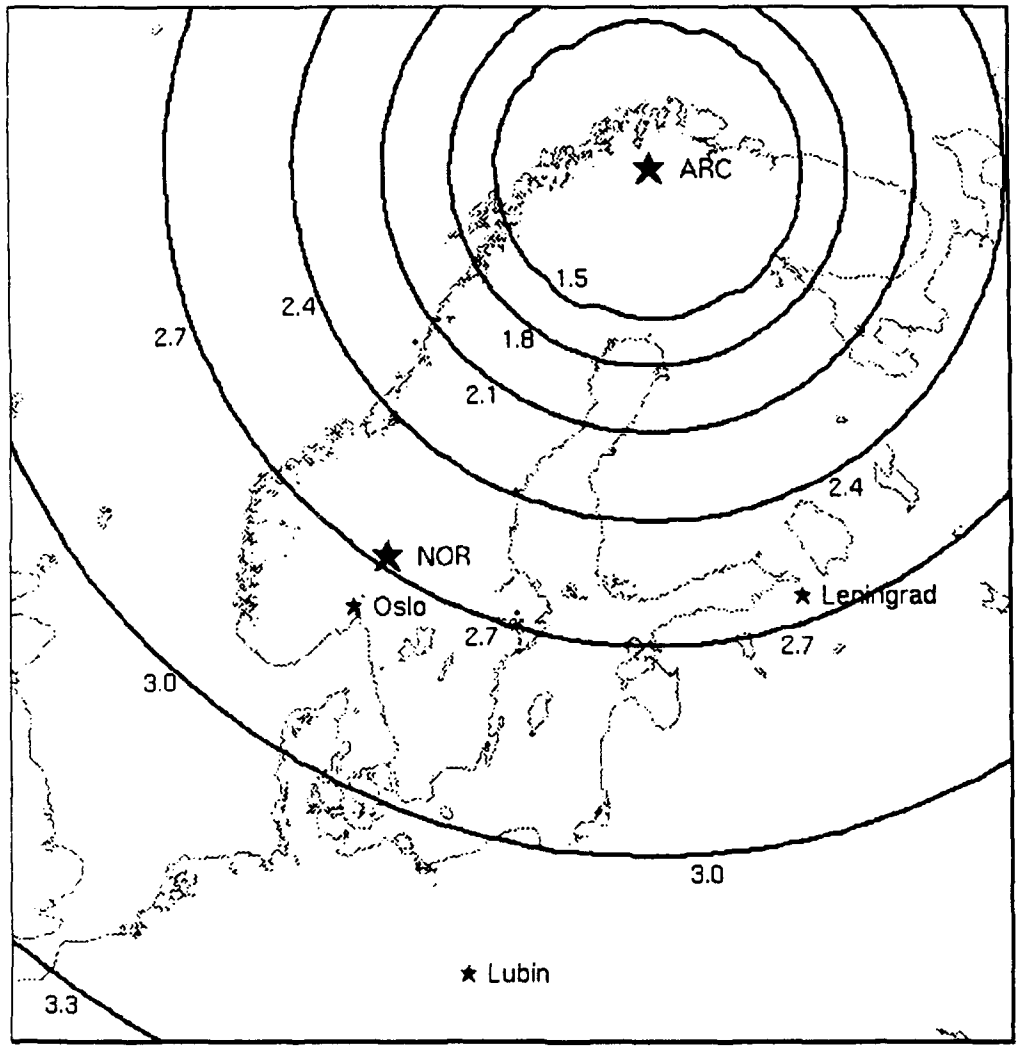

Figure 5.7. Estimate of the 90% M_L threshold for detecting one *P*-type phase (*Pn* or *Pg*) and one *S*-type phase (*Sn* or *Lg*) at ARCESS. The irregular shape of the contour closest to the array is caused by insufficient epicenter grid sampling, and has no physical significance.

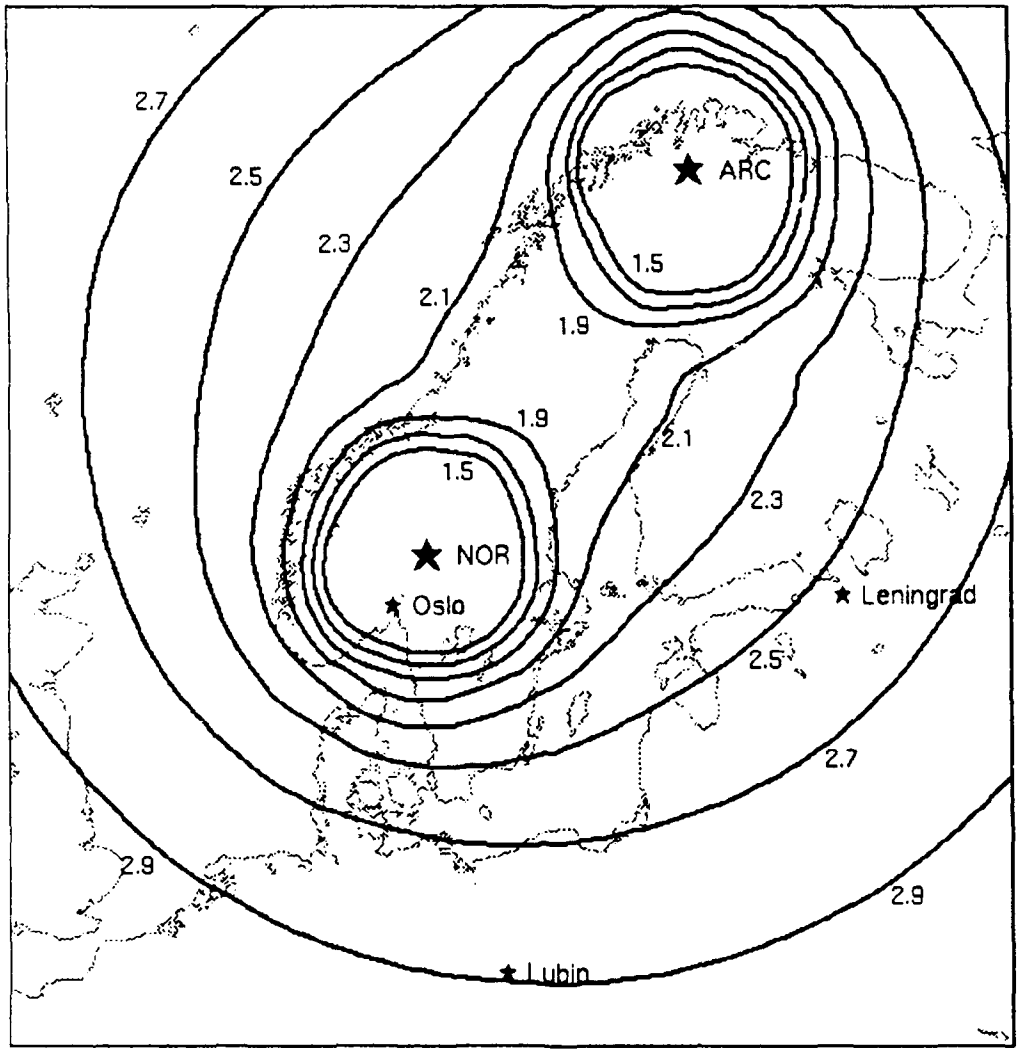

Figure 5.8. Estimate of the 90% M_L detection threshold for the NORESS/ARCESS regional network. Either *Pg* and *Lg* must be detected at one array, or three phases must be detected by two arrays (with at least one at each array).

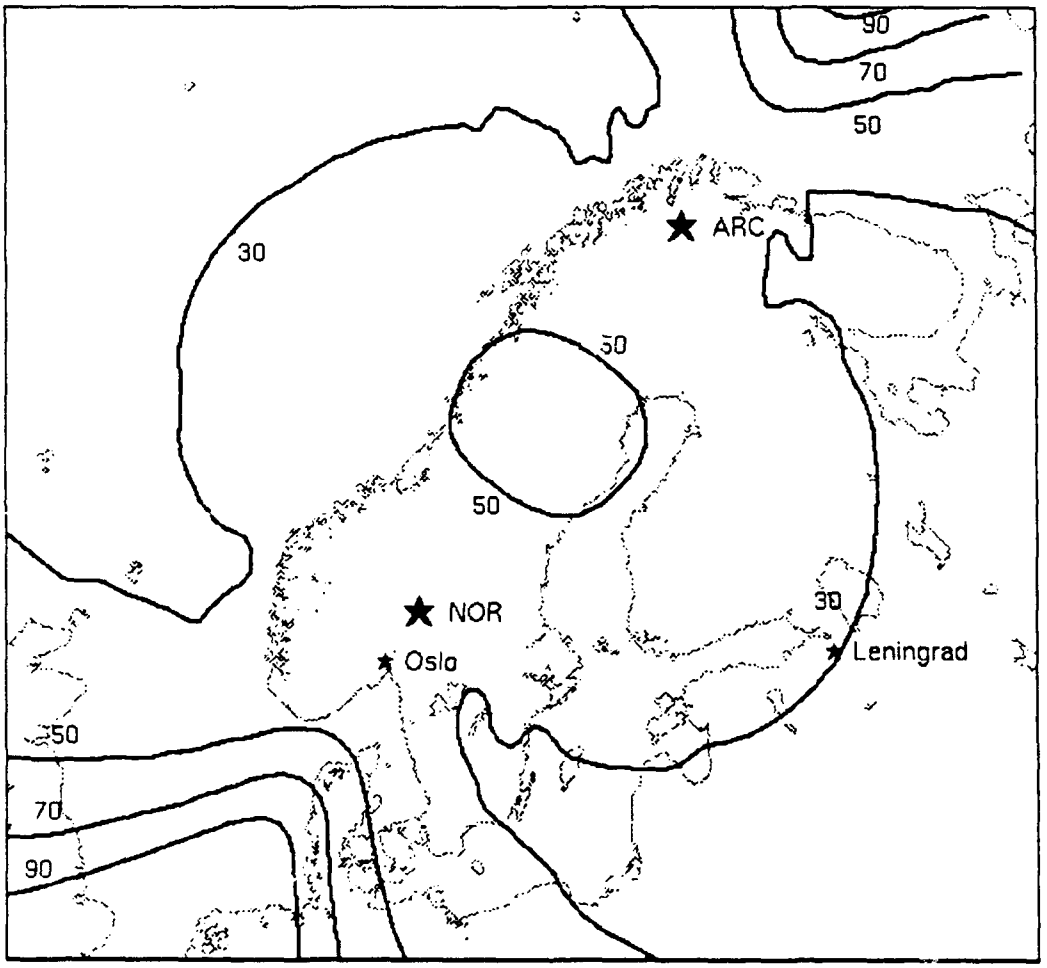

Figure 5.9. The 90th percentile semi-major axis in kilometers is contoured for events at the NORESS/ARCESS detection threshold. The irregular shape of the contours is caused by inadequate epicenter grid sampling, and has no physical significance.

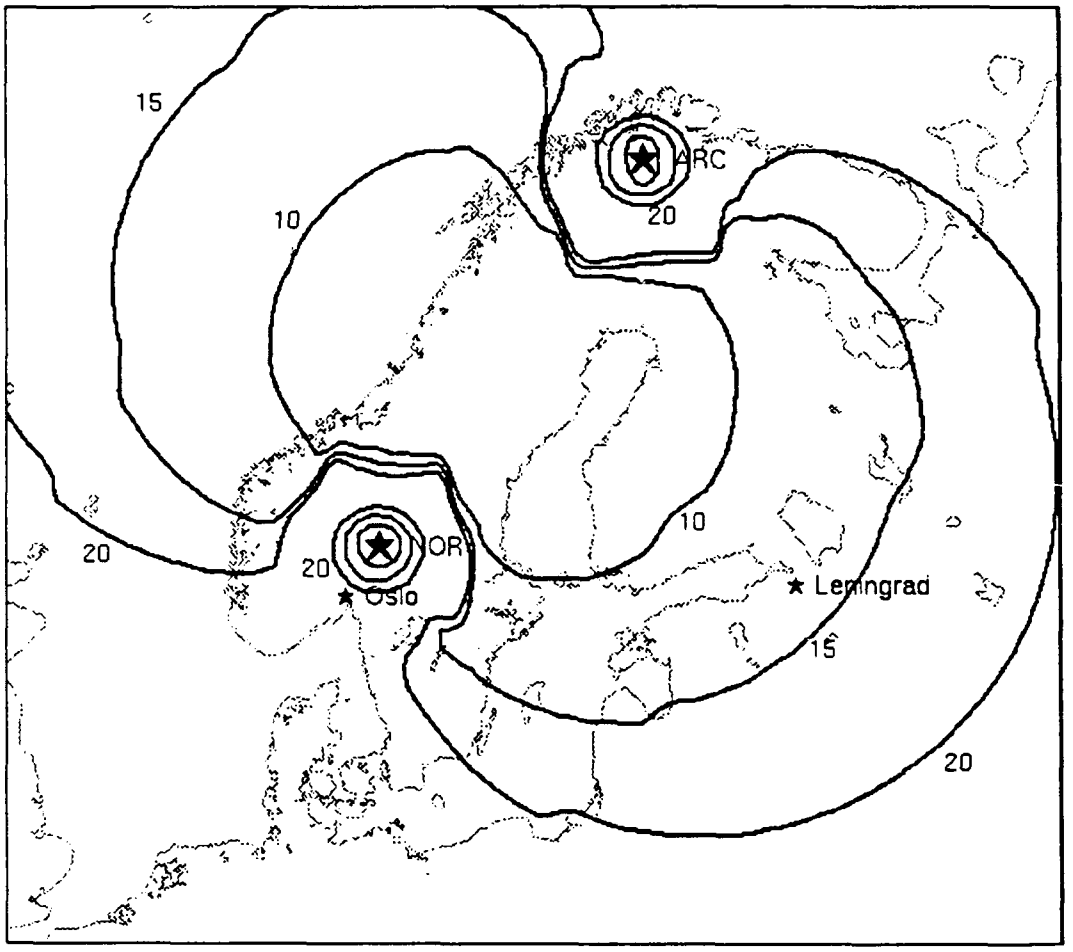

Figure 5.10. The 90th percentile semi-minor axis in kilometers is contoured for events at the NORESS/ARCESS detection threshold. The irregular shape of the contours is caused by inadequate epicenter grid sampling, and has no physical significance.

Our estimates for the location uncertainty are generally lower than estimates derived from empirical studies. For example, *Bratt et al.* [1990] estimate the "error" in the two-array locations compared to locations in the Helsinki Bulletin for 114 events in the region bounded by 59–66° N and 23–31° E. They find that the median separation between the two locations is 23.5 km. Our estimate for the "location error" at the 90% confidence level for events near the center of this region is 27.3 km, and our estimate of the median "location error" is 12.1 km. However, the empirical study by *Bratt et al.* [1990] may underestimate the location capability because they use the mine locations in the Helsinki Bulletin which are different from the mine locations determined from satellite imagery by an average distance of 11 km [*Fox*, 1989]. Also, our simulations are for events recorded by both NORESS and ARCESS, and the study by *Bratt et al.* [1990] included events with single-array locations. Therefore, it is not surprising that our simulations predict better location capability than the results of their empirical study.

Master event techniques greatly improve location accuracy because the modeling error can essentially be removed by locating events relative to nearby events with well-constrained locations (see *Bratt and Bache* [1988] for references to master event location). To quantify this, we determine the sensitivity of the location accuracy to our assumed values of the arrival time and azimuth standard deviations. Table 5.2 lists the location uncertainty as a function of arrival time standard deviation for two epicentral regions (Oslo and Leningrad), assuming that the azimuth standard deviation (σ_α) for each phase is 7°. Table 5.3 is the same, except σ_α is assumed to be 3.0°. For events near Oslo recorded at NORESS, one dimension of the error ellipse is controlled by the azimuth uncertainty, and it is 27.5 km for σ_α = 7° and 11.8 km for σ_α = 3°. The other dimension of the error ellipse is controlled by the arrival time uncertainty for shear phases, and it is 45–49 km for $\sigma_t(S)$ = 2.5 s and 20–28 km for $\sigma_t(S)$ = 1.0 s. The "location error" at the 90% confidence level (which can be calculated from the semi-major and semi-minor axes) for events near Oslo is greater than 15 km for each simulation in Tables 5.2 and 5.3. In order to reduce this to less than 15 km at this distance, the master event technique must reduce the arrival time standard deviation for shear waves to < 1.0 s and the azimuth standard deviation to < 4° for all phases. Detection at two arrays gives much more accurate locations, as can be seen in the tables. Note that the location uncertainty for events near Leningrad (about 1000 km from each array) is nearly independent of the azimuth standard deviation (e.g., compare Tables 5.2 and 5.3). For these events, the arrival time standard deviations for shear phases must be < 1.5 s to achieve a location uncertainty of < 15 km at the 90% confidence level.

Table 5.2 Location uncertainty at the 90% confidence level (σ_α = 7.0°).

σ_t (s)		Location Uncertainty (km)			
		Oslo[1]		Leningrad[2]	
P Waves	*S* Waves	*smaj*	*smin*	*smaj*	*smin*
1.0	2.5	48.4	27.5	33.6	17.6
1.0	2.0	40.3	27.5	28.2	15.6
1.0	1.5	32.7	27.5	23.1	12.9
1.0	1.0	27.5	25.9	18.3	9.4
0.7	2.5	46.5	27.5	32.2	14.2
0.7	2.0	38.0	27.5	26.5	13.1
0.7	1.5	29.8	27.5	20.9	11.4
0.7	1.0	27.5	22.1	15.7	8.7
0.5	2.5	45.6	27.5	31.5	11.1
0.5	2.0	36.9	27.5	25.6	10.5
0.5	1.5	28.4	27.5	19.8	9.5
0.5	1.0	27.5	20.1	14.2	7.8

1. Two phases required for detection (*Pg* and *Lg* at NORESS). Events are about 150 km from NORESS.
2. Three phases required for detection, and at least one phase at each array. Events are about 1000 km from each array.

Table 5.3 Location uncertainty at the 90% confidence level (σ_α = 3.0°).

σ_t (s)		Location Uncertainty (km) Oslo[1]		Leningrad[2]	
P Waves	*S* Waves	*smaj*	*smin*	*smaj*	*smin*
1.0	2.5	48.4	11.8	32.4	17.1
1.0	2.0	40.3	11.8	27.5	15.3
1.0	1.5	32.7	11.8	22.7	12.7
1.0	1.0	25.9	11.8	18.1	9.3
0.7	2.5	46.5	11.8	31.1	14.0
0.7	2.0	38.0	11.8	25.9	11.7
0.7	1.5	29.8	11.8	20.6	11.3
0.7	1.0	22.1	11.8	15.5	8.7
0.5	2.5	45.6	11.8	30.5	10.9
0.5	2.0	36.9	11.8	25.0	10.4
0.5	1.5	28.4	11.8	19.5	9.5
0.5	1.0	20.1	11.8	14.1	7.8

1. Two phases required for detection (*Pg* and *Lg* at NORESS). Events are about 150 km from NORESS.
2. Three phases required for detection, and at least one phase at each array. Events are about 1000 km from each array.

6. PROPAGATION AND SOURCE MEDIA GRIDS FOR EURASIA

The ultimate objective of this project is to simulate the detection and location capability of regional seismic networks in and around the Soviet Union. It is important to include lateral variations in propagation characteristics to obtain accurate simulations for such a large area. For example, it is well known that first order variations in regional wave propagation are related to geologic and tectonic features. Therefore, in Section 6.1 we use a tectonic map of Eurasia to develop a propagation grid on a 5°×5° scale. We associate orogenic zones with higher attenuation than areas characterized as continental plateaus. Source coupling is also important for accurate simulations. However variations in surface geology occur at a much smaller scale than the 5°×5° grid that we use in *NetSim*. Therefore, in Section 6.2 we use a map of the surface geology of Eurasia as a guide to identify potential sites for cavity decoupling (e.g., regions of bedded or domed salt).

6.1 Propagation Grid

Our propagation grid is based on the 5°×5° global tectonic regionalization, GTR1, developed by *Jordan* [1981]. He defines three oceanic provinces based on crustal age (0–25 m.y., 25–100 m.y., and > 100 m.y.), and three continental provinces based on tectonic behavior during the Phanerozic (Precambrian shields and platforms, Phanerozic platforms, Phanerozic orogenic zones and magmatic belts). We use this grid to characterize lateral variations in regional wave propagation. First, we simplify the grid by including only two provinces, stable and tectonic. We associate Precambrian shields, Phanerozic platforms, and oceanic regions > 100 m.y. with the stable province (lower attenuation), and orogenic zones and magmatic belts, and oceanic regions < 100 m.y. with the tectonic province (higher attenuation). This grid is plotted in Figure 6.1. We assume that paths to NORESS and ARCESS are representative of wave propagation in stable provinces, and we will determine the sensitivity of the simulations to assumptions regarding the attenuation in tectonic provinces (since attenuation estimates are not available for these regions).

Our primary interest is in Eurasia, so we examine this area in more detail by comparing GTR1 with a tectonic map of the Soviet Union [*Ministry of Geology, Academy of Science and Ministry of Education SSSR*, 1961]. Figure 6.2 reproduces the major features of this tectonic map. We develop a 5°×5° grid based on associating continental plateaus with the stable province and all other regions with the tectonic province (Figure 6.3). This grid differs from GTR1 in few places, but the major tectonic features are the same. The tectonic provinces include the Ural and Himalaya mountain ranges, the southern and eastern boarders of the USSR, and island arcs. We will use this grid for our simulations of the detection and location capability of regional networks in the Soviet Union.

PROPAGATION GRID

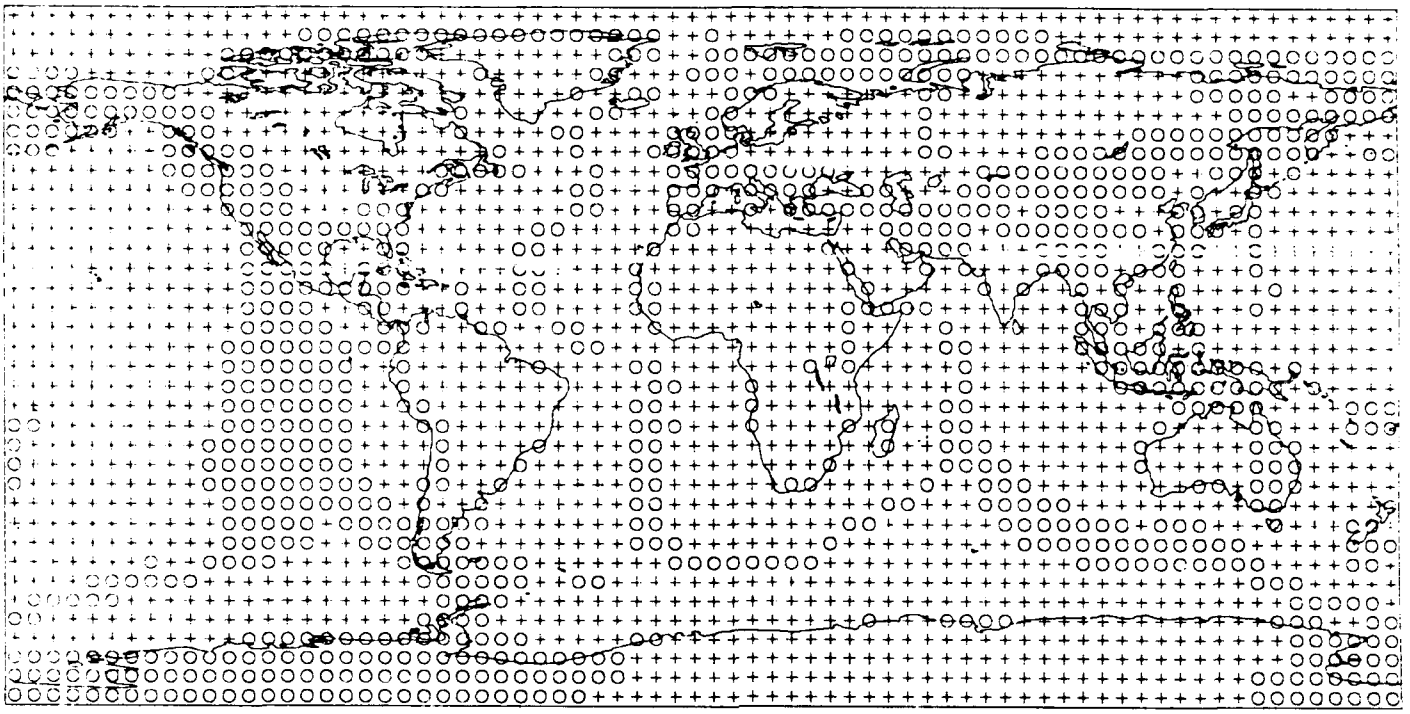

Figure 6.1. The propagation grid is plotted on a 5°×5° scale. Stable provinces are indicated by a plus symbol in each grid cell, and tectonic provinces are indicated by a circle in each grid cell. This grid is a simplification of the global tectonic regionalization, GTR1, developed by *Jordan* [1981].

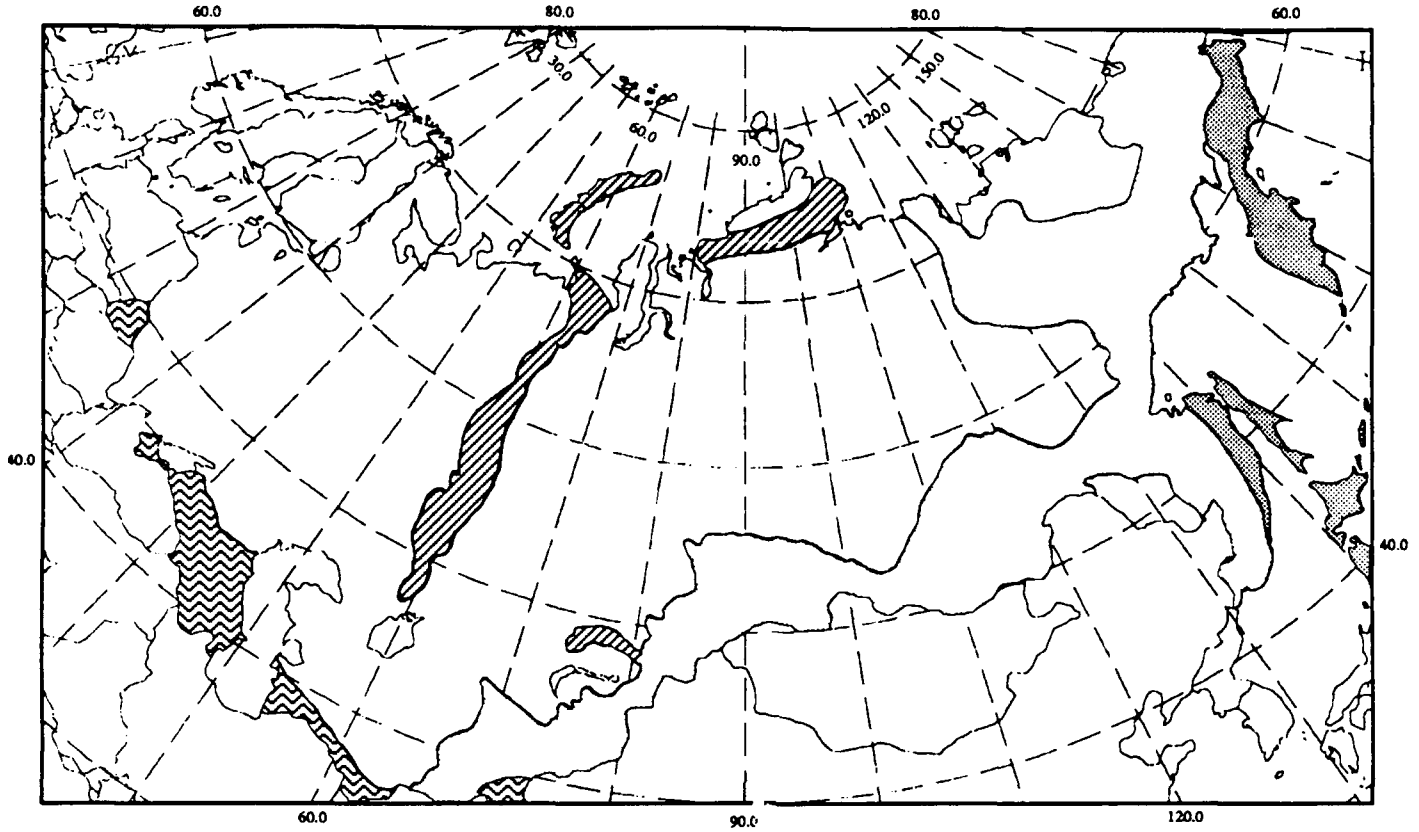

LEGEND:

- Continental Plateau
- Orogenic zones with relatively small movements
- Regions of intense orogeny in Precambrian, Paleozoic and Mesozoic
- Regions of intense Orogeny in zones of Alpine folding
- Island Arc

Figure 6.2. Tectonic regionalization of Eurasia from *Ministry of Geology, Academy of Science and Ministry of Education, SSSR* [1961].

PROPAGATION GRID - EURASIA

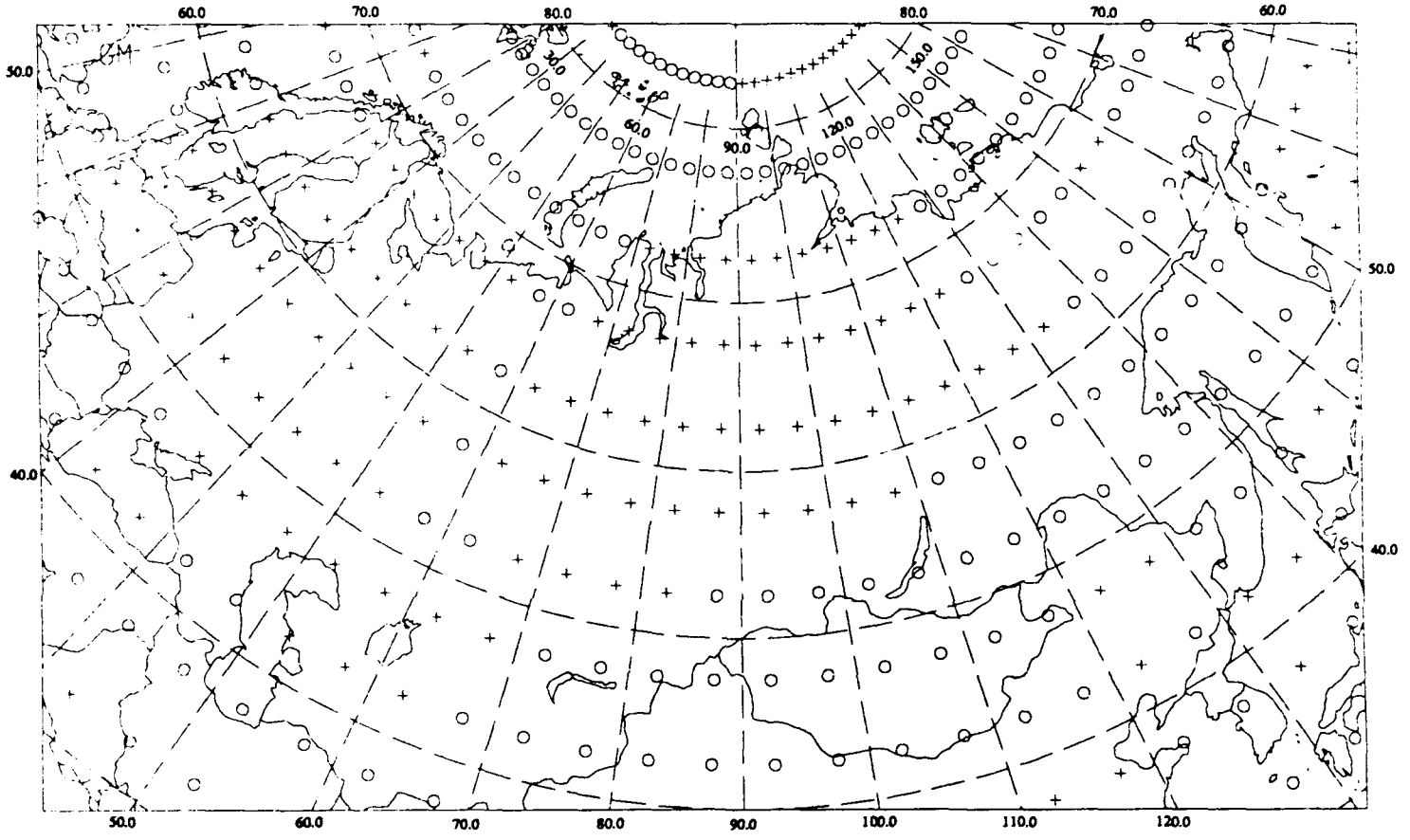

Figure 6.3. This propagation grid for Eurasia is based on the tectonic regionalization in Figure 6.2. Stable provinces are indicated by a plus symbol in each grid cell, and tectonic provinces are indicated by a circle in each grid cell.

6.2 Source Medium Grid

It is well known that seismic waves emanating from explosions detonated in a large underground cavity are smaller than those from tamped explosions with the same yield. The cavity volume required for full decoupling increases proportionally with the explosion yield, and decreases as the strength of the rock increases [for review, see *OTA Report*, 1988]. Construction of cavities large enough for explosion decoupling is possible in regions of bedded or domed salt or crystalline rock (about 25 m radius in salt and 20 m in granite). In this section, we develop a source medium grid for Eurasia on a 5°× 5° scale to identify potential sites of cavity decoupling (e.g. regions of bedded or domed salt and crystalline rock). This grid is based primarily on an atlas of Asia and eastern Europe compiled by *Alverson et al.* [1967], which includes a map of the surface geology. We also use a map of USSR salt deposits compiled by *Rachlin* [1985], and a draft version of 1°×1° grid indicating regions of domed and folded salt provided to us by Bill Leith at the USGS. Our source medium grid is plotted in Figure 6.4. Most of the salt regions consist of bedded salt. The largest volume of salt domes and anticlines is just north of the Caspian Sea. Of course, variations in surface geology occur at a much smaller scale than the 5°×5° grid that we use for network simulation. The purpose of this grid is to identify regions that may require higher station density to verify compliance with a threshold test ban treaty. We will estimate station locations and parameters required for detection of 1-kt tamped and decoupled explosions in regions where cavity construction is feasible.

Thomas J. Sereno, Jr.
Donna J. Williams

SOURCE GRID

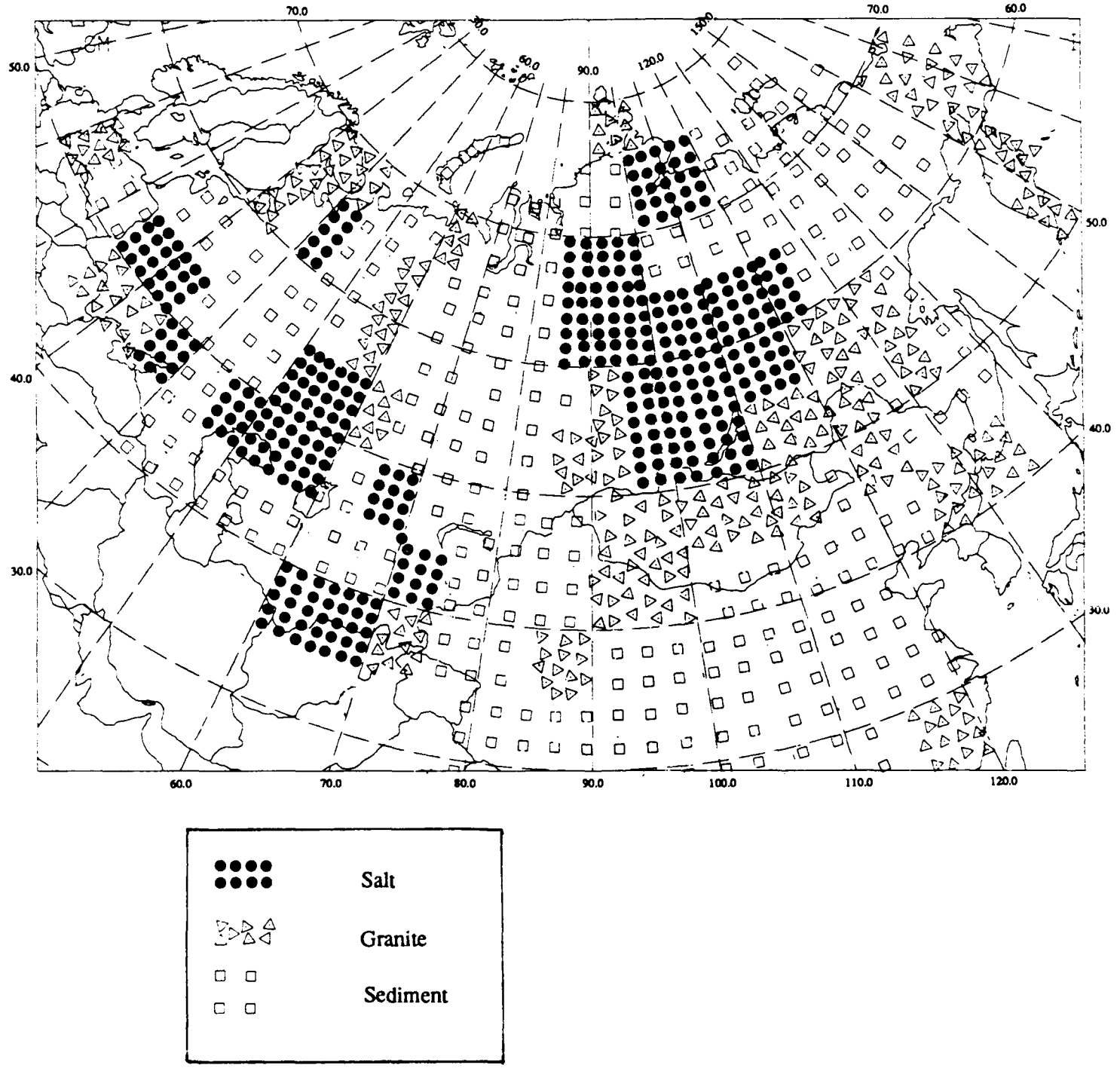

Figure 6.4. The source medium grid is plotted on a 5°×5° scale. The purpose of this grid is to identify potential sites for cavity decoupling (crystalline rocks or salt). No distinction is made between different ages or types of sedimentary deposits.

7. SUMMARY

The primary objective is to simulate the detection and location capability of seismic networks that include regional stations and arrays in and around the Soviet Union. This report summarizes several studies of important issues that are involved in normalizing these simulations. The normalization is based on data recorded by the NORESS and ARCESS arrays in Norway because of the size and quality of the data set and the fact that independent networks provide accurate locations of regional events. We start by estimating the normalization parameters (e.g., frequency-dependent attenuation, source scaling, noise spectra for primary and secondary phases) using data recorded by these arrays. Next, we use the normalized simulation method to predict the detection and location capability of NORESS and ARCESS. Finally, we validate the normalization by comparing the simulations to the capability actually achieved by these arrays. This method is shown to give accurate results for NORESS and ARCESS, so we are confident that we can use it to determine the sensitivity to various network parameters (e.g., number of stations, number of arrays versus single stations, station noise levels, etc). The next step is to extrapolate the NORESS/ARCESS results to simulate the detection and location capability of hypothetical networks in the Soviet Union.

(THIS PAGE INTENTIONALLY LEFT BLANK)

ACKNOWLEDGMENTS

I thank Thomas Bache for his careful review of this report, and Henry Swanger for many helpful suggestions and discussions. I am also grateful to Donna Williams who did nearly all of the data processing, and analysis of geologic and tectonic maps of Eurasia. I thank Bill Leith at the United States Geological Survey for providing me with an atlas of Asia and eastern Europe, and for his regionalization of domed and folded salt in the Soviet Union. This research was funded by the Defense Advanced Research Projects Agency under Contract F08606-88-C-0033 and monitored by Air Force Technical Applications Center.

(THIS PAGE INTENTIONALLY LEFT BLANK)

REFERENCES

Aki, K., and P. Richards, *Quantitative Seismology: Theory and Methods*, W. H. Freeman, San Francisco, Calif., 1980.

Alverson, D., D. Cox, A. Woloshir, M. Terman, and C. Woo, *Atlas of Asia and Eastern Europe to support detection of underground nuclear testing*, vol. 2, *Tectonics*, U.S. Geological Survey, Washington D.C., 1967.

Bache, T., P. Marshall, and L. Bache, *Q* for teleseismic *P* waves from central Asia, *J. Geophys. Res.*, *90*, 3575–3587, 1985.

Bache, T., S. Bratt, J. Wang, R. Fung, C. Kobryn, and J. Given, The intelligent monitoring system, *Bull. Seismol. Soc. Am.*, [in press], 1990a.

Bache, T. and SAIC Staff, Intelligent array system: System introduction and functional description, *SAIC Technical Report*, Sci. Appl. Int. Corp., San Diego, Calif., 1990b.

Bratt, S. and T. Bache, Locating events with a sparse network of regional arrays, *Bull. Seismol. Soc. Am.*, *78*, 780–798, 1988.

Bratt, S., T. Bache, D. Williams, Seismic monitoring capability in the Soviet Union using hypothetical regional networks, *Final Tech. Rep. SAIC 87/1752*, Sci. Appl. Int. Corp., San Diego, Calif., AFGL-TR-87-0244, 1987.

Bratt, S., H. Swanger, R. Stead, F. Ryall, and T. Bache, Initial results from the intelligent monitoring system, *Bull. Seismol. Soc. Am.*, [in press], 1990.

Bungum, H., S. Vaage, and E. Husebye, The Meløy earthquake sequence, northern Norway; Source parameters and their moment scaling relations, *Bull. Seismol. Soc. Am.*, *72*, 197–206, 1982.

Bungum, H., S. Mykkeltveit, and T. Kvaerna, Seismic noise in Fennoscandia, with emphasis on high frequencies, *Bull. Seismol. Soc. Am.*, *75*, 1489–1515, 1985.

Chun, K., Kokoski, R., and G. West, High-frequency *Pn* attenuation in the Canadian Shield, *Bull. Seismol. Soc. Am.*, *79*, 1039–1053, 1989.

Ciervo, A., S. Sanemitsu, D. Snead, R. Suey, and A. Watson, User's manual for *SNAP/D*: seismic network assessment program for detection, *Pacific-Sierra Research Corporation, Report 1027B*, 1985.

Fox, W., Satellite imagery of areas in northwest Europe, *SAIC Technical Report*, Sci. Appl. Int. Corp., San Diego, Calif., 1989.

Fyen, J., NORESS noise spectral studies, preliminary report, *Sci. Rep. 2-85/86*, NTNF/NORSAR, Kjeller, Norway, 1986.

Fyen, J. NORESS noise spectral studies: Noise level characteristics, *Sci. Rep. 2-86/87*, NTNF/NORSAR, Kjeller, Norway, 1987.

Gibowicz, S., NORESS capability for detection and location of mining tremors in the Lubin area of Poland, *Sci. Rep. 2-86/87*, NTNF/NORSAR, Kjeller, Norway, 1987.

Hasegawa, H., *Lg* spectra of local earthquakes recorded by the Eastern Canada Telemetered Network and spectral scaling, *Bull. Seismol. Soc. Am., 73*, 1041–1061, 1983.

Jordan, T., Global tectonic regionalization for seismological data analysis, *Bull. Seismol. Soc. Am., 71*, 1131–1141, 1981.

Kennett, B., On regional S, *Bull. Seismol. Soc. Am., 75*, 1077–1086, 1985.

Kvaerna, T., On exploitation of small-aperture NORESS type arrays for enhanced *P*-wave detectability, *Bull. Seismol. Soc. Am., 79*, 888–900, 1989.

Kvaerna, T., and D. Doornbos, An integrated approach to slowness analysis with arrays and three-component stations, *Sci. Rep. 2-85/86*, NTNF/NORSAR, Kjeller, Norway, 1986.

Kvaerna, T., and S. Mykkeltveit, Optimum beam deployment for NORESS *P*-wave detection, *Sci. Rep. 1-86/87*, NTNF/NORSAR, Kjeller, Norway, 1986.

Kvaerna, T., S. Kibsgaard, and F. Ringdal, False alarm statistics and threshold determination for regional event detection, *Sci. Rep. 1-87/88*, NTNF/NORSAR, Kjeller, Norway, 1987.

Ministry of Geology, Academy of Science and Ministry and Ministry of Education SSSR, *USSR Neotectonic map, 1:5,000,000*, 1961.

Mueller, R., and J. Murphy, Seismic characteristics of underground nuclear detonations, *Bull. Seismol. Soc. Am., 61*, 1675–1692, 1971.

Mykkeltveit, S., A new regional array in Norway: Design work, *Sci. Rep. 2-82/83*, NTNF/NORSAR, Kjeller, Norway, 1983.

Mykkeltveit, S., NORESS real time processing performance for events in western Norway and the North Sea, *Sci. Rep. 2-85/86*, NTNF/NORSAR, Kjeller, Norway, 1986.

Mykkeltveit, S., and F. Ringdal, New results from processing of data recorded at the new ARCESS regional array, *Sci. Rep. 2-87/88*, NTNF/NORSAR, Kjeller, Norway, 1988.

Mykkeltveit, S., F. Ringdal, J. Fyen, and T. Kvaerna, Initial results from analysis of data recorded at the new regional array in Finnmark, Norway, *Sci. Rep. 1-87/88*, NTNF/NORSAR, Kjeller, Norway, 1987.

Office of Technology Assessment, U.S. Congress, Seismic verification of nuclear testing Treaties, *OTA-ISC-361*, Washington D.C., 1988.

Rachlin, J. Cavity construction opportunities in the Soviet Union, Proceedings of the Cavity Decoupling Workshop, Pajaro Dunes, Calif., July 29–31, Editor: Donald Larson, v53–v66, 1985.

Ringdal, F., Real time event detection using the small-aperture NORESS array, *Sci. Rep. 2-84/85*, NTNF/NORSAR, Kjeller, Norway, 1985.

Ringdal, F., Regional event detection using the NORESS array, *Sci. Rep. 2-85/86*, NTNF/NORSAR, Kjeller, Norway, 1986.

Rivers, W., A. Watson, and A. Ciervo, Data base for *SNAP/D*: Seismic network assessment program for detection, *Final Rep. PSR Report 1551*, Pacific-Sierra Research Corp., Los Angeles, Calif., 1985.

Sereno, T., Numerical modeling of *Pn* geometric spreading and empirically determined attenuation of *Pn* and *Lg* phases recorded in eastern Kazakhstan, *Semiannu. Tech. Rep. SAIC 89/1555*, Sci. Appl. Int. Corp., San Diego, Calif., 1989.

Sereno, T., S. Bratt, and T. Bache, Simultaneous inversion of regional wave spectra for attenuation and seismic moment in Scandinavia, *J. Geophys. Res., 93*, 2019-2035, 1988.

Sereno, T., S. Bratt, and G. Yee, *NetSim*: A computer program for simulating detection and location capability of regional seismic networks, *Annu. Tech. Rep. SAIC 90/1163*, Sci. Appl. Int. Corp., San Diego, Calif., 1990.

Sereno, T., and J. Given, *Pn* attenuation for a spherically symmetric earth model, *Geophys. Res. Lett., 17*, 1141–1144, 1990.

Suteau-Henson, A., and T. Bache, Spectral characteristics of regional phases recorded at NORESS, *Bull. Seismol. Soc. Am.*, *78*, 708–725, 1988.

APPENDIX A: SAMPLE FITS TO OBSERVED SPECTRA

This appendix gives examples of the fit of theoretical spectra to observed *Pn*, *Pg*, *Sn*, and *Lg* spectra. The theoretical spectra are based on the inversion results presented in Section 3. Six events are selected at distances between 200 and 1530 km (Figures A.1–A.6). These are representative of the quality of the fit for most of the events used in the inversion. NORESS spectra are plotted on the left of each figure, and ARCESS spectra are plotted on the right. Each panel plots the observed signal spectrum, the "noise" spectrum calculated from a time sample taken just prior to the signal, and the theoretical spectrum based on the inversion results. The noise spectra are normalized to the signal window length for each phase. The map in the upper left corner of each figure shows the event epicenter and station locations. The spectra are plotted between 1 and 15 Hz, but the maximum frequencies considered for *Sn* and *Lg* were 10 Hz and 7 Hz, respectively. In addition, data are included in the inversion only if their *snr* exceeds a predetermined threshold (Section 3).

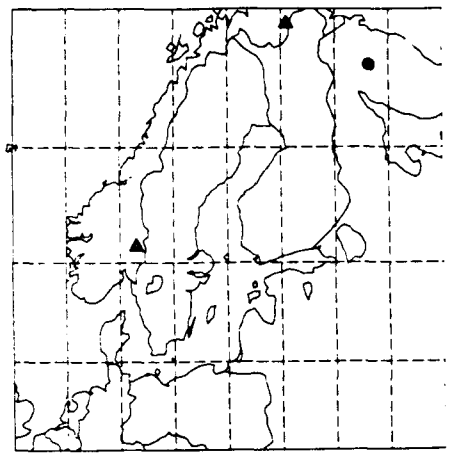

EVENT 8
MINING EXPLOSION (HD6)

(68.1° N, 33.2° E) M_L = 2.8

Δ_{noress} = 1312 km
Δ_{arcess} = 348 km

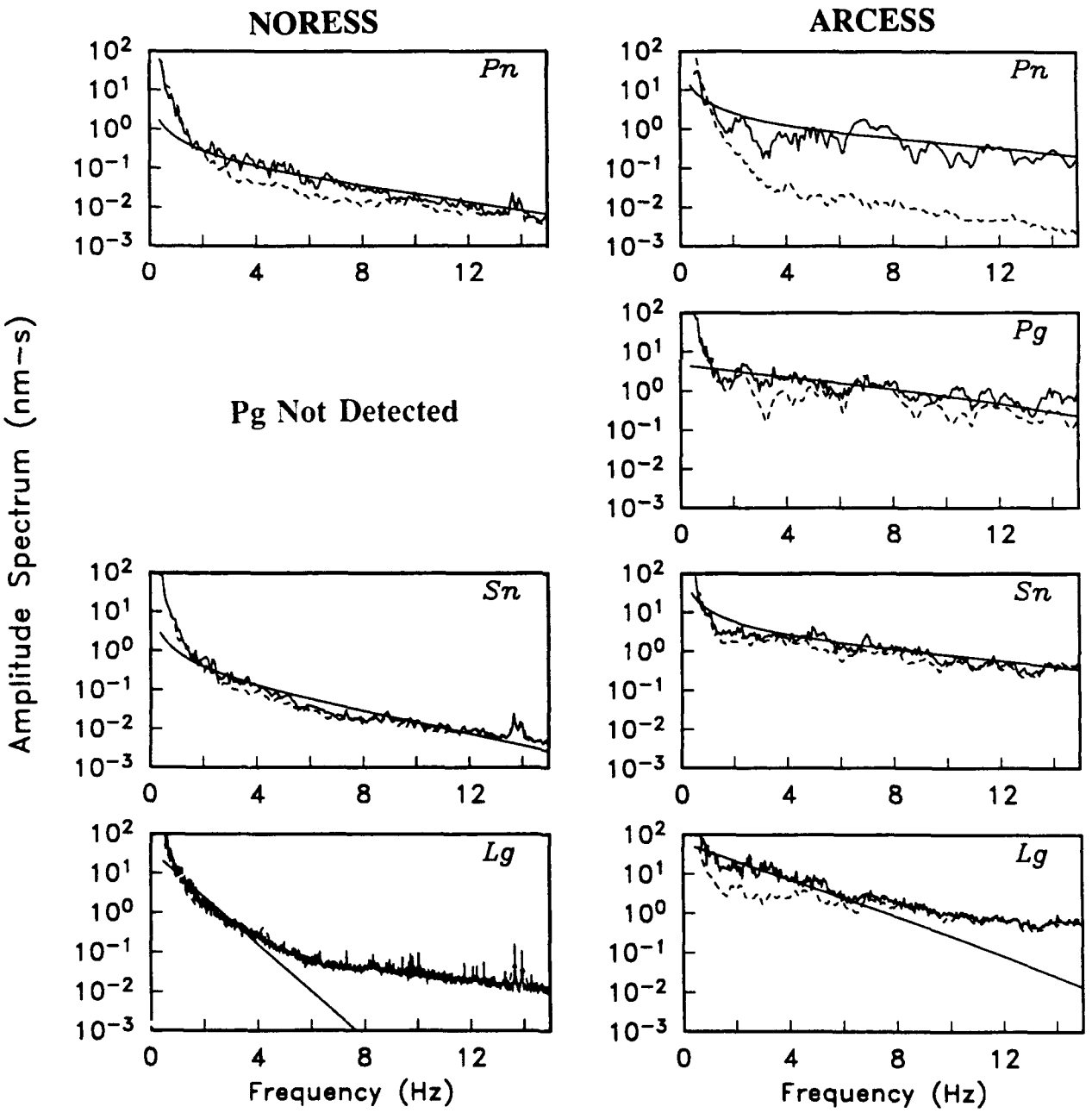

Figure A.1 Theoretical and observed spectra at NORESS and ARCESS for a mining explosion in the Kola Peninsula.

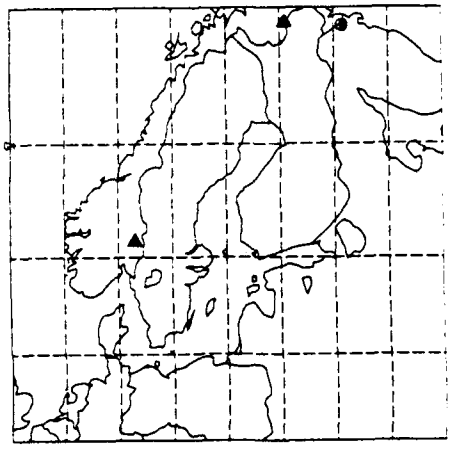

EVENT 57
MINING EXPLOSION (HD2)

(69.4° N, 30.8° E) M_L = 3.1

Δ_{noress} = 1309 km
Δ_{arcess} = 207 km

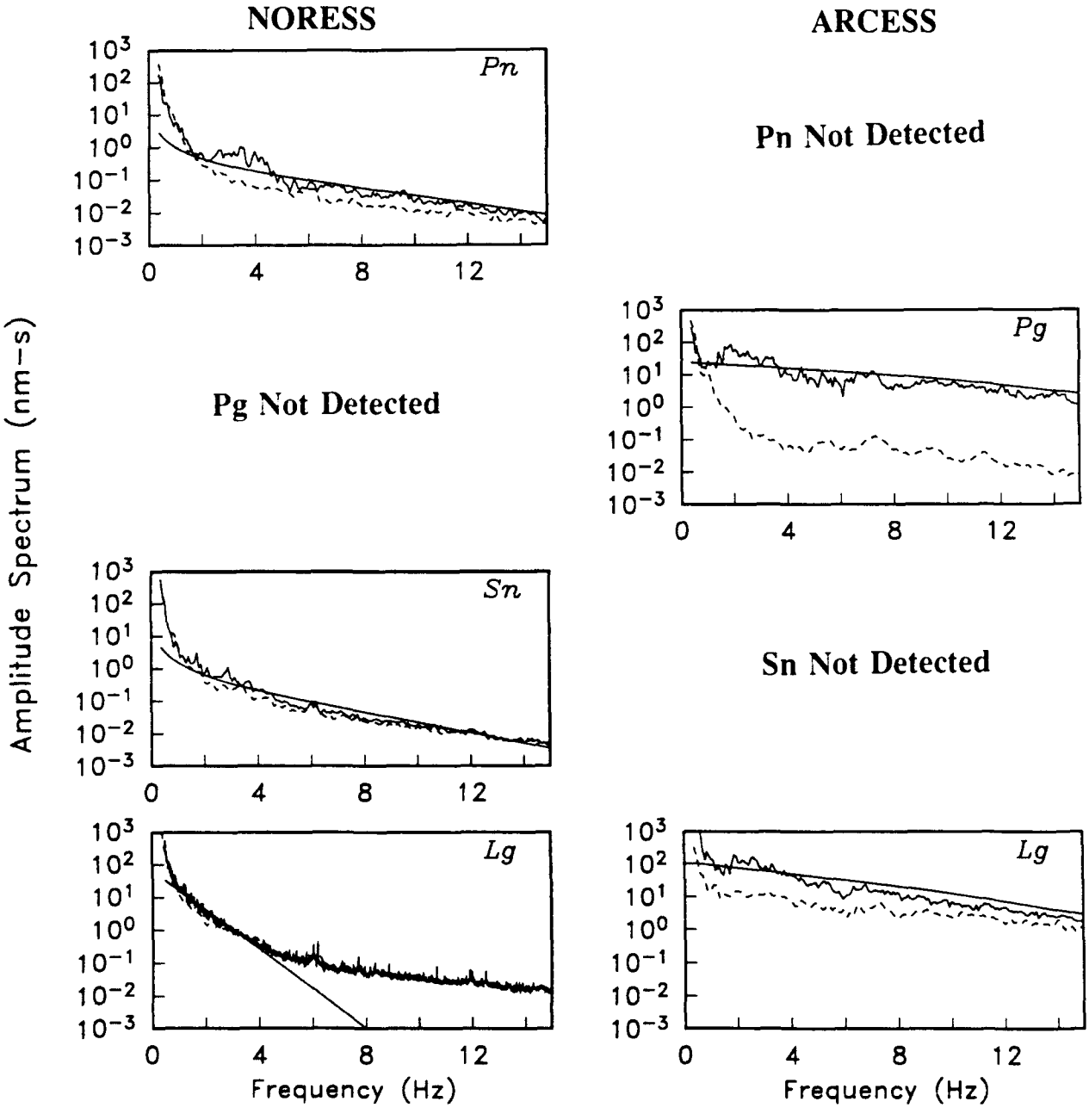

Figure A.2 Theoretical and observed spectra at NORESS and ARCESS for a mining explosion in the Kola Peninsula.

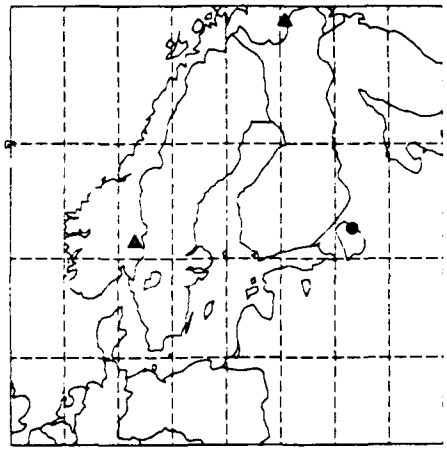

EVENT 61
MINING EXPLOSION (HC14)

(61.4° N, 31.6° E) M_L **= 2.6**

Δ_{noress} **= 1077 km**
Δ_{arcess} **= 946 km**

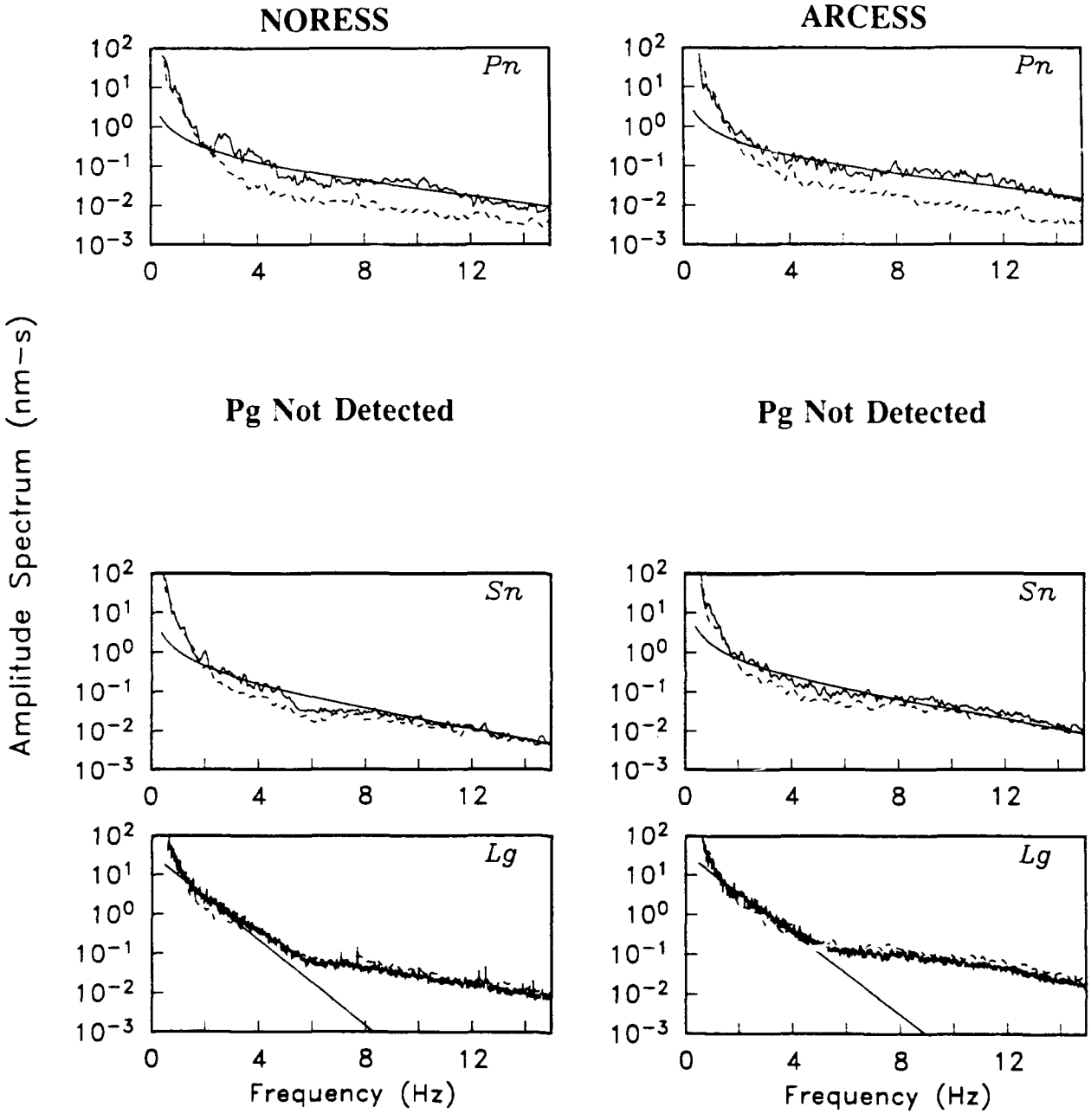

Figure A.3 Theoretical and observed spectra at NORESS and ARCESS for a mining explosion near Leningrad, USSR.

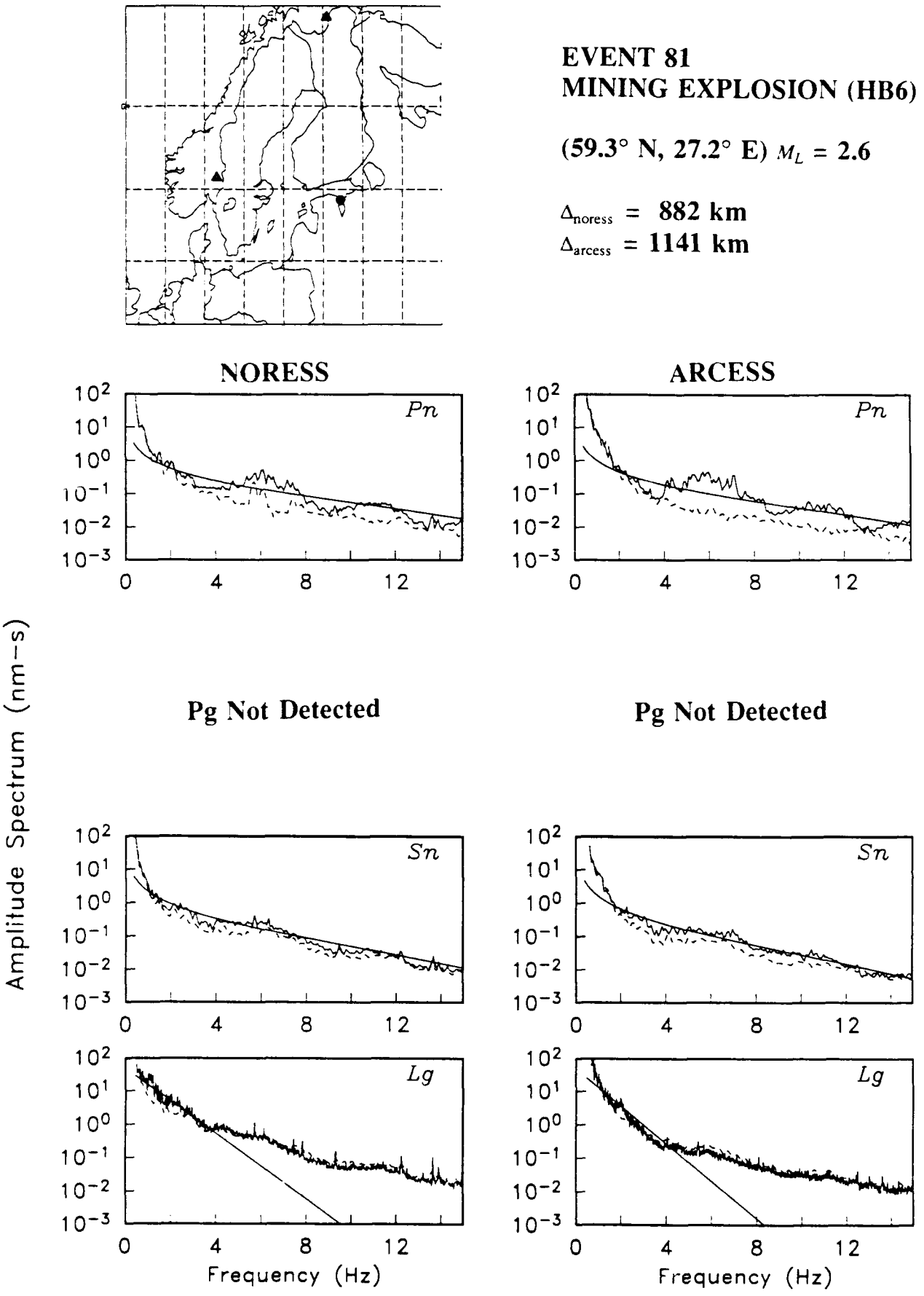

Figure A.4 Theoretical and observed spectra at NORESS and ARCESS for a mining explosion near Estonia, USSR.

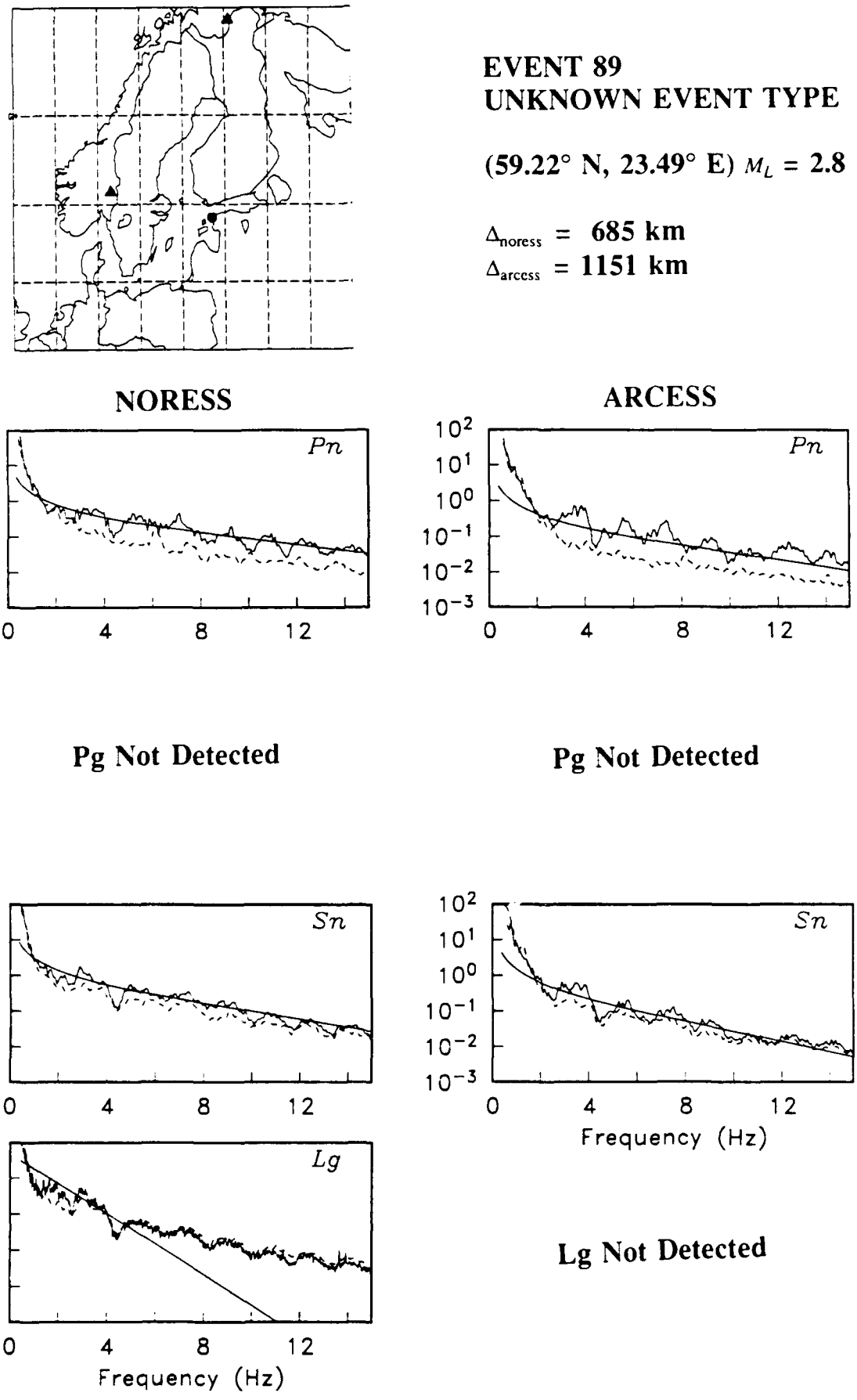

Figure A.5 Theoretical and observed spectra at NORESS and ARCESS for an event (unknown origin) near Estonia, USSR.

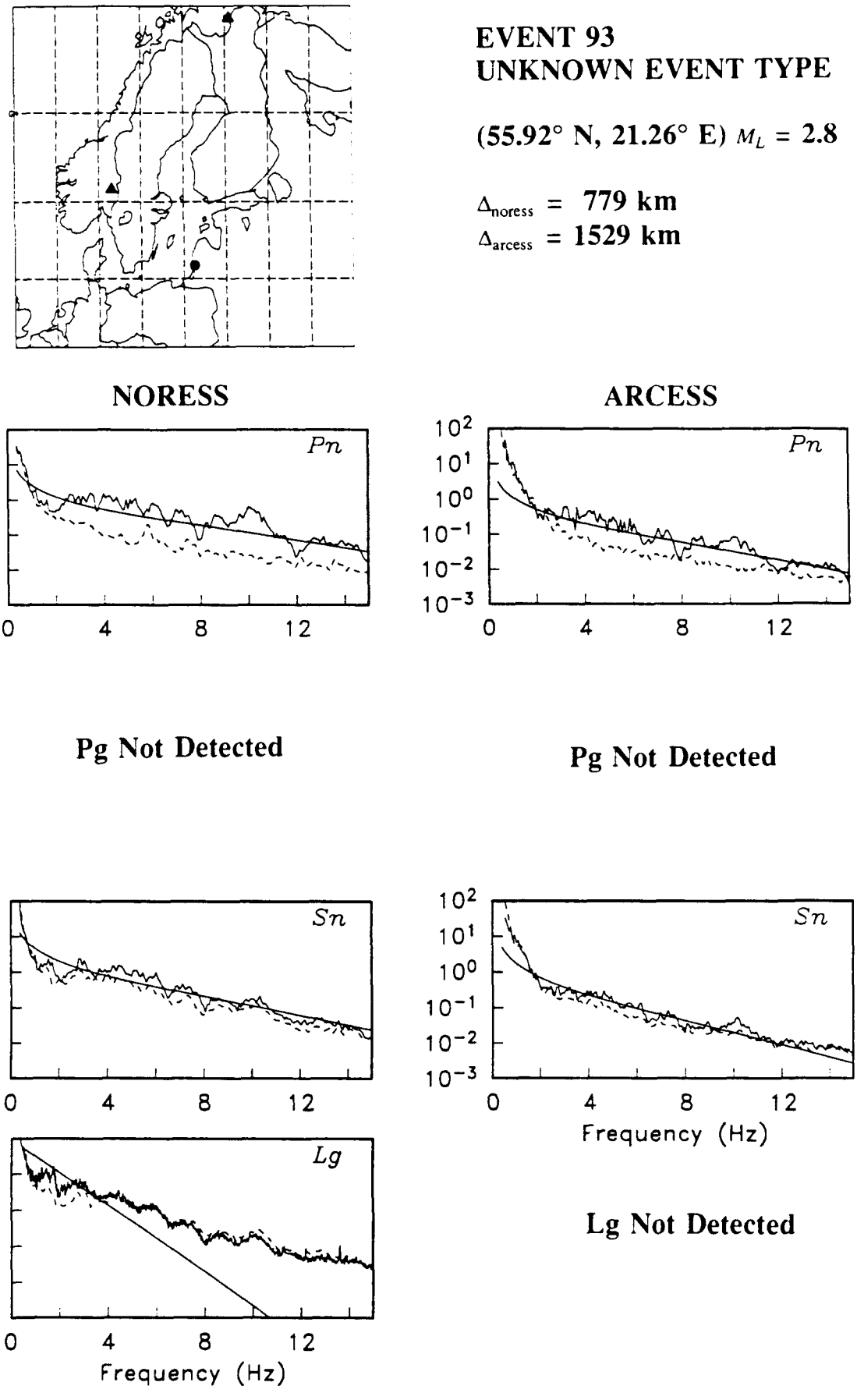

Figure A.6 Theoretical and observed spectra at NORESS and ARCESS for an event (unknown origin) near Lithuania, USSR.

(THIS PAGE INTENTIONALLY LEFT BLANK)

DISTRIBUTION LIST
FOR UNCLASSIFIED REPORTS
DARPA-FUNDED PROJECTS
(Last Revised: 26 Nov 90)

RECIPIENT	NUMBER OF COPIES

DEPARTMENT OF DEFENSE

DARPA/NMRO ATTN: Dr. R. Alewine and Dr. A. Ryall, Jr 1400 Wilson Boulevard Arlington, VA 22209-2308	2
Defense Intelligence Agency Directorate for Scientific and Technical Intelligence Washington, D.C. 20340-6158	1
Defense Nuclear Agency Shock Physics Directorate/SD Washington, D.C. 20305-1000	1
Defense Technical Information Center Cameron Station Alexandria, VA 22314	2

DEPARTMENT OF THE AIR FORCE

AFOSR/NP Bldg 410, Room C222 Bolling AFB, Washington, D.C. 20332-6448	1
AFTAC/STINFO Patrick AFB, FL 32925-6001	1
AFTAC/TT Patrick AFB, FL 32925-6001	3
AFWL/NTESG Kirkland AFB, NM 87171-6008	1

GL/LWH 1
ATTN: Mr. James Lewkowicz
Terrestrial Sciences Division
Hanscom AFB, MA 01731-5000

AFTAC/Center for Seismic Studies 1
Attn: Dr. Robert Blandford
1300 North 17th Street Suite 1450
Arlington, VA 22209-2308

DEPARTMENT OF THE NAVY

NORDA 1
ATTN: Dr. J. A. Ballard
Code 543
NSTL Station, MS 39529

DEPARTMENT OF ENERGY

Department of Energy 1
ATTN: Mr. Max A. Koontz (DP-331)
International Security Affairs
1000 Independence Avenue
Washington, D.C. 20585

Lawrence Livermore National Laboratory 3
ATTN: Dr. J. Hannon, Dr. S. Taylor, and Dr. K. Nakanishi
University of California
P.O. Box 808
Livermore, CA 94550

Los Alamos Scientific Laboratory 2
ATTN: Dr. C. Newton
P.O. Box 1663
Los Alamos, NM 87544

Sandia Laboratories 1
ATTN: Mr. P. Stokes, Dept. 9110
P.O. Box 5800
Albuquerque, NM 87185

OTHER GOVERNMENT AGENCIES

Central Intelligence Agency 1
ATTN: Dr. L. Turnbull
OSI/NED, Room 5G48
Washington, D.C. 20505

U.S. Arms Control and Disarmament Agency 1
ATTN: Dr. M. Eimer
Verification and Intelligence Bureau, Room 4953
Washington, D.C. 20451

U.S. Arms Control and Disarmament Agency 1
ATTN: Mr. R. J. Morrow
Multilateral Affairs Bureau, Rm 5499
Washington, D.C. 20451

U.S. Geological Survey 1
ATTN: Dr. T. Hanks
National Earthquake Research Center
345 Middlefield Road
Menlo Park, CA 94025

US Geological Survey 1
Attn: Dr. William S. Leith
Mail Stop 928
Reston, VA 22092

U.S. Geological Survey MS-913 1
ATTN: Dr. R. Masse
Global Seismology Branch
Box 25046, Stop 967
Denver Federal Center
Denver, CO 80225

UNIVERSITIES

Boston College 1
ATTN: Dr. A. Kafka
Western Observatory
381 Concord Road
Weston, MA 02193

California Institute of Technology 1
ATTN: Dr. D. Harkrider
Seismological Laboratory
Pasadena, CA 91125

Columbia University 1
ATTN: Dr. L. Sykes
Lamont-Doherty Geological Observatory
Palisades, NY 10964

Cornell University 1
ATTN: Dr. M. Barazangi
INSTOC
Snee Hall
Ithaca, NY 14853

Harvard University 1
ATTN: Dr. J. Woodhouse
Hoffman Laboratory
20 Oxford Street
Cambridge, MA 02138

Massachusetts Institute of Technology 3
ATTN: Dr. S. Soloman, Dr. N. Toksoz, and Dr. T. Jordon
Earth Resources Laboratory
42 Carleton Street
Cambridge, MA 02142

Southern Methodist University 2
ATTN: Dr. E. Herrin and Dr. B. Stump
Institute for the Study of Earth and Man
Geophysical Laboratory
Dallas, TX 75275

Southern Methodist University 1
ATTN: Dr. Gary McCartor
Department of Physics
Dallas, TX 75275

State University of New York at Binghamton 1
ATTN: Dr. F. Wu
Department of Geological Sciences
Vestal, NY 13901

St. Louis University 2
ATTN: Dr. B. Mitchell and Dr. R. Herrmann
Department of Earth and Atmospheric Sciences
3507 Laclede
St. Louis, MO 63156

The Pennsylvania State University 1
ATTN: Dr. S. Alexander
Geosciences Department
403 Deike Building
University Park, PA 16802

University of Arizona 1
ATTN: Dr. T. Wallace
Department of Geosciences
Tucson, AZ 85721

University of California, Berkeley 1
ATTN: Dr. T. McEvilly
Seismographic Station
Berkeley, CA 94720

University of California, Los Angeles 1
ATTN: Dr. L. Knopoff
405 Hilgard Avenue
Los Angeles, CA 90024

University of California, San Diego 1
ATTN: Dr. J. Orcutt and Ms. Ann Kerr
Scripps Institute of Oceanography
La Jolla, CA 92093

University of Colorado 1
ATTN: Dr. C. Archambeau
CIRES
Boulder, CO 80309

University of Illinois 1
ATTN: Dr. S. Grand
Department of Geology
1301 West Green Street
Urbana, IL 61801

University of California, Santa Cruz 1
ATTN: Dr. T. Lay
Institute of Tectonics
Earth Science Board
Santa Cruz, CA 95064

University of Cambridge 1
ATTN: Dr. K. Priestley
Bullard Labs, Dept of Earth Sciences
Madingley Rise, Madingley Road
Cambridge CB3, OEZ, England

University of Southern California 1
ATTN: Dr. K. Aki
Center for Earth Sciences
University Park
Los Angeles, CA 90089-0741

DEPARTMENT OF DEFENSE CONTRACTORS

Analytical Sciences Corporation, The 1
Dr. Richard Sailor
ATTN: Document Control
55 Walkers Brook Drive
Reading, MA 01867

Applied Theory, Inc. 1
ATTN: Dr. J. Trulio
930 South La Brea Avenue
Suite 2
Los Angeles, CA 90036

Center for Seismic Studies 2
ATTN: Dr. C. Romney and Mr. R. Perez
1300 N. 17th Street, Suite 1450
Arlington, VA 22209

ENSCO, Inc. 1
ATTN: Mr. John R. Stevenson
P.O. Box 1346
Springfield, VA 22151

ENSCO, Inc. 1
ATTN: Dr. R. Kemerait
445 Pineda Court
Melbourne, FL 32940-7508

Martin-Marietta
ATTN: Mr. R. J. Woodard
Chesapeake Instrument Division
6711 Baymeado Drive
Glen Burnie, MD 21061 — 1

Maxwell Laboratories, Inc.
S-CUBED Reston Geophysics Office
Reston International Center
ATTN: Mr. J. Murphy, Suite 1212
11800 Sunrise Valley Drive
Reston, VA 22091 — 1

Mission Research Corporation
Attn: Mark Fisk
735 State Street
PO Drawer 719
Santa Barbara, CA 93102 — 1

Pacific Sierra Research Corp.
ATTN: Mr. F. Thomas
12340 Santa Monica Boulevard
Los Angeles, CA 90025 — 1

Pacific-Sierra Research Corporation
Attn: Dr. Karl F. Veith
1401 Wilson Boulevard
Arlington, VA 22209 — 1

Rockwell International
ATTN: B. Tittmann
1049 Camino Dos Rios
Thousand Oaks, CA 91360 — 1

Rondout Associates, Inc.
ATTN: Dr. P. Pomeroy
P.O. Box 224
Stone Ridge, NY 12484 — 1

Science Applications International Corporation
ATTN: Document Control (Dr. T. Bache, Jr.)
10260 Campus Point Drive
San Diego, CA 92121 — 1

Science Horizons 2
ATTN: Dr. T. Cherry and Dr. J. Minster
710 Encinitas Blvd.
Suite 101
Encinitas, CA 92024

S-CUBED, A Division of Maxwell 1
Laboratories, Inc.
ATTN: Dr. Keith L. McLaughlin
P.O. Box 1620
La Jolla, CA 92038-1620

Sierra Geophysics, Inc. 2
ATTN: Dr. R. Hart and Dr. G. Mellman
11255 Kirkland Way
Kirkland, WA 98033

SRI International 1
ATTN: Dr. A. Florence
333 Ravenswood Avenue
Menlo Park, CA 94025-3493

Teledyne Industries, Inc. 1
Teledyne Geotech Alexandria Laboratories
ATTN: Mr. W. Rivers
314 Montgomery Street
Alexandria, VA 22314-1581

Woodward-Clyde Consultants 1
ATTN: Dr. L. Burdick
P.O. Box 93254
Pasadena, CA 91109-3254

NON-US RECIPIENTS

Blacknest Seismological Center 1
ATTN: Mr. Peter Marshall
Atomic Weapons Research Establishment
UK Ministry of Defense
Brimpton, Reading RG7-4RS
United Kingdom

National Defense Research Institute 1
ATTN: Dr. Ola Dahlman
Stockholm 80, Sweden

NTNF NORSAR 1
ATTN: Dr. Frode Ringdal
P.O. Box 51
N-2007 Kjeller
Norway

OTHER DISTRIBUTION

To be determined by the project office 4

TOTAL 81